Dynamics and variability of the Subantarctic mixed-layer as determined from a high-resolution glider dataset

Marcel David du Plessis

A thesis presented for the degree of
Master of Science

Department of Oceanography

University of Cape Town

Supervisors

Dr. Sebastiaan Swart

Southern Ocean Carbon and Climate Observatory, CSIR, Rosebank, South Africa

Dr. Amala Mahadevan

Woods Hole Oceanographic Institution, Woods Hole, MA, United States of America

Ass. Prof. Isabelle Ansorge

Department of Oceanography, University of Cape Town, Rondebosch, Cape Town, South Africa

Dr. Jennifer Jackson-Veitch

Department of Oceanography, University of Cape Town, Rondebosch, Cape Town, South Africa

Abstract

Traditional understanding of mixed-layer (ML) dynamics in the African sector of the Southern Ocean suggests that seasonal summer stratification and subsequent reduction in ML depth (MLD) is determined by the onset of a positive net heat flux. The impact of physical forcing mechanisms on the intra-seasonal variability of the ML is still relatively unknown. Recent research in the North Atlantic has highlighted the role that sub-mesoscale ML eddy dynamics has on ML stratification. It is now understood that large horizontal density gradients drive sub-mesoscale eddy formation which have been shown to result in the early onset of spring phytoplankton blooms at high latitudes. To date these ML eddies have been researched primarily in models with few observational studies available. To test the ML eddy hypothesis in the Subantarctic Zone (SAZ) we use high-resolution ($\sim$3km, 4-hourly) glider measurements between austral spring to late summer. Strong contrasts between a highly variable spring ML (12-272 m) and strongly stratified summer ML ($<$100 m) are observed in the dataset. We propose that ML eddies have a far larger affect on stratification in the austral spring with large rates of restratification ($>$100 $m\ day^{-1}$) whereas solar heating increases the mean surface layer stratification (N^2 $>1.1 \times 10^{-5}\ s^{-2}$) during the austral summer months, inhibiting mixing. As the ML eddies are governed by large horizontal buoyancy gradients, comparisons of the observed gradient distributions from spring and summer are examined with their impact on stratification. Furthermore, during summer, modulations of the MLD are observed to occur in agreement to increases in wind stress at the synoptic scale (storms). This has potential implications for sustaining phytoplankton production, when nutrient limitation inhibits growth, and therefore carbon export in the ocean.

Acknowledgements

I was lucky to have four supervisors involved in my M.Sc, each contributing to get me to this point. Dr. Seb Swart's role began two years and 836 emails ago. Sitting in a dirty Thai train station, I get an email from Seb: "I need someone responsible to run the UCTD on a cruise to Antarctica, will you go?". That sentence sums you up, Seb. You entrust me with responsibility knowing full well that you probably shouldn't, and provide me with opportunities where I have travelled to Antarctica, the USA and New Zealand. Seb's initiating and running of South Africa's first ever glider program has ensured almost limitless possibilities for me to learn in both the scope of my project as well as getting involved in a successful ocean science program. Thank you, Seb.

To Ass. Prof. Isabelle Ansorge, your expertise and ever willing nature for a good old rant will always be looked upon fondly. Also, your financial assistance and encouragement in setting me on my way to my first international conference will not be forgotten.

To Dr. Jenny Jackson-Veitch, whose time was limited yet offered support whenever asked for and helped me to see the wood from the trees. Also, Dr. Julie Deschayes, your joy in learning is infectious.

To my advisor in the USA, Dr. Amala Mahadevan. The two months I spent at Woods Hole gave my project significant traction and direction. To yourself, Melissa and Mariona, my stay in Woods Hole will always be a fond memory.

Thank you to those at SOCCO for making my project possible; Dr. Pedro Monteiro, Seb, Dr. Sandy Thomalla and Dr. Nicolette Chang as well as the guys at SAMERC; Derek, Andre, JP and Sinekhaya, who facilitated the glider operations for SOSCEx. To Seb, Sandy, Nicollette, Emma, Luke, Warren, Sarah and Precious for lunches in the sun and some good office banter. To my mates, Jen, Kyle vdM, Kate, Laura, Sandi, Putty, Skippy, Kyle C, Momo, Chris J: Writing a thesis has taught me many things about perseverance, but nothing quite matches up to the shear determination of being at Hudsons every Friday.

A huge thanks to my family for offering never-ending support and understanding. I appreciate the interest you have shown in my work and life and always willing me to go forward and be better. I have learnt a lot from you. Finally to my best friend, I don't think it is

possible to overemphasize the patience and encouragement you showed me. From celebrating minor breakthroughs, through the ever popular "you don't understand how much work I have" comments, supporting me despite being on the other side of the world at times and listening to my problems and triumphs. I am very grateful for everything, thank you Jen.

Funding

I would like to thank the National Research Foundation of the Department of Science and Technology, South Africa for financial support through the award of an Innovation Bursary for the tenure my Master of Science degree.

I got a big contribution from my collaboration at the Woods Hole Oceanographic Institution, MA, United States of America. I would like to thank the following for providing financial assistance in making this possible:

1. National Research Foundation, Department of Science and Technology, South Africa

2. Marine Research Institute, University of Cape Town, Rondebosch, South Africa

3. Postgraduate Funding Office, University of Cape Town, Rondebosch, South Africa

Acronyms

ACC:	Antarctic Circumpolar Current
APF:	Antarctic Polar Front
CO_2:	Carbon Dioxide
CT-Sail:	Conductivity - Temperature Sail
EMD:	Empirical Mode Decomposition
IMF:	Intrinsic Mode Function
MADT:	Maps of Absolute Dynamic Topography
ML:	Mixed-layer
MLD:	Mixed-layer Depth
OSCAR:	Ocean Surface Current Analysis Real-time
OSTIA:	Operational Sea Surface and Sea Ice Analysis
sACCf:	Southern Antarctic Circumpolar Current Front
SAF:	Subantarctic Front
SAZ:	Subantarctic Zone
SBdy:	Southern Boundary
SG573:	Seaglider 573
SOSCEx:	Southern Ocean Seasonal Cycle Experiment
SSH:	Sea Surface Height
SST:	Sea Surface Temperature
STF:	Subtropical Front
STSW:	Subtropical Surface Water
T-S:	Temperature - Salinity

Contents

List of Figures

List of Tables

Literature Review

1.1 The Southern Ocean

The Southern Ocean is a unique environment in that it extends circumpolar around Antarctica with no continental barriers. It is characterised by a steep meridional gradient in water mass properties, with warm, Subtropical waters toward the north and cold Antarctic water toward the south. In the core of the Southern Ocean, around 45°- 55° S, a band of the world's most intense westerly winds drive a major eastward flowing surface current, the Antarctic Circumpolar Current (ACC) (Nowlin and Klinck, 1986; Trenberth et al., 1990).

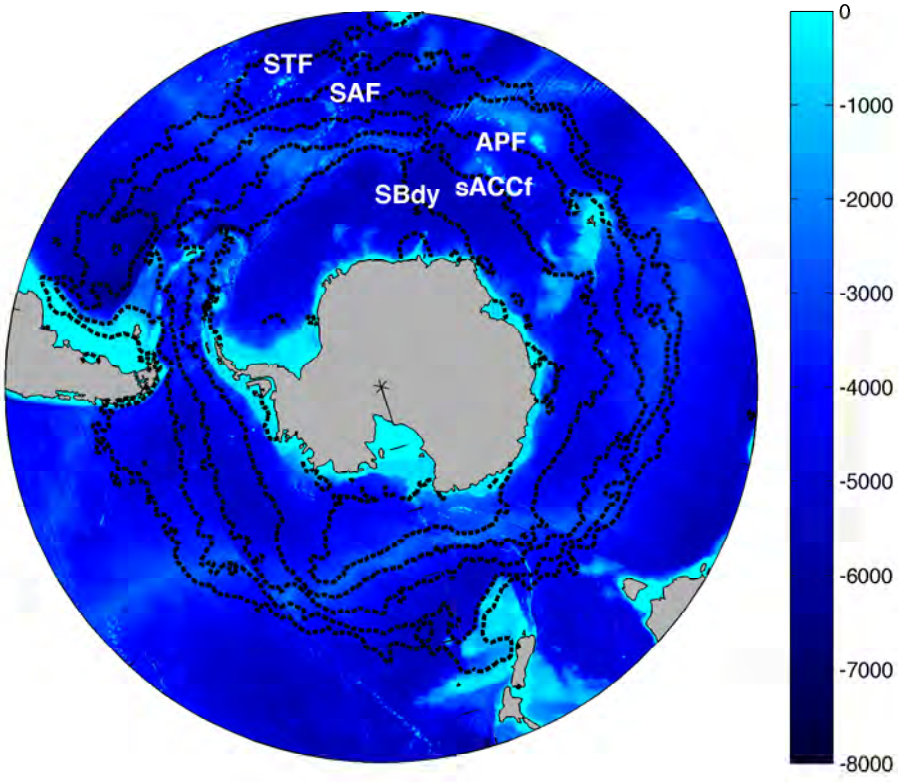

Figure 1.1: Location of the circumpolar frontal bands (dotted black lines) across the Southern Ocean determined from satellite altimetry (*dynamic m*, Swart and Speich, 2010) over the period of the Southern Ocean Seasonal Cycle Experiment (SOSCEx). From north to south, the Subtropical Front (STF), Subantarctic Front (SAF), Antarctic Polar Front (APF), southern ACC front (sACCf) and the Southern Boundary (SBdy). Ocean bathymetry is acquired from the ETOPO1 dataset (meters below sea level).

The ACC absorbs and stirs up the heat and salt properties from the Atlantic, Indian and Pacific Oceans, redistributing them northward through the Atlantic passageway. This forms a key mechanism for the global Meridional Overturning Circulation and the mediation of the global climate system (Rintoul, 1991; Gordon et al., 1992; Speich et al., 2001).

1.1.1 Southern Ocean fronts

The pronounced north-south gradients of density within the Southern Ocean can largely be characterised by a series of steps, or frontal bands (Orsi et al., 1995; Belkin and Gordon, 1996) (Figure 1.1). The location of the fronts were characterised by Orsi et al. (1995) as a series of sub-surface temperature criteria, which in order to investigate would require an extensive array of Conductivity, Temperature, Depth (CTD) casts up to 400 m. Later, Swart et al. (2008) was able to infer the same fronts using satellite altimetry, making their locations easily identifiable from remotely sensed data.

The Subtropical Front (STF) demarcates the northern extent of the Southern Ocean, separating warmer, saltier Subtropical waters from the colder, fresher Subantarctic Zone (SAZ) (Clifford, 1983; Orsi et al., 1995). Further south, the Subantarctic Front (SAF) marks the start of cold Antarctic waters where, combined with the Antarctic Polar Front (APF) is considered the core of the ACC (Rintoul and Sokolov, 2001). South of the APF is the Antarctic Zone, which encompasses the southern ACC front (sACCf) and the Southern Boundary (Sbdy) of the ACC. The fronts are characterised by intense mesoscale (10-100 km) flow variability where meanders of the fronts, eddies and intense lateral gradients in temperature result in jet-like filaments (Sokolov and Rintoul, 2007; Arhan et al., 2011). The meanders are largely directed by topographical steering (*e.g.* at the South-West Indian Ridge, Ansorge and Lutjeharms, 2003) meaning that the latitudinal locations of the frontal bands vary with longitude (Figure 1.1). At the location of the fronts, outcropping isopycnals that slope upward to the south display different water mass properties that have associated stratification and biological distributions (Pollard et al., 2002; Thomalla et al., 2011).

1.1.2 The Subantarctic Zone

The SAZ encompasses the region between STF and SAF and forms the meeting place of the warmer and saltier waters of Subtropical origin and the much colder and fresher polar waters. Topographical steering occurs over a large latitudinal extent where south of Africa, the northern limit of the SAZ is observed around 39.9° S down to its southern most coverage of 47.6° S, as defined by Swart and Speich (2010).

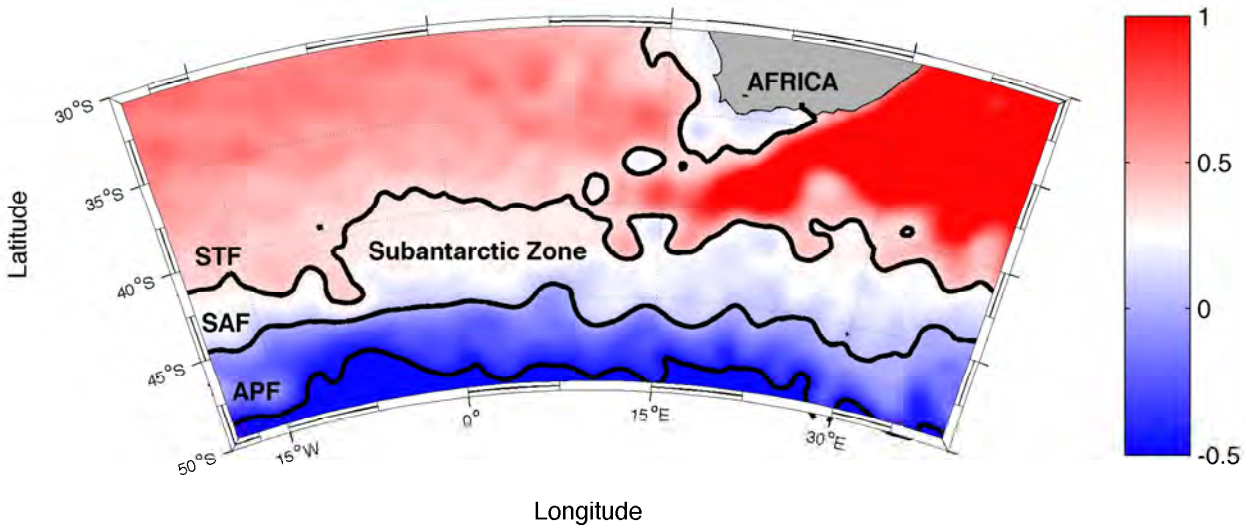

Figure 1.2: The SAZ forms the meeting place of warmer, less dense water from the north and colder, denser water from the south. Satellite altimetry (*dynamic m*) south of Africa indicates the large meridional density gradients that set up the lateral fronts of the Southern Ocean. Black lines indicate from north to south the STF, SAF and the APF as determined from satellite altimetry (see Swart and Speich, 2010).

It has an approximate width of 540 km south of Africa (Swart and Speich, 2010) and differs considerably in water mass properties from regions to the north and south. South of Australia, surface temperature changes can be up to 5 $°C$ within a width of 120 km (Rintoul and Trull, 2001). Figure 1.2 indicates the intense meridional gradient in satellite altimetry where a decline in sea surface height (SSH) indicates an increase in the vertically depth-compensated density structure. In terms of the stratification dynamics, the flow of warmer, lighter water from the northern region of the SAZ results in temperature dominating salinity in the contribution to vertical density stratification. The southern region of the SAZ is salinity

compensated as a result of the cross-frontal exchange of colder, fresher water over the SAF. The addition of transient pulses of mesoscale eddies and frontal meanders at the northern boundary of the SAZ induced by the Agulhas Return Current contributes to the already intense flow variability by increasing the lateral gradient in physical properties (Lutjeharms and Ansorge, 2001; Faure et al., 2011). The increase in flow injects strong horizontal velocities into the SAZ that are able to generate intense kinetic energy and drive deep mixing (Durgadoo et al., 2011; Arhan et al., 2011).

1.2 Problem Identification

1.2.1 Coupling the physical-biological importance of the Southern Ocean

The Southern Ocean biological pump is a globally important process, estimating to remove around 3 $PgC\ yr^{-1}$ from surface waters (33% of the global organic carbon flux) (Schlitzer, 2002). Despite this, the Southern Ocean is considered a high-nitrate, low chlorophyll region, meaning that it holds a large inventory of macro-nutrients but has low average phytoplankton biomass (Boyd et al., 1999). This is a direct result of phytoplankton growth being subdued due to the limitation of iron (Fe) and sunlight; important ingredients in phytoplankton growth (Fauchereau et al., 2011).

A fundamental dynamic in alleviating or promoting this limitation is the vertical density stratification that suppresses turbulence and defines the depth of the mixed-layer (MLD). The MLD is critical in that it forms the base of the ML, where within lies the environmental habitat for phytoplankton cells and where gases, such as CO_2 communicate directly with the atmosphere at the air-sea interface (de Boyer Montégut et al., 2004). Additionally, the depth of the ferricline, where $\partial Fe/\partial z$ is maximal is often deeper than the MLD, and thus the subsequent depletion of Fe within the ML by phytoplankton growth inhibits further growth (Boyd et al., 1999; Tagliabue et al., 2014). Therefore, restocking the ML with Fe is important in enhancing primary production. For this to happen the MLD must be deeper than the ferri-

cline where Fe is entrained into the ML. However, in order for phytoplankton growth rates to exceed grazing and lead to phytoplankton blooms, the MLD must be shallower than the depth where light enters the ocean (euphotic depth), as phytoplankton cells require sunlight to grow (Sverdrup, 1953). Therefore, changes in MLD are crucial in determining the amount of phytoplankton growth with respect to depth and time below the ferricline (restocking the ML with Fe) and time above the euphotic depth (light availability to phytoplankton cells).

A principle driver of changes in stratification, and thereby MLD, is the transfer of momentum and energy through solar induced surface buoyancy fluxes, acting on seasonal to sub-seasonal time scales (Fauchereau et al., 2011; Schulz et al., 2012). The MLD is predicted to be greatly affected by the effects of climate change as increased heating leads to increased stratification. This is postulated to result in a decrease in the vertical exchange of nutrients (including Fe) into the ML, weakening the Southern Ocean carbon sink (Sarmiento et al., 1998; Bopp et al., 2005). The seasonal cycle, one of the strongest modes of variability, is a key mechanism in monitoring this hypothesis as it links the physical mechanisms of climate forcing to biological production in the Southern Ocean (Sallée et al., 2010; Monteiro et al., 2011; Tagliabue et al., 2014).

The seasonal cycle

A recent study by Tagliabue et al. (2014) observes that deep winter mixing (depths extending >300 m) below the ferricline is critical for restocking the ML with Fe (Figure 1.3), with seasonal fluxes in the surface buoyancy playing a major role in this process.

In comparison to summer, maximum cooling in winter reaches below $-200\ W\ m^2$ and cools the ocean surface, thereby weakening the vertical temperature gradient, deepening the MLD >300 m (Rintoul and Trull, 2001; Sallée et al., 2010). During this time, phytoplankton cells remain mixed down below the euphotic depth (where light enters the ocean), thus the unavailability of light means primary production is low. During springtime, a change to positive surface buoyancy forcing and a seasonal shoaling of the MLD (to depths less than 50 m, Swart et al., 2014) above the euphotic depth means that phytoplankton remain in the sunlight layer for sufficient time to allow for net community growth and a bloom in phytoplankton pro-

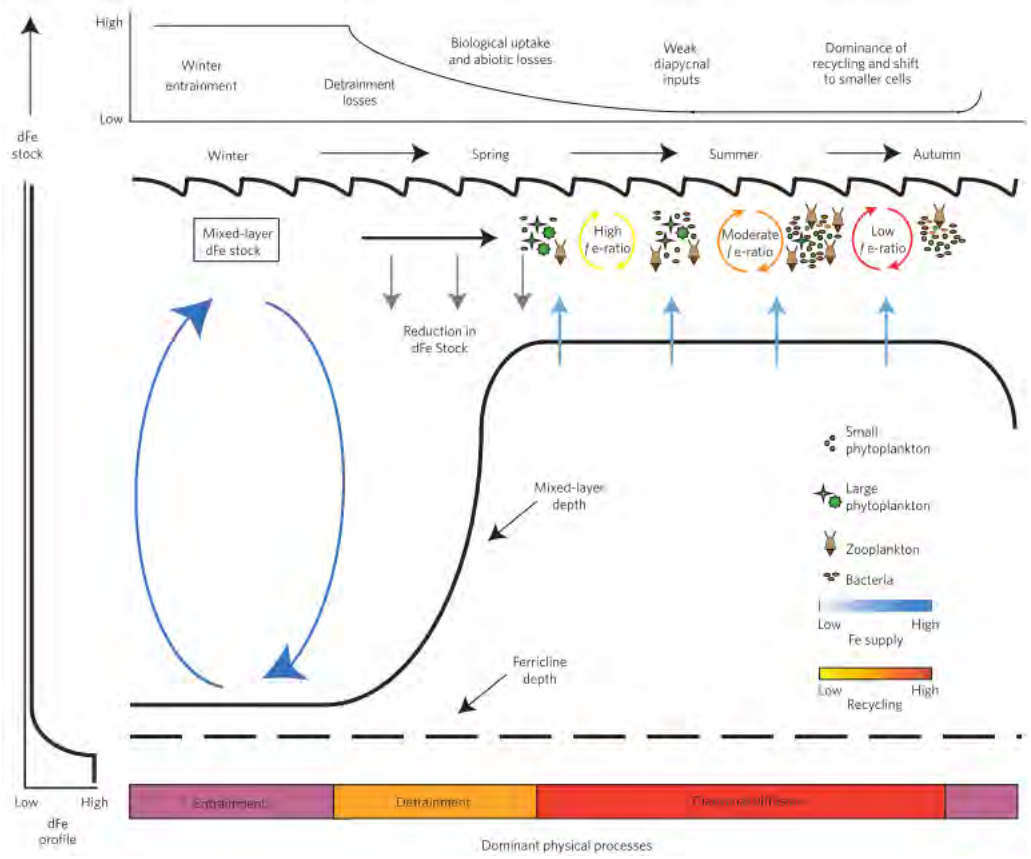

Figure 1.3: Seasonal cycle of the physical Fe supply into the ML. Deep MLs in winter entrain Fe with low productivity due to limited light. Spring shoaling of the MLD allows for phytoplankton growth. As the Fe stock reduces into summer, phytoplankton species change due to the reliance on recycled Fe (from Tagliabue et al., 2014).

duction (Sverdrup, 1953). In summer, maxima in buoyancy forcing (>300 $W\ m^{-2}$) (Schulz et al., 2012) further shoals the MLD to constantly <100 m (Swart et al., 2014) whereby the depletion of the Fe stock in the ML by phytoplankton production lead to declining growth rates, where other pelagic communities dominate (Boyd et al., 1999; Tagliabue et al., 2014).

Therefore, understanding the seasonal cycle that couples climate variability to ocean productivity is key in determining the amount of seasonal phytoplankton production and accurately predicting long-term trends in the ocean carbon cycle (Lenton et al., 2013). However, coupled physical-biogeochemical Southern Ocean models are unable to robustly predict the seasonal onset of phytoplankton production and thereby misrepresent the phytoplankton production budget (*e.g.* Beaulieu et al., 2013). An important finding by Thomalla et al. (2011)

indicates that one of the reasons for the knowledge gap in determining phytoplankton budgets is that the physical mechanisms explaining phytoplankton production vary spatially and temporally. This is illustrated in Figure 1.4 where zonal classifications of biological importance within the Southern Ocean occur through the separation of regions of low and high chlorophyll concentrations (*proxy* for phytoplankton growth) as well as their respective seasonal reproducibility, which is essentially the ability to reproduce the seasonal timing and amplitude of biological productivity (Thomalla et al., 2011).

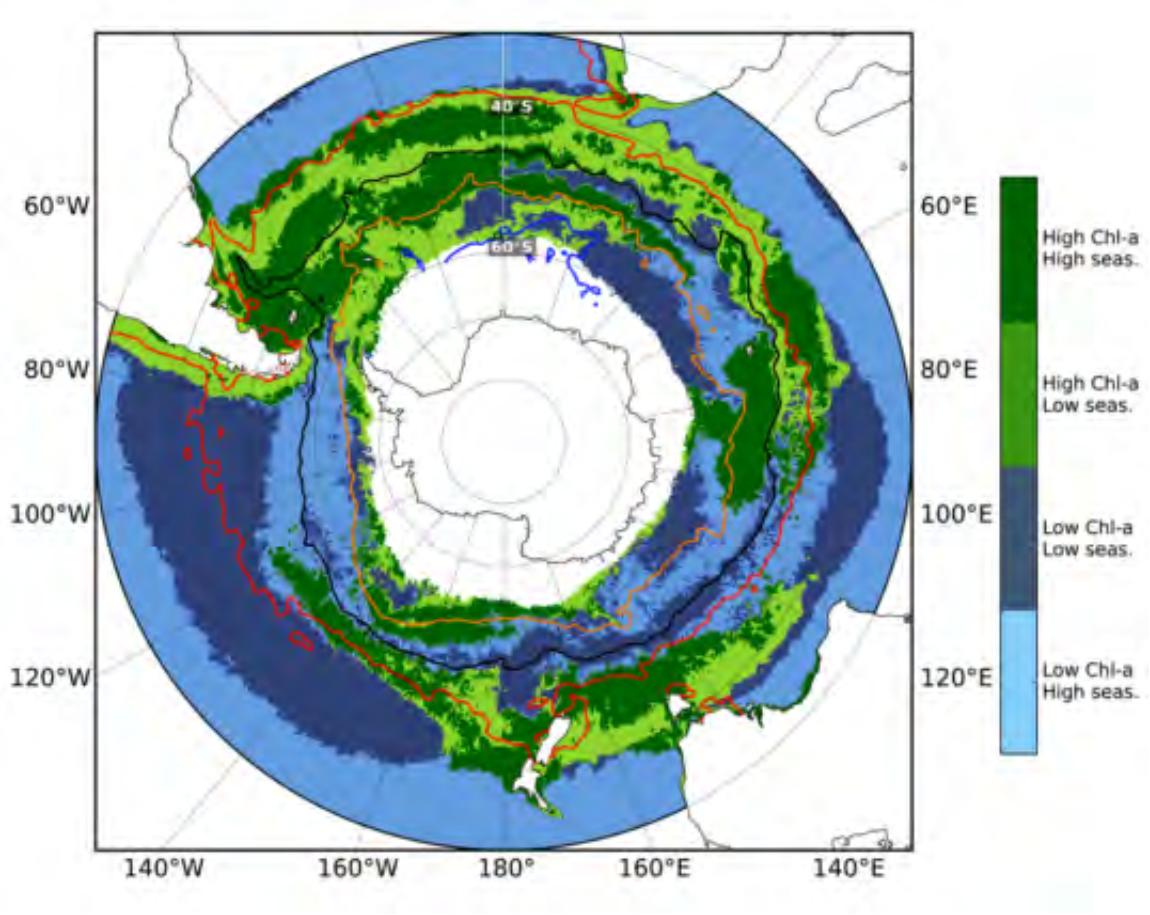

Figure 1.4: Schematic indicating the response of phytoplankton biomass to the underlying physics of different seasonal regimes. Regions in blue indicate low chlorophyll concentrations with either high seasonal reproducibility (light blue) for low seasonal reproducibility (dark blue). Regions in green indicate high chlorophyll concentrations with either high seasonal reproducibility (dark green) or low seasonal reproducibility (light green) (Thomalla et al., 2011).

Regional and temporal asymmetry in phytoplankton growth within the SAZ

The region encompassing the SAZ shows to be the largest zonally averaged region of the Southern Ocean for oceanic sinks of CO_2 (Figure 1.4) (Metzl et al., 1999; Thomalla et al., 2011). However, within this region there are sizeable areas that are particularly poor in reproducing the timing of the seasonal onset of phytoplankton growth, suggesting strong inter-seasonal variability in the transition between deep winter mixing to a shallow MLD in spring. Recent studies in the Southern Ocean are beginning to show that at sub-seasonal time scales and sub-mesoscales (1-10 km), the response of phytoplankton to climate forcing mechanisms are becoming critical (Fauchereau et al., 2011; Swart et al., 2014).

Swart et al. (2014) suggest that meso- to sub-mesoscale features occurring within the ML increase the vertical stratification and lead to early spring phytoplankton growth. This occurs before the onset of solar induced stratification, which was originally thought to dictate the springtime shoaling of the MLD (Waniek, 2003; Henson et al., 2006). This is a critical observation in the regimes of both Southern Ocean physical-biological coupling and sub-mesoscale restratification dynamics. It is the first observation in the SAZ that links sub-mesoscale features to increases in phytoplankton growth and provides a possible explanation to the low seasonal reproducibility in Figure 1.4 as sub-mesoscale features are spatial and temporally patchy (Mahadevan and Tandon, 2006).

It displays additional significance in ML ocean physics as it provides observational evidence to many model studies that have investigated the role of lateral density gradients in restratifying the ML (Tandon and Garrett, 1994, 1995; Marshall and Jones, 2002; Thomas et al., 2008; Mahadevan and Tandon, 2006; Boccaletti et al., 2007; Fox-Kemper et al., 2008; Mahadevan et al., 2010; Taylor and Ferrari, 2011; Levy and Martin, 2013). It also forms a basis for comparison to observations in the North Atlantic (Mahadevan et al., 2012b) and Mediterranean (Olita et al., 2014), where sub-mesoscale physical processes directly influence rapid restratification of the springtime MLD and onset phytoplankton production. The study by Swart et al. (2014) inferred the presence of sub-mesoscale features based on lateral gradients in the surface buoyancy but did not apply any quantified analysis used in the Northern

Hemisphere observations and model studies.

Additionally, a study by Fauchereau et al. (2011) shows that in the summer regime, sub-seasonal transient wind mixing events deepen the MLD sufficiently to resupply nutrients into the ML and subsequently lead to an increase in phytoplankton productivity. This study along with Swart et al. (2014) highlighted the importance of sub-seasonal wind variability on the MLD in sustaining summertime phytoplankton growth, which is particularly important for the Southern Ocean as the intense westerly winds that drive the ACC are associated with the distribution of synoptic weather storms (Trenberth, 1991; Parish and Bromwich, 1998). These storms typically range from 200-1000 km, with life cycles of 4 days or longer (Yuan et al., 2009) and are immensely cold due to their Antarctic origin. They interact with warmer water below to enhance intense heat loss from the ocean and induce strong mechanical stirring, deepening the MLD further (Sallée et al., 2010). Despite these improvements in our understanding of the physical-biological link at sub-seasonal scales, there is a clear lack of understanding of the ability of the Southern Ocean to continually absorb atmospheric CO_2 at the current rate with a changing climate. There is a severe need for observational evidence that quantifies the physical environment which allows for a basis whereby change can be measured. For example, understanding the relationship between wind strength and variability in the summer and its subsequent role on MLD variability will aid in better estimating how future changes in climate will affect wind distribution and strength and impact phytoplankton growth.

1.3 Sub-mesoscale dynamics

1.3.1 Defining sub-mesoscale

An active flow field at the surface of the ocean generates strong horizontal stirring dominated by large scale currents that are enhanced at surface density fronts. At those locations, the balance between planetary vorticity (Earth's rotation) and the lateral pressure gradient allows the front to remain in balance, restoring potential energy and directing flow along the density gradient (Tandon and Garrett, 1994). As the front becomes unstable and meanders

(Figure 1.5A), it results in the growth of instabilities that intensify the lateral velocity shear and across-front buoyancy gradient, where outcropping isopycnals are pinched together. At these regions, the flow dynamics differ to the mesoscale where relative vertical vorticity ($\zeta = v_x$ - u_y) is dominated by planetary vorticity f (see Equation (1.3)). Small Rossby numbers exist, such that $R_o = |\zeta|/f \ll 1$. At the sub-mesoscale, relative vorticity becomes large whereby R_o is of the order of 1 (Figure 1.5B), thereby forming strong ageostrophic flow that occurs within the length scale of the first baroclinic Rossby radius of deformation (λ) (Mahadevan and Tandon, 2006; Boccaletti et al., 2007; Thomas et al., 2008; Lévy et al., 2012).

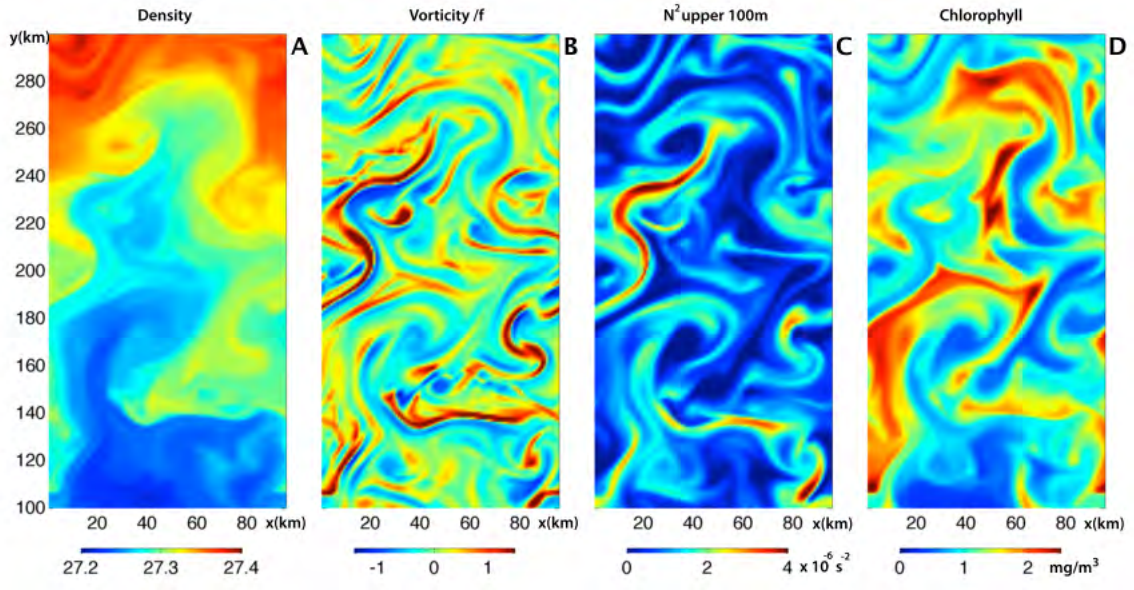

Figure 1.5: Process study 3-D model output from Mahadevan et al. (2012a) showing that in regions of A) large lateral density gradients, filaments and eddies generate sub-mesoscale fronts, where B) relative vorticity dominates f, C) enhancing the mean stratification (N^2) of the upper 100 m, and D) promoting chlorophyll (phytoplankton) enhancement.

Therefore, for length scales below λ, the term sub-mesoscale is defined. It is determined from the ratio between the first baroclinic gravity wave speed c_m of a parcel of water, and the planetary vorticity where the m denotes the baroclinic mode number (Chelton et al., 1998). The larger the first baroclinic wave speed is, the larger the length scale will be whereby frontal instabilities grow. The wave speed of a column of water is defined in Equation (1.1):

$$c_m = \frac{1}{m\pi} \int_{-H}^{0} N(z)\, dz,\ m \geq 1, \tag{1.1}$$

where N is the vertical buoyancy frequency (s^{-1}), H is the water column depth (m) and z is depth increments in m.

The first wave speed c_1 is used in determining the length scale λ:

$$\lambda = \frac{c_1}{f}, \tag{1.2}$$

where f is the planetary vorticity in s^{-1} following:

$$f = 2\Omega \sin\theta, \tag{1.3}$$

where is Ω the angular rotation of the earth at $\Omega = 2\pi/86400$ and θ is the latitude.

Chelton et al. (1998) determined this length scale to be around 10 km at high latitudes, the same length scale that model studies have defined as the sub-mesoscale (Mahadevan and Tandon, 2006; Boccaletti et al., 2007).

1.3.2 Sub-mesoscale restratification

At the sub-mesoscale relative vorticity becomes important such that both f and ζ are the same order of magnitude and therefore the lateral density gradient across the front is allowed to relax. This means that the growth of energetic eddies below λ, defined as ML eddies are able to release the potential energy that is preserved by the lateral density gradient and act to drive lighter water over heavier water.

This imparts a tilting of the vertical isopycnals towards to the horizontal (Figure 1.6), enhancing the mean stratification (N^2) of the top 100 m (Figure 1.5C). The increased strat-

ification leads to a shoaled MLD, increasing the light availability to phytoplankton thereby promoting chlorophyll growth (Figure 1.5D) (Mahadevan et al., 2012b).

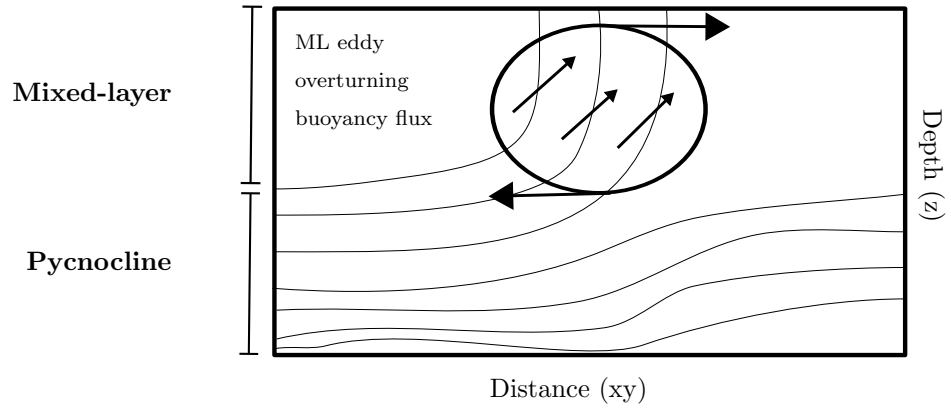

Figure 1.6: Restratification due to isopycnal slumping occurs when potential energy is released by ML eddy overturning. Thin black lines denote isopycnals, thick black lines indicate direction of ML eddy overturning buoyancy flux with circular arrows showing direction of isopycnal movement. From Fox-Kemper et al. (2008).

Parameterising ML eddy restratification from model studies

High-resolution model studies have been able to parameterise the ML eddy restratification process which is important for estimating the MLD in global climate models (Fox-Kemper et al., 2008; Mahadevan et al., 2010) and understanding estimates of phytoplankton growth (Mahadevan et al., 2012b). The models show that the dependence of ML eddy growth is reliant on the overlying wind field and surface buoyancy forcing which can either enhance or destroy the eddies.

Through surface Ekman dynamics (Ekman, 1962), wind propagating along a density front in the direction of flow (or "down-front", purple arrow in Figure 1.7) will act to advect the heavier water over the lighter water, generating a convective overturning process and destroying stratification. Conversely, an "up-front" wind will promote the advection of lighter water over heavier water and speed up the restratification process. Additionally, incoming solar radiation implies a surface buoyancy flux that can promote stratification by heating the surface and thereby increasing the vertical density gradient, or generate destratification by cooling the surface and promoting convective mixing. This sets up a competition between the stratifying effects of ML eddy overturning, up-front winds and solar heating against destratifying effects

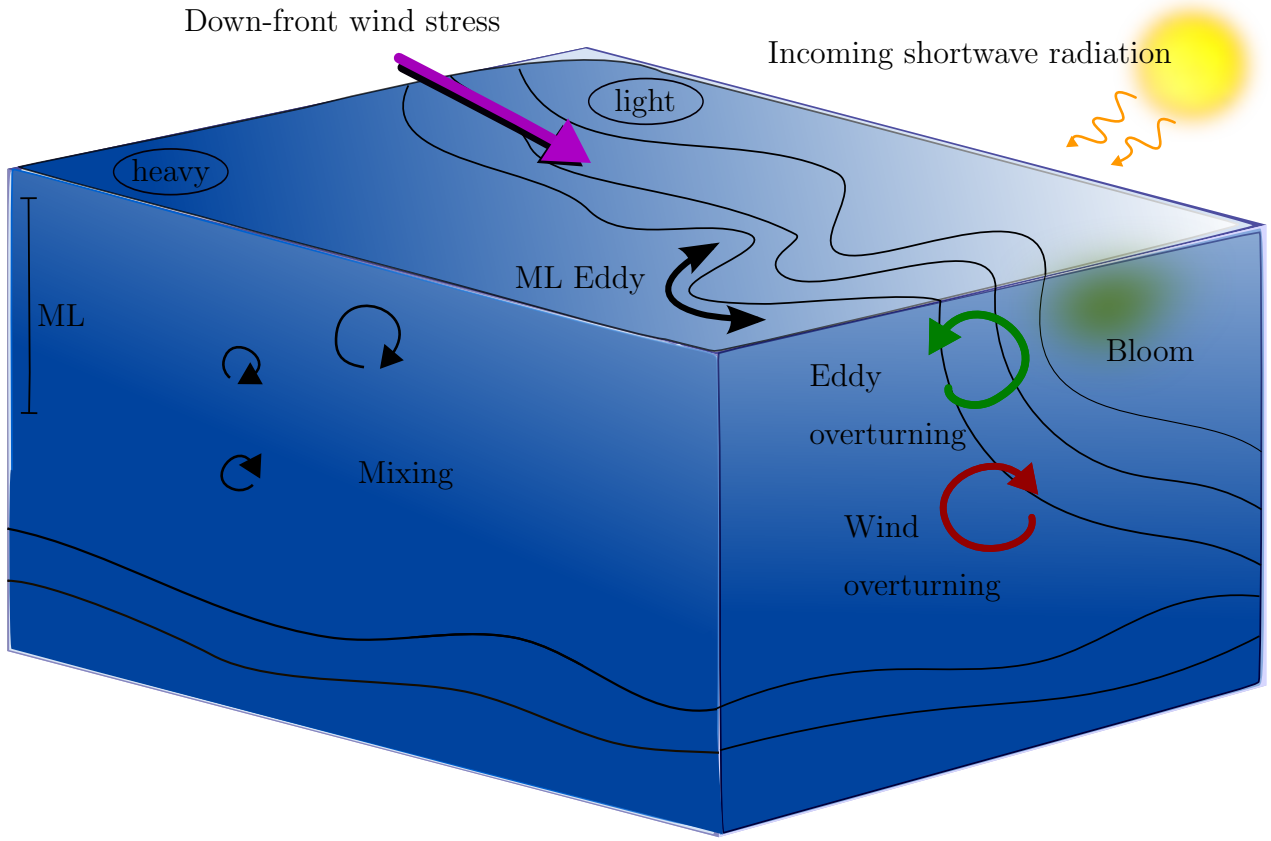

Figure 1.7: At geostrophically balanced fronts, the increase of a down-frontal wind stress will enhance the Ekman flux, increasing the wind-driven overturning circulation by transporting heavier water over lighter water. Conversely, a decrease in the down-frontal wind stress will inhibit mixing and restratify the water column. Figure adapted from Mahadevan et al. (2012b) but made for Southern Hemisphere representation.

of convective surface cooling and down-frontal winds (Mahadevan et al., 2010).

These processes are responsible for controlling the MLD and are quantified through the following processes of overturning fluxes from ML eddies, winds and cooling (heating):

The stratifying buoyancy flux from ML eddies (ψ_e) is dependent on the strength of the lateral surface buoyancy gradient (b_{xy}), the MLD and f (Fox-Kemper et al., 2008; Mahadevan et al., 2010), where b_{xy} is the lateral gradient in the buoyancy term:

$$b \equiv \frac{g\rho\prime}{\rho_0}, \tag{1.4}$$

where b is the buoyancy term (s^{-2}), g is the gravitational acceleration ($m\ s^{-2}$) and $\rho\prime$ is the deviation of surface density from a reference state ρ_0 in $kg\ m^{-3}$.

In the literature (Fox-Kemper et al., 2008; Mahadevan et al., 2010), the lateral buoyancy gradient is denoted as b_y as the gradient is directly across-frontal. In this work, however, the direction of sampling is not directly across- or along-frontal and therefore I introduce b_{xy} as the lateral buoyancy gradient. This can be calculated as follows:

$$b_{xy} = \frac{b(i+1) - b(i)}{\delta l}, \tag{1.5}$$

where i represents the profile number in increasing increments of 1, and δl is the distance (m) between profiles.

The ML eddy buoyancy flux is represented by ψ_e:

$$\psi_e = \frac{0.06\, b_{xy}\, MLD^2}{f} \tag{1.6}$$

The ML eddy buoyancy flux is converted into a mean overturning stream function which represents the vertical overturning buoyancy flux by ML eddies:

$$\langle w\prime\, b\prime \rangle_e \sim \langle \psi_e\, b_{xy} \rangle \tag{1.7}$$

Restratification by the vertical overturning buoyancy flux of ML eddies is opposed by surface cooling which inputs negative buoyancy at the ocean surface, generating vertical mixing:

$$\langle w\prime\, b\prime \rangle_{cool} = -\frac{\alpha Q g}{\rho C_p}, \tag{1.8}$$

where Q represents the net incoming heat flux ($W\ m^{-2}$), α is the thermal expansion coefficient ($1.6 \times 10^{-4}\ ^{\circ}K^{-1}$), C_p the specific heat capacity of sea water at constant pressure ($3988\ J/kg/^{\circ}K$) and ρ the surface density of the sea water sample.

Finally, destratification of the ML through wind-induced overturning from a down-frontal wind stress follows:

$$\langle w\prime\, b\prime \rangle_w \sim \langle \psi_w\, b_{xy} \rangle = \langle \frac{\tau}{\rho f}\, b_{xy} \rangle, \tag{1.9}$$

where τ is the down-frontal wind stress ($N\ m^{-2}$) and f reperesents the Coriolis parameter where within $sin(\theta)$ dictates it as a function of latitude.

It must be noted that $\langle w\prime\, b\prime \rangle_e$ acts to restratify the ML whereas $\langle w\prime\, b\prime \rangle_{cool}$ and $\langle w\prime\, b\prime \rangle_w$ destratify the ML. The competition between these vertical fluxes establish the rate of either restratification or destratification of the ML.

If $\langle w\prime\, b\prime \rangle_e > \langle w\prime\, b\prime \rangle_{cool} + \langle w\prime\, b\prime \rangle_w$ then ML eddies win and restratification of the ML will take place, while if $\langle w\prime\, b\prime \rangle_e < \langle w\prime\, b\prime \rangle_{cool} + \langle w\prime\, b\prime \rangle_w$, the cooling effects dominate and destratification of the ML will occur.

Current observations of ML eddy restratification

This process of enhanced stratification due to ML eddies can cause significant shoaling of the MLD with growth scales of the order of a day to weeks (Fox-Kemper et al., 2008; Mahadevan et al., 2012b) and have shown to be ubiquitous at mesoscale fronts due to the large horizontal density gradients present (Pasquero et al., 2005). Although the concept of ML eddy restratification was developed in models (Fox-Kemper et al., 2008), recent observations have shown that a springtime restratification of the MLD in the North Atlantic (Taylor and Ferrari, 2011; Mahadevan et al., 2012b) and the Mediterranean (Olita et al., 2014) are a result of ML eddy overturning at lateral density fronts, causing phytoplankton growth before the onset of seasonal summer stratification. Our understanding of this process is therefore critical in

estimating the phytoplankton budget. Increased observations in the global ocean of ML eddy overturning are required to improve our predictions in climate models, but until now these observations at these required space and time scales have been missing in the Southern Ocean.

Introduction

Phytoplankton growth in the Southern Ocean is considered a globally important process in the mitigation of climate change, accounting for around a third of the total global carbon flux (Schlitzer, 2002). Within the Southern Ocean, different zones separate different regimes in phytoplankton biomass, where SAZ is the largest contributor to the Southern Ocean biological cycle (Thomalla et al., 2011). The strongest mode of variability in the SAZ is characterised as the seasonal cycle of linking climate forcing and primary production (Monteiro et al., 2011). In winter, strong atmospheric cooling and winds generate deep mixing, carrying phytoplankton cells below the light level and inhibiting phytoplankton growth (Boyd et al., 1999). The springtime increase of light combined with weaker surface forcing reduces the depth of turbulent mixing and allows the phytoplankton to be trapped into the light level for longer periods, promoting photosynthesis and leading to phytoplankton blooms (Sverdrup, 1953).

Fundamental to our understanding of these blooms is determining the drivers of the MLD. The MLD is primarily controlled by the vertical density stratification, where a stronger gradient suppresses turbulence and constrains mixing. Fluxes of the MLD are controlled by effects that deepen it, such as strong winds and surface cooling directing an air-sea interaction that drives momentum into the ocean, inducing convection (Sallée et al., 2010). Conversely, surface heating and precipitation result in a positive buoyancy at the ocean surface, increasing stratification. Developments in model studies (*e.g.* Thomas and Lee, 2005; Boccaletti et al., 2007) have shown that the role of lateral density gradients are important in determining MLD budgets. Consider a large scale density front, such as those observed in the Southern Ocean (Orsi et al., 1995). After the passing of a storm the MLD deepens, erasing vertical stratification but not the horizontal. The front undergoes geostrophic adjustment (Tandon and Garrett, 1994), eventually becoming unstable and generating meanders, where baroclinic instabilities develop energetic ML eddies of size 1-10 km and as deep as the MLD (Fox-Kemper et al., 2008). The ML eddies want to drive the net transfer of lighter water over the heavier water, generating a ML eddy-overturning circulation and thereby restratifying the MLD (Mahadevan et al., 2010). This process of restratification can be opposed or enhanced due to the affects of wind stress acting either in the direction of the geostrophic flow of the front (down-front) or

against it (up-front). It follows this example: in the Southern Ocean, denser waters lie southward toward Antarctica with lighter waters situated equatorward. The prominent westerly winds (Trenberth et al., 1990) acting in a down-frontal direction to the mean flow with surface Ekman transport normal and to the left of the wind in the Southern Hemisphere (Ekman, 1962) result in a northward advection of heavier water over lighter water promoting convective overturning and destratifying the ML. Conversely, as the wind direction reverses to up-front of the mean flow (easterly winds over the Southern Ocean), a capping of lighter water over heavier water will promote restratification. Global observations of ML eddy restratification have been limited, owing to their small spatial scales and evolutionary time scales of a few days (Fox-Kemper et al., 2008). However, recent studies in the North Atlantic (Mahadevan et al., 2012b) and Meditteranean (Olita et al., 2014) have found that ML eddies are able to generate early springtime restratification of the ML, enhancing phytoplankton growth. Nevertheless, observations in the Southern Ocean have been limited to a study by Swart et al. (2014), who observed the ML eddies at the same time the primary productivity increased. There is still an urgent need to apply the parameterisations developed by Fox-Kemper et al. (2008) to the Southern Ocean, where there is a great deal of temporal and spatial inconsistencies in the timing of springtime phytoplankton growth (Thomalla et al., 2011).

Furthermore, Fauchereau et al. (2011) showed that MLD changes in the Southern Ocean during summertime are well fitted to transient wind events on a sub-seasonal scale. Their study links MLD deepening events to increases in phytoplankton growth, inferring the injection of Fe into the ML and thereby sustaining productivity. This is supported by Swart et al. (2014), who observed sustained summer blooms in the SAZ that correlated to storm events occurring at periods of between 4 to 9 days. These studies have highlighted the importance of coupling sub-seasonal atmospheric variability to enhanced productivity, which therefore have important implications for physical-biological model projections.

The above findings indicate a need for determining the physical drivers of MLD variability in the SAZ during the springtime restratification period and quantifying the sensitivity of the coupling between wind forcing and MLD deepening in the SAZ summer regime.

2.1 Aims and Questions

This project falls under the framework of the Southern Ocean Seasonal Cycle Experiment (SOSCEx). The aim of SOSCEx is to build a seasonal cycle of high-resolution physical and biogeochemical measurements to understand the response of the biological productivity to physical forcing mechanisms on timescales of inter-annual, seasonal and sub-mesoscale (Swart et al., 2012).

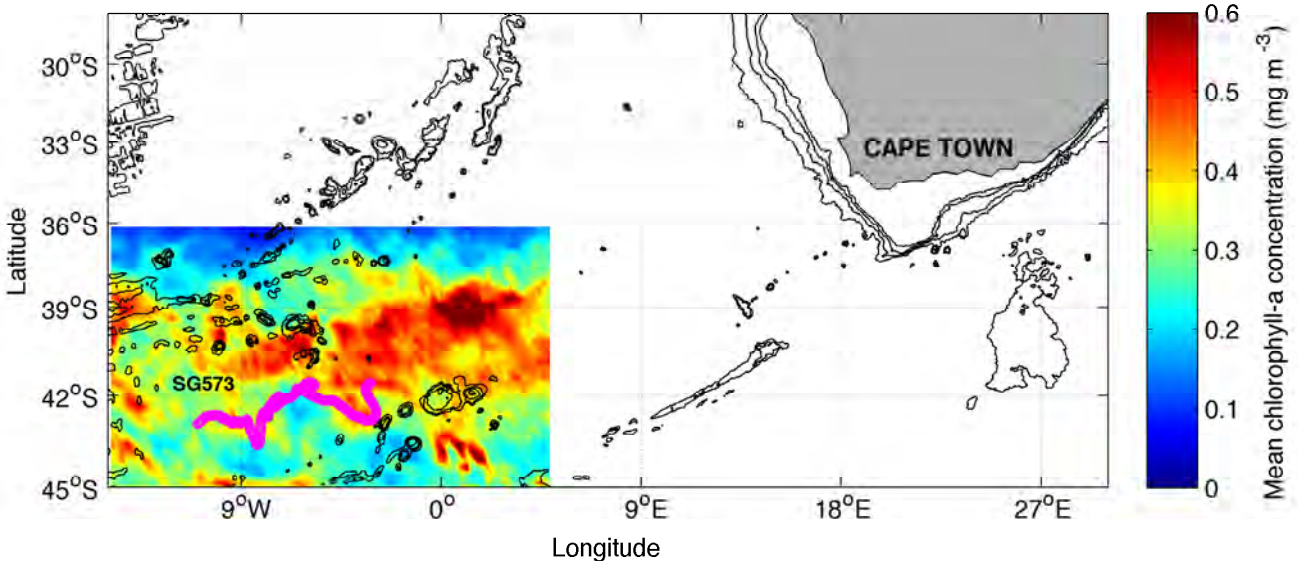

Figure 2.1: Trajectory covered by Seaglider 573 (SG573) for the duration of SOSCEx (25 September 2012 - 15 February 2013) is indicated by the magenta line. Colour shows the mean surface cholrophyll-a concentrations ($mg\ m^{-3}$) during the period of SOSCEx acquired from the GlobColour project. Black lines indicate the bathymetry determined from the ETOPO1 dataset. Figure adapted from Swart et al. (2014).

As a part of SOSCEx, an autonomous ocean Seaglider 573 (SG573) continually sampled the SAZ south-west of Africa (Figure 2.1) (41° S to 44° S) from the ocean surface to a depth of 1000 m for 5.5 months (25 September 2012 - 15 February 2013). The experiment managed to successfully capture spring and summertime phytoplankton blooms (colour scheme in Figure 2.1), suggesting that the physical drivers underlying MLD variability that are important for phytoplankton growth in the SAZ can now be examined.

This study investigates two particular questions:

1. Do ML eddies drive springtime restratification in the SAZ?

Studies in the North Atlantic show that lateral buoyancy gradients at the ocean surface become unstable and grow into sub-mesoscale ML eddies (Mahadevan et al., 2012b). Parameterisation of the overturning flux of these ML eddies has shown to be successful in reporting the restratifying of the springtime MLD before solar-induced stratification, initiating phytoplankton blooms that are likely to be an important contribution to the total oceanic phytoplankton production.

In answering this question the index of the stratification (N^2), MLD and lateral buoyancy gradients in combination with upper ocean ML hydrographic properties are determined from the springtime SG573 dataset and analysed in conjunction with satellite atmospheric parameters of heat flux and wind stress. To test the presence of sub-mesoscale overturning features at lateral buoyancy fronts, the competition between ML eddy restratification and destratifying atmospheric mechanisms are applied whereby significant events in MLD variability occur.

2. At what sub-seasonal temporal scales do wind forcing and deepening of the MLD couple? Is there a quantified relationship between the two?

During summertime in the SAZ region, when nutrients within the ML become depleted from biogeochemical productivity, the coupling effect of transient wind events and deepening of the MLD over sub-seasonal scales has been shown to result in favourable bursts of phytoplankton growth (Swart et al., 2014). Part of this study will apply statistical analysis to derive a relationship between wind events and variability of the MLD at the sub-seasonal scales. By addressing this question, the contribution of sub-seasonal winds to MLD variability can be determined. This is particularly important as changes in climate can have altering effects on the ML physics with knock-on effects to biological processes.

Data and Methods

3.1 Sampling with a Seaglider

The Seaglider 573 (SG573) used in this study is an autonomous vehicle of length 1.2 m and weight 52 kg (Figure 3.1). It glides in a V-shaped sawtooth pattern from the surface ocean to a programmed depth of 1000 m and back to the surface with an average horizontal velocity for this study of 0.33 $m\ s^{-1}$ and vertical velocity of 0.1 $m\ s^{-1}$.

It is driven by its own buoyancy by pumping hydraulic oil between internal and external bladders, allowing it to move up and down. The angle of the glider wings determines the horizontal distance the glider will travel, which is dependent on the target position programmed to it. Between the dive cycles, the glider uses Iridium satellites to communicate to the base station, downloading the data collected from the previous dive as well as attaining a target location for the following dive to the shore-based basestation (Eriksen et al., 2001).

The Seaglider platform has previously been used to sample high-resolution scales of ML variability that relate to biogeochemical production (Sackmann et al., 2008; Frajka-Williams et al., 2009; Lee et al., 2011; Perry et al., 2008). It is becoming a useful platform in determining high spatial and temporal scales of MLD variability (less than 10 km within a few hours) (Eriksen et al., 2001). This is in contrast to traditional measuring platforms of Argo floats which profile every 10 days and ship measurements which have a spatial resolution of over 20 km.

On 25 September 2012, SG573 was deployed south of Gough Island in the Atlantic sector of the Southern Ocean at 42.9° S, 11° W and retrieved on 15 February 2013 at 41.6° S, 3.2° W, spending a total of 143 days in the SAZ (Figure 3.2, see Swart et al. (2014)). A Sea-Bird Electronics SBE41 unpumped conductivity (salinity), temperature and depth profiler (CT-Sail) sampled continuously at a nominal vertical velocity rate of 1 $m\ s^{-1}$ with an average rate of 0.2 Hz, attaining to a vertical resolution of <1 m.

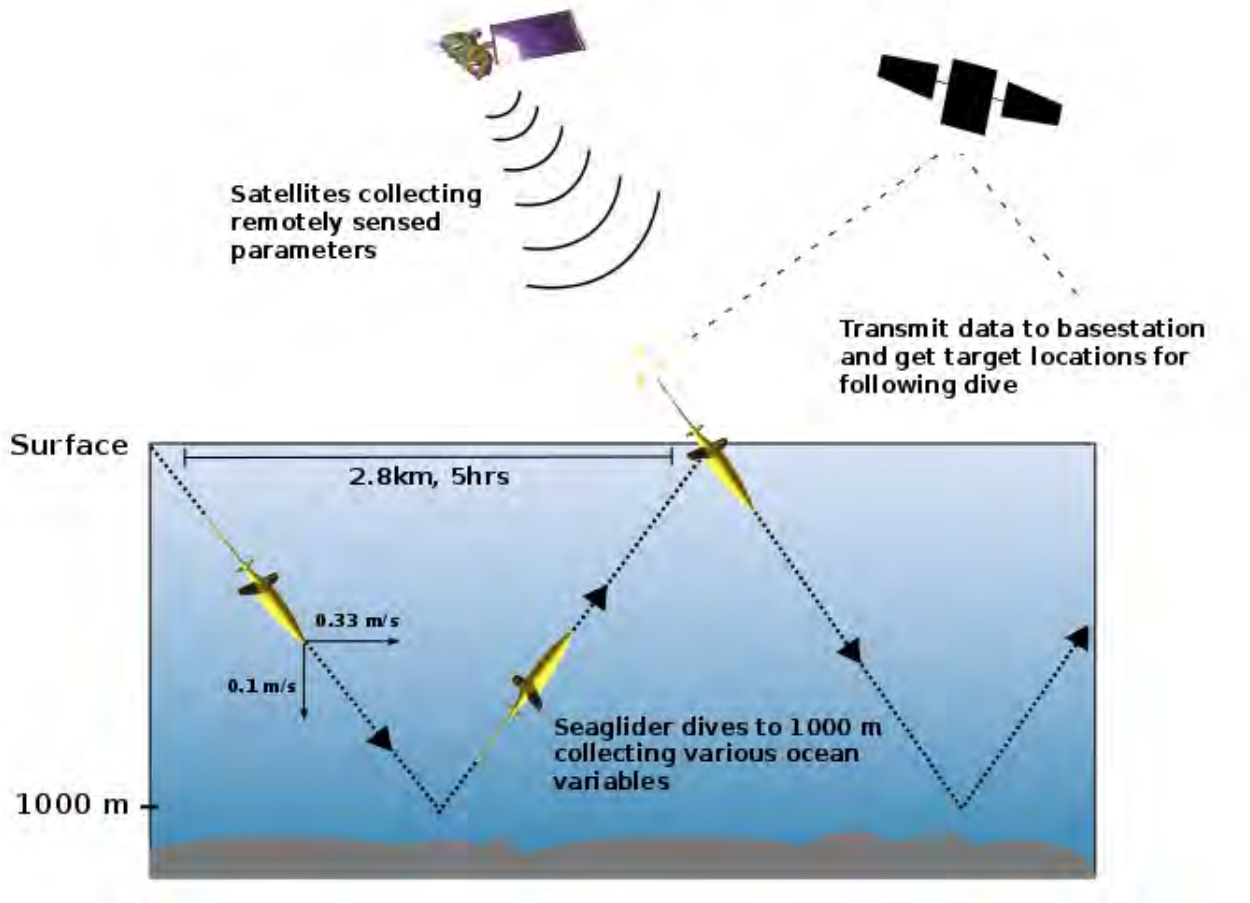

Figure 3.1: Schematic indicating sawtooth diving pattern of the Seaglider. SG573 dove continuously from the surface to 1000 m and back, collecting variables at 0.2 Hz with an average horizontal length resolution of 2.8 km and temporal resolution of 5 hours between dives. At the surface, SG573 transmitted to the base station via Iridium satellite and got target locations for the next dive. Simultaneously satellites collected remotely sensed data over the same location as SG573.

The fluid flow connecting the temperature and conductivity sensor using the unpumped CT-Sail relies on the Seaglider's propulsion and thus thermal-inertia effects arise as the speed of the Seaglider is not consistent. In addition, large vertical gradients in temperature occur such as at the thermocline where inconsistencies between the measured temperature of the thermistor and the actual temperature at the conductivity cell differ. This can offset calculated salinity from the true value. Such an issue can vary in time as during summer periods the effect of solar heating on the surface of the ocean generates stronger vertical temperature gradients. To correct this, an effective water temperature inside the conductivity tube is com-

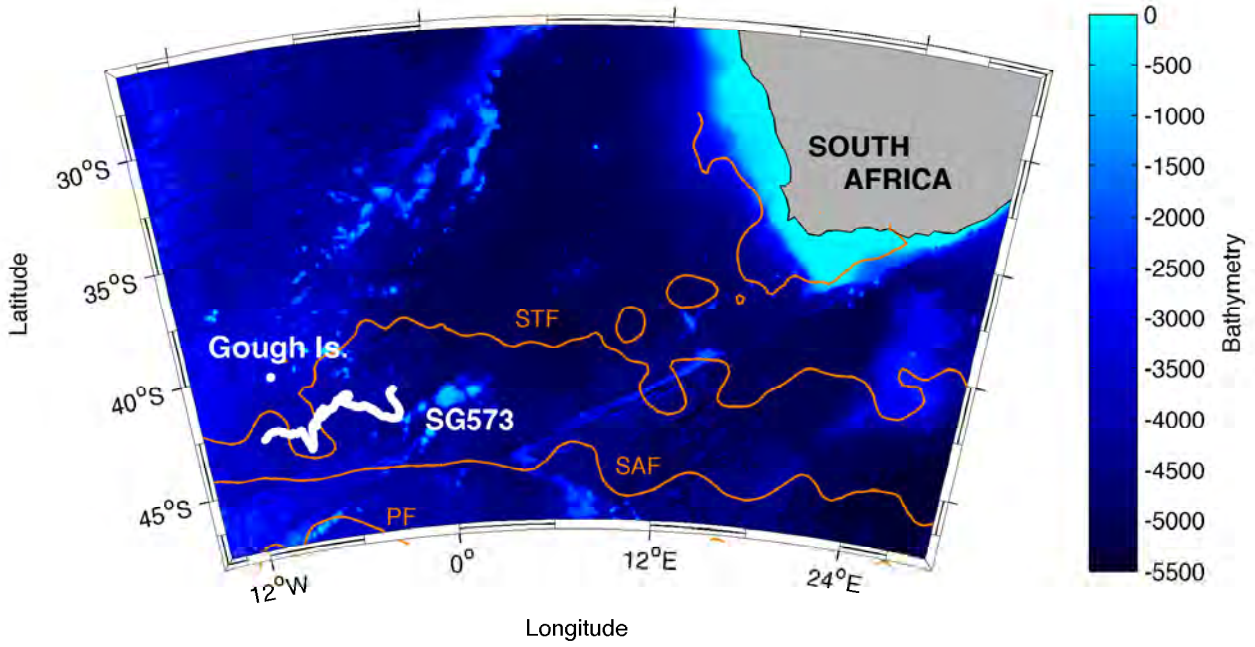

Figure 3.2: White line shows the trajectory of SG573 during SOSCEx. Colour indicates bathymetry (in metres below sea level) using the ETOPO1 dataset. Mean surface frontal locations during SOSCEx determined from satellite altimetry are drawn in orange and show the STF, SAF and PF.

puted based on the tube's thermal response to the changes in measured temperature outside the tube and the estimated flow through the tube, yielding a corrected salinity derived from the associated conductivity measurement (Eriksen et al., 2001). At both the deployment and retrieval sites, collaboration casts using a ship-board CTD notice a conductivity sensor drift of 0.03, which has been corrected for by Swart et al. (2014) (Figure 3.3). The density is then determined using the corrected salinities.

The mean lateral distance between dive cycles is 2.8 km, which measures up to 1.4 km per profile, totalling 1212 profiles. The mean temporal resolution between the profiles is 2.5 hours. Using a linear interpolation, the profiles were adjusted to a 6-hourly time step in order to be comparable to 6-hourly satellite products of wind stress and heat flux. This readjusts the 1212 profiles to 571 for the period of this study with a nominal horizontal spatial resolution of 2.9 km.

In addition, an array of biological sensors were fitted to SG573 during the sampling of

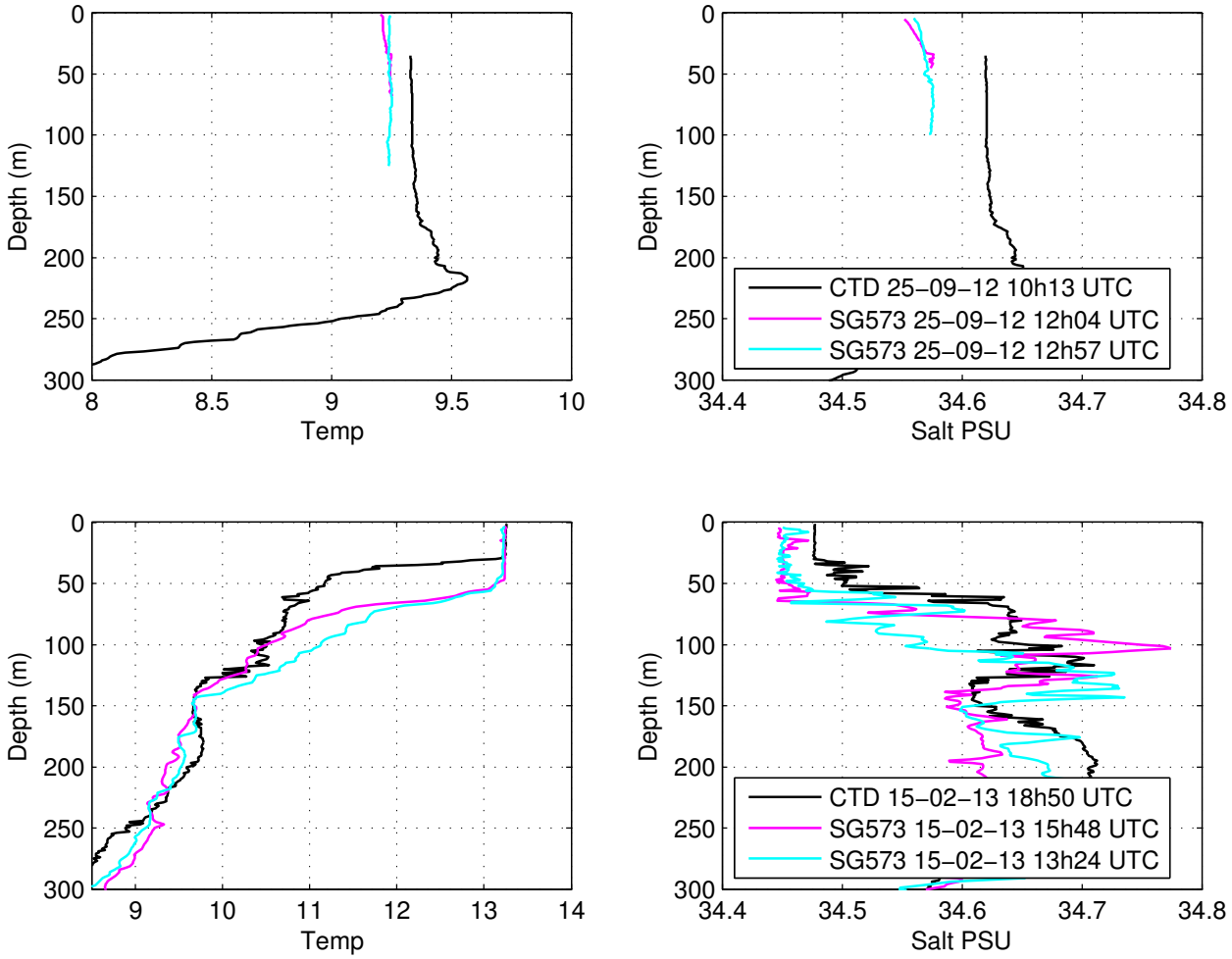

Figure 3.3: SG573 calibration casts using a ship-board CTD at deployment (a, b) and retrieval (c, d) sites. A sensor drift of the conductivity sensor realised a 0.03 offset.

SOSCEx. These include dissolved oxygen, Photosynthetically Active Radar (PAR), backscattering and chlorophyll-*a* fluorescence (*proxy* for phytoplankton production). This study will only make use of the physical parameters sampled by the CT-Sail. The results from the biogeochemistry measurements are discussed further in Swart et al. (2014).

For the final five weeks of the SOSCEx survey, SG573 experienced forms of biofouling from Goose-neck barnacles on both the fairing and the sensor platforms (Figure 3.4). Barnacle growth on the CT-Sail is believed to have restricted the flow rate through the Conductivity flow path and result in erroneous spiking in the salinity measurements that were subsequently corrected or removed from the dataset.

Figure 3.4: Goose-neck barnacles biofoul SG573 after 143 days at sea.

3.2 Determining the mixed-layer depth

A considerable amount of work has been undertaken in determining a method whereby the MLD can be accurately calculated (Brainerd and Gregg, 1995; Obata et al., 1996; Kara et al., 2000; Thomson and Fine, 2003; de Boyer Montégut et al., 2004; Dong et al., 2008). In these studies, a threshold criteria is used whereby the deviation of either temperature (ΔT) or density ($\Delta\sigma_T$) from a surface reference level with depth defines the MLD (Kara et al., 2000; de Boyer Montégut et al., 2004). A reference level is chosen due to air-sea processes generating a thin layer at the surface usually 1-2 m deep (Price et al., 1986) whereby a strong vertical gradient in physical ocean properties erroneously triggers the MLD. Numerous criteria have been proposed as the recommended MLD threshold (Table 3.1).

The density criteria is considered the robust determination of the MLD as vertical gradients in the density defines the pycnocline. However, there are cases whereby changes in both density and/or temperature determine the MLD, which is useful when salinity measurements are unavailable or erroneous.

Dong et al. (2008) performed a study to estimate the MLD for the Southern Ocean and found that in almost all regions north of ~50° S, the density and temperature criteria defined

Study and Region	MLD Threshold Criterion	Reference Level	Method used
de Boyer Montégut et al., 2004, global	$\Delta T = 0.2\ ^{\circ}C$, $\Delta\sigma_T = 0.03\ kg\ m^{-3}$	10 m	observations of 4, 490, 571 profiles
Brainerd and Gregg, 1995, Pacific Ocean	$\Delta\sigma_T = 0.05$ to $0.05\ kg\ m^{-3}$	0 m	observations of overturning length scale
Obata et al., 1996, Global Ocean	$\Delta T = 0.5\ ^{\circ}C$	0 m	arbitrary
Kara et al., 2000, Global Ocean	$\Delta T = 0.8\ ^{\circ}C$	10 m	comparison of ocean weather stations and *World Ocean Atlas*
Thomson and Fine, 2003, North Pacific	$\Delta\sigma_T = 0.01$ to $0.03\ kg\ m^{-3}$	2.5 m	arbitrary

Table 3.1: Examples of criterion for determining the MLD based on a threshold method whereby a change in temperature (ΔT) or density ($\Delta\sigma_T$) relative to a defined reference level.

by de Boyer Montégut et al. (2004) of $\Delta\sigma_T = 0.03\ kg\ m^{-3}$ and $\Delta T = 0.2\ ^{\circ}C$ compare well. This is due to the thermal control on the mixing depth generated by the strong thermocline. Dong et al. (2008) therefore imply that using the temperature criteria of $\Delta T = 0.2\ ^{\circ}C$ from a surface reference level of 20 m is an adequate representation for the MLD north of ~50° S.

Therefore, the MLD threshold used in this study will follow the de Boyer Montégut et al. (2004) temperature criterion whereby a deviation of the temperature by 0.2 $^{\circ}C$ from a reference depth of 10 m denotes the MLD ($\Delta T_{10m} = 0.2\ ^{\circ}C$). This is undertaken for two reasons:

1. A thermal lag error related to the umpumped CT-Sail installed on SG573 (Figure 3.5) has the temperature sensor positioned beneath and parallel to the conductivity sensor. The conductivity sensor is placed within a metal guard with holes that allow water to flow through (Figure 3.5) (Janzen and Creed, 2011).

The two sensors are not connected, therefore it cannot be guaranteed that they will be measuring the same seawater sample as water is allowed to flow freely between the two sensors. The thermal lag error occurs when water in the conductivity cell is not flushed out completely but rather recirculated, hence altering the conductivity of the following water sample measurement. This has been shown to cause spikes in the salinity measurements (Garau et al.,

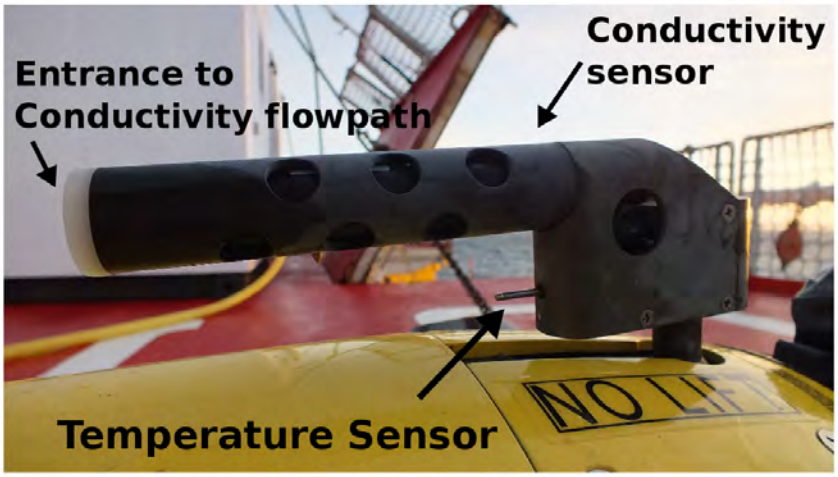

Figure 3.5: Integrated CT-Sail on board SG573. Temperature sensor situated below and parallel to the conductivity sensor.

2011),

2. The bio-fouling (Figure 3.4) around the CT-Sail during the final five weeks of sampling lead to erroneous salinity measurements. Additionally, a recent study using this dataset successfully applied the criteria of $\Delta T_{10m} = 0.2\ ^{\circ}C$ (Swart et al., 2014).

3.3 Satellite products

3.3.1 Winds

The wind data used in this study originates from a SeaWinds blended vector sea surface winds (at 10 m above sea level reference height) product comprising of a combination of observations from up to six satellites, including Scatterometers (QuikSCAT), SSMIs, TMI and AMSR-E (Zhang et al., 2006, ftp://eclipse.ncdc.noaa.gov/pub/seawinds/). The amalgamation produces a gridded-field of a 6-hourly product with a 0.25° resolution (∼28 km) and four instantaneous global snapshots per day at UTC/GMT 00, 06, 12 and 18Z. A bi-linear interpolation was performed on the glider locations to attain the wind speed values for each glider

location, whereby the Large and Pond (1981) method was applied to convert the wind speed to a wind stress product.

3.3.2 Sea surface temperature (SST)

The Operational Sea Surface and Sea Ice Analysis (OSTIA) Level 4 product is used for SSTs during this study. OSTIA uses optimal interpolation from a combination of satellites (AMSR-E, AATSR, SEVIRI, AVHRR-3, TMI) from the Global High Resolution Sea Surface Temperature (GHRSST) project in addition to *in-situ* observations (Donlon et al., 2012) to produce daily SST product on a 0.054° resolution grid (∼5 km) (http://podaac.jpl.nasa.gov/dataset/UKMO-L4HRfnd-GLOB-OSTIA).

3.3.3 Altimetry

The 'Maps of Absolute Dynamic Topography' (MADT) shows the surface altimetry determined by the sea level anomaly added to the mean dynamic topography. It represents the density structure of the full water column as *dynamic m* (*e.g.* an increase in the MADT typically representing a decrease in the integrated density throughout the water column). The MADT is a CLS/AVISO product obtained from JASON-1, ENVISAT, ERS and TOPEX/POSIEDON satellites. Daily snapshots of the sea state are given on a 0.25° resolution grid (∼28 km) (http://www.aviso.altimetry.fr).

3.3.4 Surface currents

The Ocean Surface Current Analysis Real-time (OSCAR) provides a Level 4 0.33° resolution (∼37 km) near-surface horizontal velocity field estimated from 18 SSH, surface vector wind and SST satellites, including ENVISAT, AVHRR-3, JASON-1, ERS-1/ERS-2 ALTIMETER and TOPEX-POSEIDON (http://podaac.jpl.nasa.gov/dataset/OSCAR_L4_OC_third-deg) (Bonjean and Lagerloef, 2002). The velocities are calculated from a quasi-geostrophic model in addition to an eddy viscosity based wind-driven ageostrophic component and a thermal wind adjustment. The model produces an average current for the top 30 m of the ocean

at 5-day intervals.

3.3.5 Heat fluxes

The National Centre for Environmental Prediction, NCEP/DOE AMIP-II Reanalysis (Reanalysis-2) provides 6-hourly averages for products of incoming shortwave (Q_S), outgoing longwave (Q_L), latent heat (Q_{lat}) and sensible heat (Q_{sens}) fluxes, from which $Q_{net} = (Q_S) + (Q_L) + (Q_{lat}) + (Q_{sens})$ at a 1.9° resolution (∼210 km) (http://www.esrl.noaa.gov). Typically $(Q_S) > 0\ W\ m^{-2} > (Q_L)$, (Q_{lat}) and (Q_{sens}).

3.4 Statistical methods

3.4.1 Multi-taper spectral analysis

A Multi-taper spectral analysis using a density spectrum presented on a logarithmic scale illustrates a wide range of spatial variability, especially at the higher frequencies. Generally, the range spans shallow slopes of high wavenumbers and decreasing horizontal resolution associated with steeper slopes. Decreasing spectrum slope angles from -3 to $-5/3$ display an increase in the horizontal resolution as an intensification of the transition from mesoscale towards the sub-mesoscale occurs (Capet et al., 2008). Application of a Multi-taper spectral analysis to the near-surface density reveals the horizontal scales of density structures that are accurately captured by glider measurements.

3.4.2 Deriving buoyancy gradients

The lateral buoyancy gradients for this study are computed using the mean distance between all profiles from the glider dataset (2.9 km). This is due to the lateral inconsistency related to glider measurements (range: 0.2-7.2 km). By averaging the distance between profiles, the determination of the b_{xy} is not biased with respect to the spatial variability between dives. This allows the b_{xy} to be a function of the strength of the lateral gradient in buoyancy

only.

3.4.3 Empirical Mode Decomposition

An Empirical Mode Decomposition (EMD) is a function that decomposes a signal into a series of primary signals called Intrinsic Mode Functions (IMFs) (Rato et al., 2008). It performs a spectral analysis using the Hilbert transform followed by an instantaneous frequency computation (Huang et al., 1998). Here, EMDs are used to find similar modes of variability by decomposing the MLD, wind stress and Q_{net} into a number of different frequencies (IMFs) relating to each respective signal. Each of the IMFs are used to analyse different temporal modes of variability by averaging the time between peaks of each IMF. The EMD calculations are acquired from the MATLAB function $rParabEmd\_\_L$, based on Rato et al. (2008).

3.4.4 Correlating the wind and MLD variability

Correlation statistics are used in this study to define how well wind stress variability explains the MLD variability, following Equation 3.1:

$$r = \frac{1}{N-1}\sum_{t=1}^{N}\frac{(x(t)-\bar{x})}{\sigma_x} \times \frac{(y(t)-\bar{y})}{\sigma_y}, \tag{3.1}$$

where x and y represent two different time series, N is the total number of samples for x and y and t is the time step = 1.

A Student T-test is performed on the correlation to determine whether the two variables concerned are significantly correlated. This occurs when the absolute value of Equation 3.2 is larger than the absolute value of the inverse of the Student's T cumulative distribution function.

$$t = \frac{r\sqrt{n-2}}{\sqrt{1-r^2}}, \tag{3.2}$$

where t is the Student T-test value, r is the correlation and n is the number of samples. If the correlation between the two variable is significant to the 99% level, the square of the

correlation co-efficient (r^2) explains the amount of variance given between two variables.

Results

4.1 A seasonal setting

4.1.1 The SAZ ML

The broader seasonal setting of this study with respect to the seasonal SAZ MLD is determined by overlaying the MLD derived from Argo float profiles for an entire season with the glider MLDs of this study (Figure 4.1A). This presents a larger temporal picture of the sampling period with respect to the seasonal cycle of the MLD. A direct comparison of the two MLD products immediately indicates that the glider MLDs are shallower than the MLDs computed from the ARGO floats.

A likely reasoning for this is that the vertical resolution of the ARGO floats is in 10 m intervals, while the glider follows a 1 m resolution. The 10 m resolution allows for smoothing of parameters in each bin, reducing the vertical gradient and thus simulating a weaker thermocline than that which the glider measures. Although this generates a deeper than normal MLD, it does not misrepresent its seasonal variability and thus it is used to compare the seasonal progression of the glider MLD with that of the full season of ARGO MLDs. The Argo MLD presents the full grasp of the seasonal cycle, showing maximum MLDs in August/September (MLD >200 m), which shoal to a minimum in January/February (MLD <100 m). The glider MLDs indicate that the sampling period successfully captures the bulk of the MLD shoaling period in addition to over 2 months of shallow summer MLDs. A visual comparison between the Argo MLD dataset and the net incoming heat flux during the period of glider sampling suggests that the seasonal increase in heat flux is responsible for the seasonal shoaling of the MLD. However, the considerably high frequency variability captured by the glider suggests otherwise. For instance, variability in the glider MLD ranges from a minimum of 12 m to a maximum of 272 m with rates of restratification (shoaling of the MLD) >100 $m\ day^{-1}$. In almost all cases of restratification, the MLD shoals to ∼20 m, implying an increase of temperature by 0.2 $^{\circ}C$ within that depth. The amount of heat required to enter the ocean in order to heat the top 20 m of 1 m^2 in 1 day by 0.2 $^{\circ}C$ can be calculated through

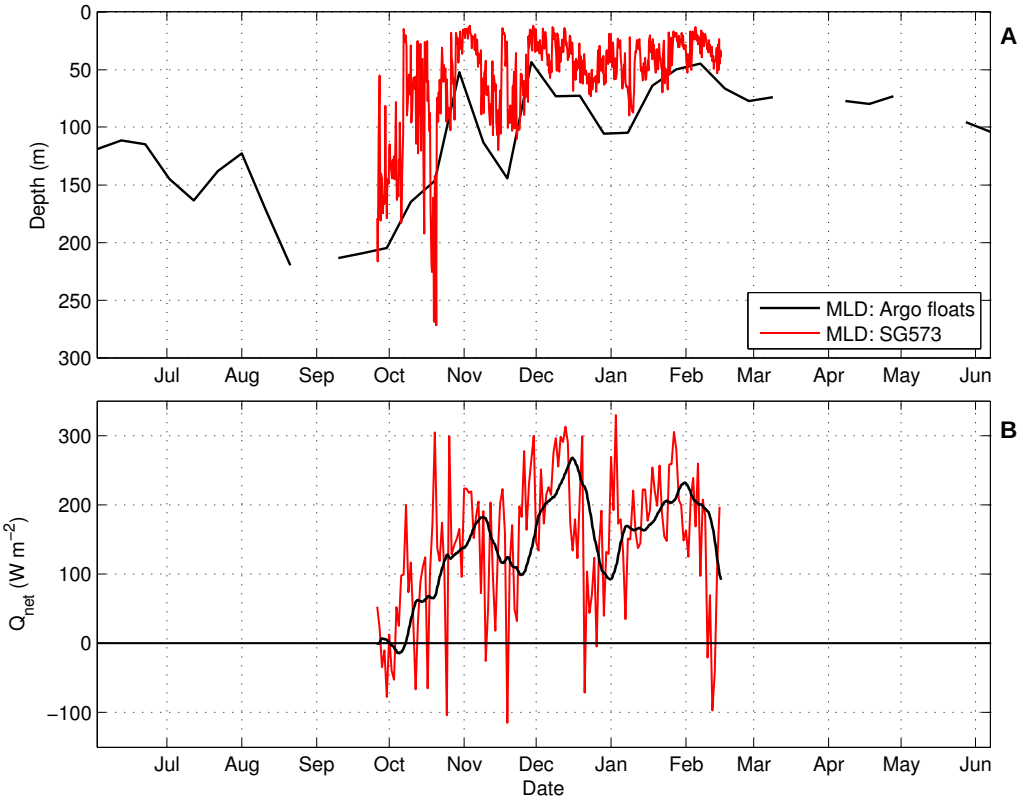

Figure 4.1: A) MLDs (m) determined from Argo float profiles for June 2012 to June 2013 encompassing the region 41° S - 44° S and 2° W - 12° W shown in black line. MLDs (m) from SG573 for SOSCEx shown by red line. B) Red line indicates Q_{net} for the location of each SG573 profile while black line overlaid is a low-pass Butterworth filter applied to show the progressive increase of Q_{net}. Black horizontal line indicates divide between the ocean gaining heat (positive) and the ocean losing heat (negative).

the application of the energy flux Equation (4.1) below,

$$Energy\ Flux = \frac{\pi\, r^2\, z\, \rho\, C_p\, \Delta T}{area\ time} \tag{4.1}$$

where r^2 is the radius of area studied, z is the depth of the heated area (20 m), ρ is the density of the seawater sample ($kg\ m^{-3}$), C_p the specific heat capacity of sea water at constant pressure (3988 $J/kg/^{\circ}K$) and ΔT is the change in temperature required (0.2 $^{\circ}C$). Area is in m^2 and time in seconds.

A positive incoming heat flux would need to be 595 $W\ m^{-2}$ for one full day. Figure 4.1B indicates that this is not the case and thus infers that there are alternative physical dynamics that determine the springtime restratification of the MLD.

Around half way through the glider sampling period, the seasonal cycle of the MLD shifts from the highly variable springtime (12 - 272 m) to consistently shallow (<100 m) during summer. Hydrographic variables of density, temperature and salinity as well as the vertical stratification measure N^2 indicate the reason for this. The seasonal contrast of MLD behaviour is a direct result of the disparity in the seasonal upper ocean physics (Figure 4.2).

The spring period is characterised by mesoscale structures associated with large ML variability in both temperature (∼8.5 - 11 $°C$) and salinity (34.3 - 34.8), while the summer hydrography exhibits an abrupt increase in the temperature of the top 100 m by 2 $°C$ associated with a strengthening of the pycnocline (N^2) (Figure 4.2).

Hovmöller diagrams illustrate the seasonal evolution with latitudinal space for the MADT and the SST over the period of SOSCEx (Figure 4.3).

Figure 4.3A illustrates the mesoscale variability in the form of deviations of MADT associated with shifts in the vertical density structure. A prominent cyclonic feature is crossed during the first two weeks of deployment with other noticeable lateral gradients in MADT sampled during the duration of the study. Figure 4.3B displays the seasonal southward warming of the surface ocean. The point in time where the southward shift in positive buoyancy forcing 'meets' the glider is considered to be when the summer period of the study starts. The exact date of this transition in season is discussed in the following section.

4.1.2 The onset of summer determined from upper ocean physics

Identifying the split between spring and summer in the dataset is necessary as it defines the point of the seasonal transition of upper ocean hydrography, allowing for separate analysis.

This point is considered to be when ML stratification is initiated by the seasonal warming of the surface waters. On 28 November, a band of stratification develops <50 m and strengthens between 50 and 150 m with the progression into summer. From this date, general deviations

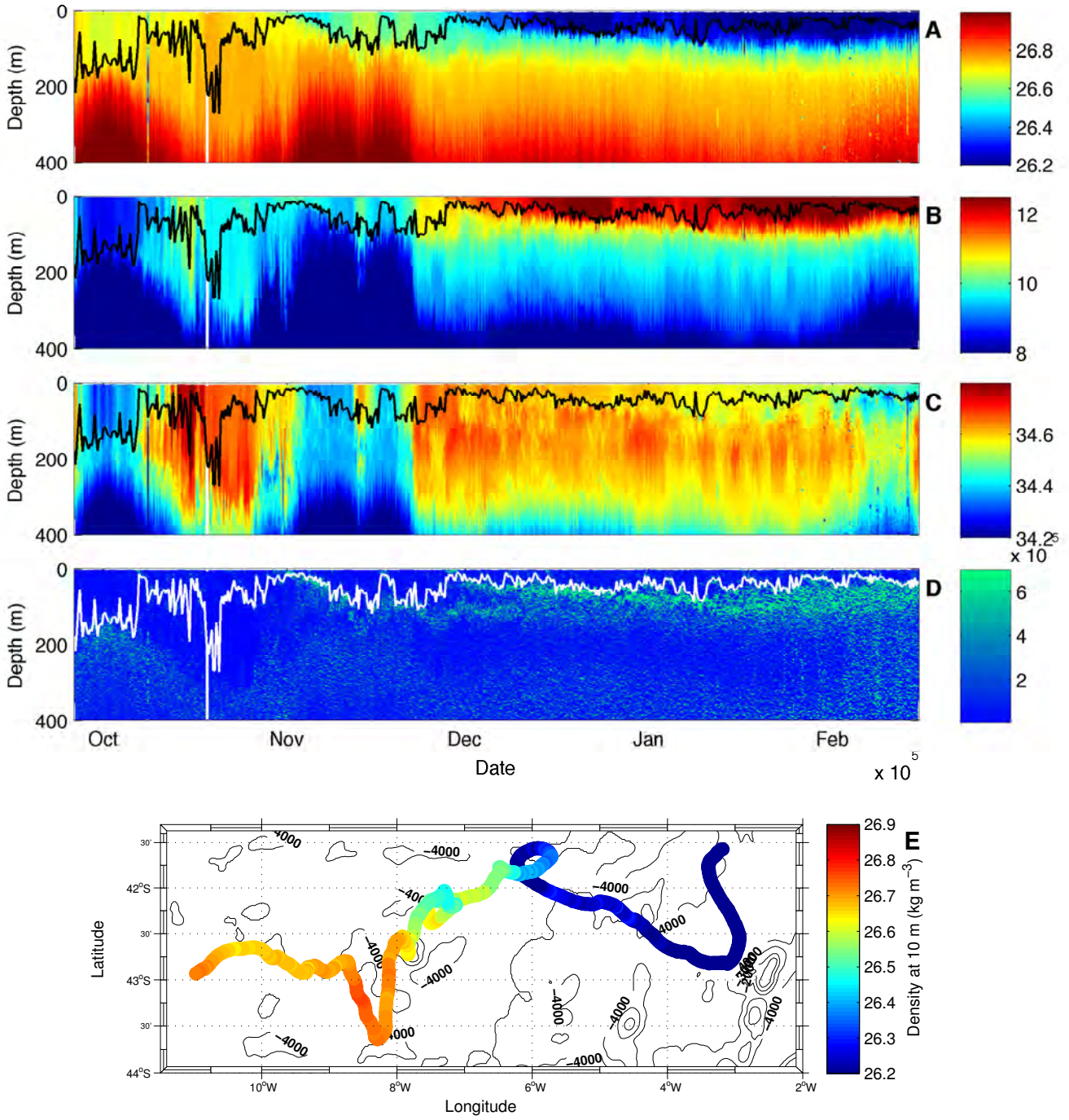

Figure 4.2: Sections of A) density ($kg\,m^{-3}$), B) temperature ($^{\circ}C$), C) salinity and D) Brunt-Väisälä frequency (N^2) for the upper 400 m from SG573. The MLD (m) is overlaid in black for A, B, C and in white for D. E) SG573 trajectory with colour indicating the 10 m density for the same period.

in the N^2_{0-100m} occur synonymously with a warming and cooling of the T_{5m} (Figure 4.4A).

This agreement is considered to arise as a result of the strengthening of the thermocline

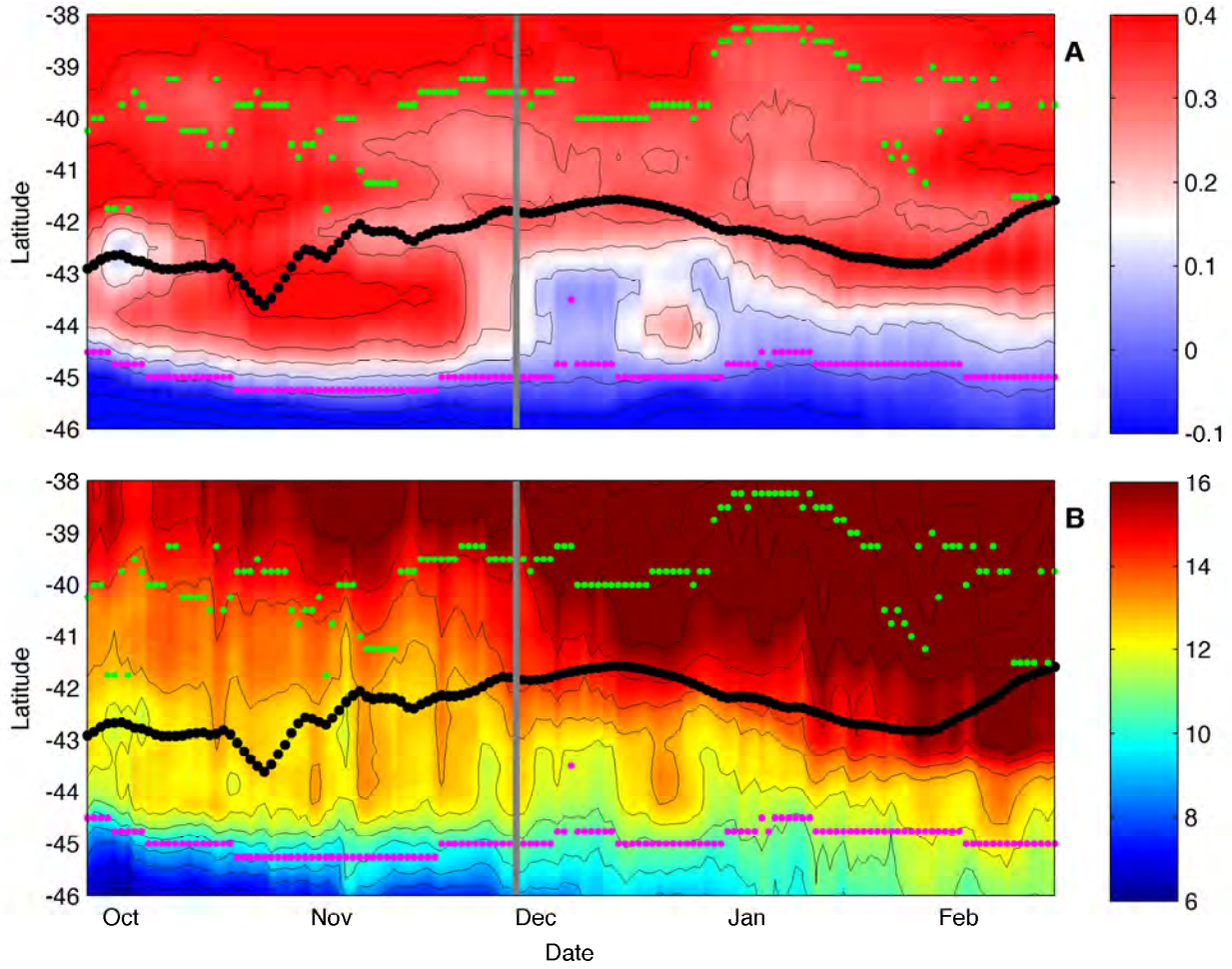

Figure 4.3: Hovmöller diagrams illustrating the temporal evolution of A) satellite altimetry (*dynamic m*) and B) SST ($^{\circ}C$) for the latitudinal extent 38° S - 46° S for the period of SOSCEx. Black dots indicate latitudinal location of SG573. Green dots show location of STF, while magenta dots show location of SAF. Grey lines indicate the separation between spring and summer on 28 November 2012.

from spring to summer, as represented by the increase in maximum δT/δz (δz = 1 m) of the top 200 m from mostly below to above 0.1 $^{\circ}C\ m^{-1}$ (Figure 4.4B). Therefore, the onset of upper ocean thermal control on stratification due to the increase in thermocline during summer indicates the contrast of physical mechanisms that underly the MLD between spring and summer. From this point forward in the study, the dataset will be split into a spring and summer time series, where the characteristics of the each season's MLD is explored independently.

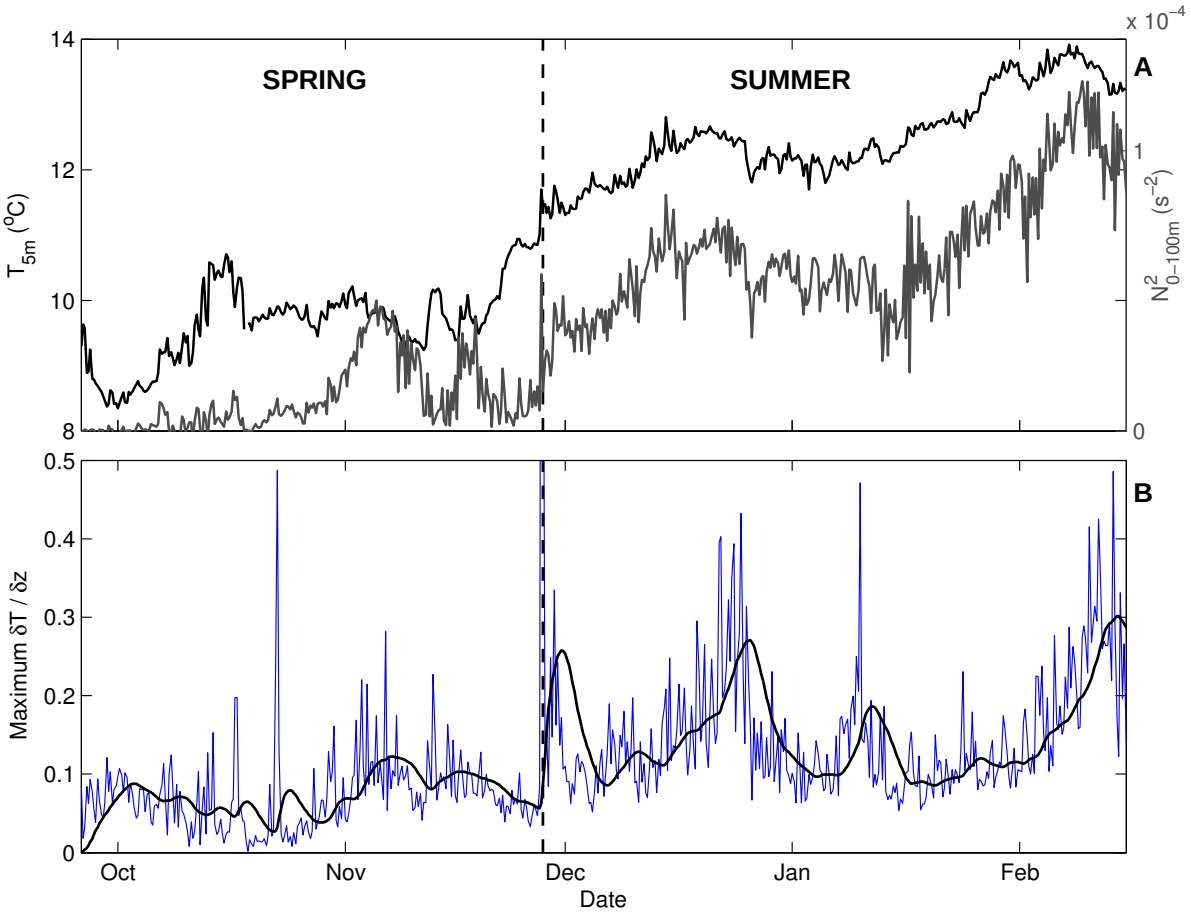

Figure 4.4: A) Temperature (°C) at 5 m depth (solid black line) with averaged Brunt-V*äisälä* frequency (N^2) of the top 100 m (grey line). B) Maximum vertical temperature gradient (δT/δz) from the surface to 200 m (blue line) with a low-pass Butterworth filter applied in black line. Dotted lines indicate seasonal split between spring and summer on 28 November.

4.1.3 Varying physical properties of the spring and summer ML

The seasonal shift in ML properties of the SAZ from spring to summer occurs when a weakly stratified ML with highly variable MLDs is suppressed in the summer by upper ocean warming. This is a product of persistent heating and increasing of the thermocline gradient. Therefore, the contrast between the ML water mass properties of spring and summer provides evidence to the seasonal depth variation of the MLD.

ML water mass properties

A temperature-salinity (T-S) diagram presenting the water mass structure of the top 500 m is plotted to show the seasonal contrast of upper ocean hydrographic properties (Figure 4.5). There are distinct seasonal differences in ML temperature and salinities. During spring, highly inconsistent ML salinities (range $\sim$0.5) strongly influence the determination of the MLDs, which occur primarily within a narrow density band of $\sim$0.2 $kg\ m^{-3}$. During summer, the salinities are comparatively constricted (range $\sim$0.2) where deviations in temperature dominate the deviations in the MLDs within a much wider density band of $\sim$0.5 $kg\ m^{-3}$. The wider density band observed during summer is a direct influence of positive surface buoyancy forcing, which decreases the ML density through heating with the progression of summer.

Comparing the MLDs

Mean seasonal profiles for both temperature and salinity provide additional insight into the MLD structure of spring and summer (Figure 4.6). The spring profiles exhibit greater vertical homogeneity than summer, with larger deviations around the mean MLD (79 $\pm$ 51 m for spring, 39 $\pm$ 16 m for summer).

Interestingly, despite the seasonal heating, variability of the spring and summer ML temperatures are similar with a spring mean of $\sim$9.7 $\pm$ 0.65 $^{\circ}C$ and summer a mean $\sim$12.6 $\pm$ 0.63 $^{\circ}C$. The analogous variability of the thermal structure in the ML during both seasons suggests that the forcing mechanisms that drive the variability are present despite the $\sim$3 $^{\circ}C$ increase in summer. However, this is not the case in the salinity profiles, where much less deviation is observed in summer (34.5 $\pm$ 0.13 in spring and 34.6 $\pm$ 0.07 in summer).

4.2 Decomposing the scales of variability observed

In the previous section, the seasonal variability of the ML hydrographic properties between spring and summer gave insight into the nature of MLD variability, with a threefold decrease from spring to summer. The rapid nature of the MLD variability with restratification rates of $>$100 $m\ day^{-1}$ indicates that there are rapid processes leading to this observed variability.

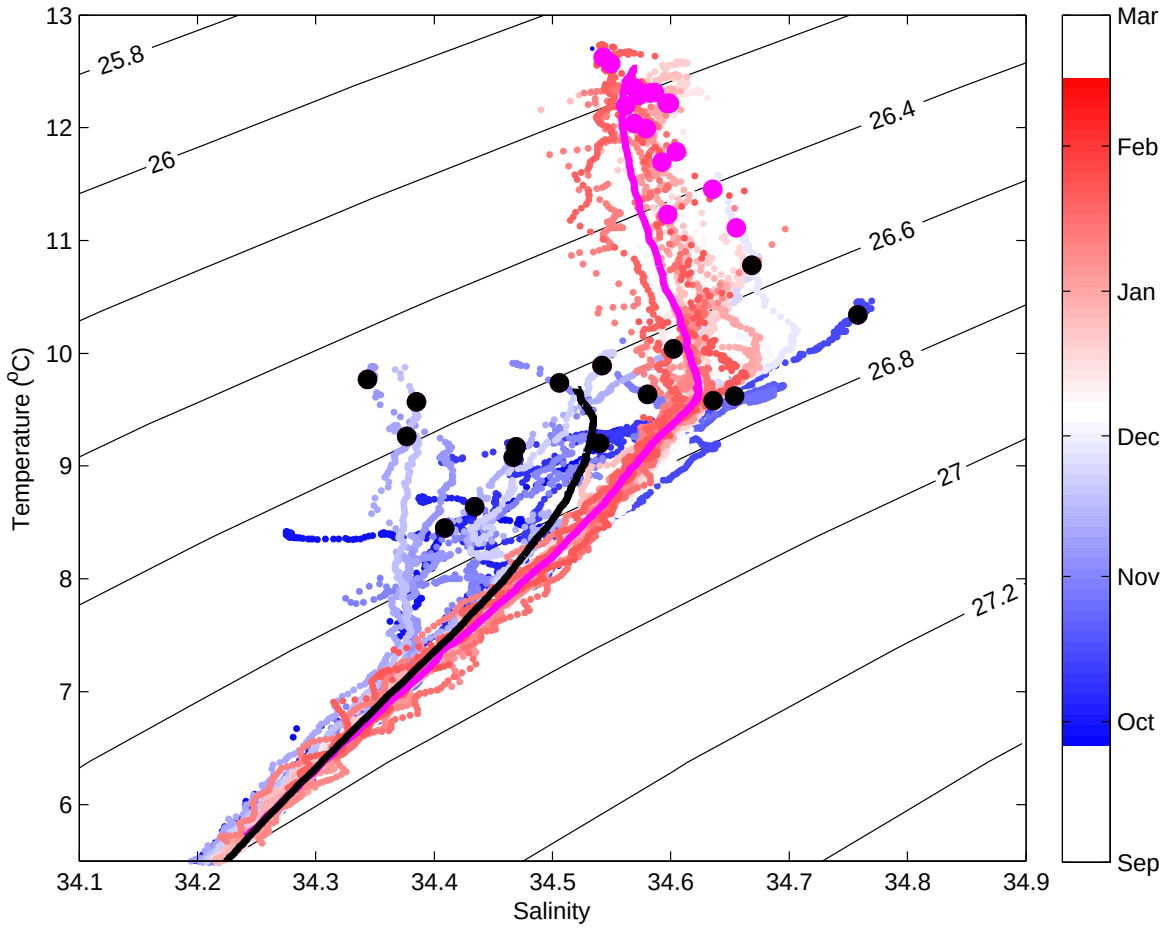

Figure 4.5: Temperature-salinity diagram taken for every 15th SG573 profile overlaid on isopycnals. The progression of blue to red profiles is representative of the spring to summer transition. Mean profiles of spring (black line) and summer (magenta line) are indicated. Black and magenta dots indicate the MLD for each respective profile. Figure adapted from Swart et al. (2014).

4.2.1 Length scale spectral analysis

A multi-taper power spectrum (in log-log space) applied to the 10 m density is used to determine the length scales of variability captured during the SG573 deployment (Figure 4.7). Reading from left to right, the initial change in slope of the spectra from the horizontal downward is observed at length scales around 1000 km, with a strong gradient slope of -3.

A levelling off of the density slope variance occurs at approximately the mesoscale (100 km), where the slope gradient begins to follow between the gradients -2 and -5/3. This level-

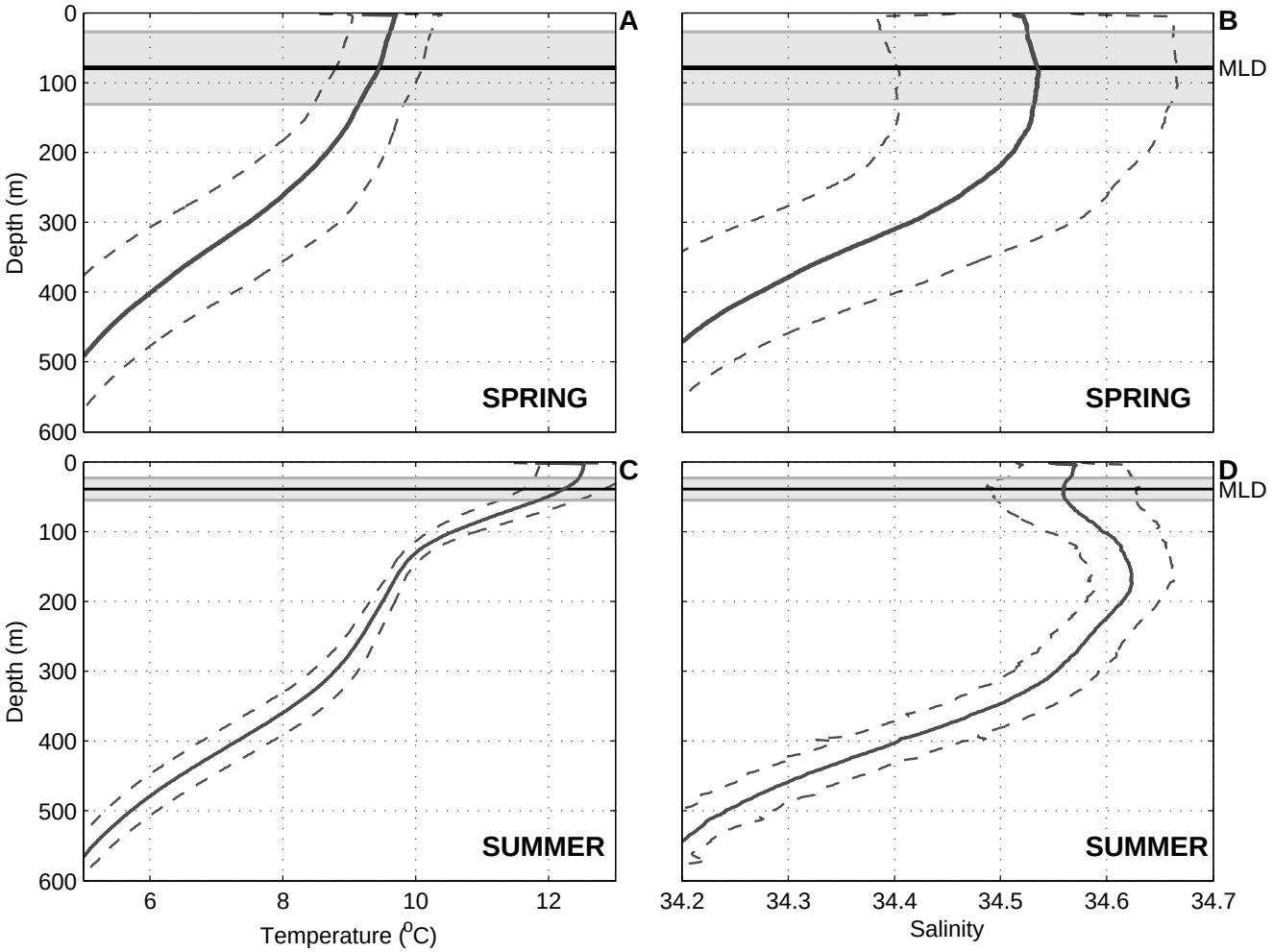

Figure 4.6: Mean vertical profiles for the top 250 m of A) temperature ($^{\circ}C$) and, B) salinity during spring, are compared to C) temperature ($^{\circ}C$) and, D) salinity during summer. Dashed grey lines indicate standard deviation of the profiles. Solid black horizontal lines indicate depth of the mean MLD (m) for the respective periods as determined using the $\Delta T_{10m} = 0.2\ ^{\circ}C$ criteria from de Boyer Montégut et al., 2004. Grey shaded areas indicate standard deviation of MLD.

ling off of the slope suggests a stronger variance in the near-surface lateral density structure at the mesoscale. With increasing horizontal resolution the slope levels off further, signalling a strong level of variance with finer spatial scales. A clear spike in the spectra is observed at $\sim$12 km that stands out at around an order of magnitude above the rest of the signal. The physical process occurring near the surface at the spatial scale of $\sim$12 km that generates this spike is unclear, however, it seems to separate the sub-mesoscale below from the larger spatial scales. The variability within the sub-mesoscale shown by the density slope suggests a notable amount of spiking with ranges occurring just within the error bar. This could likely be a

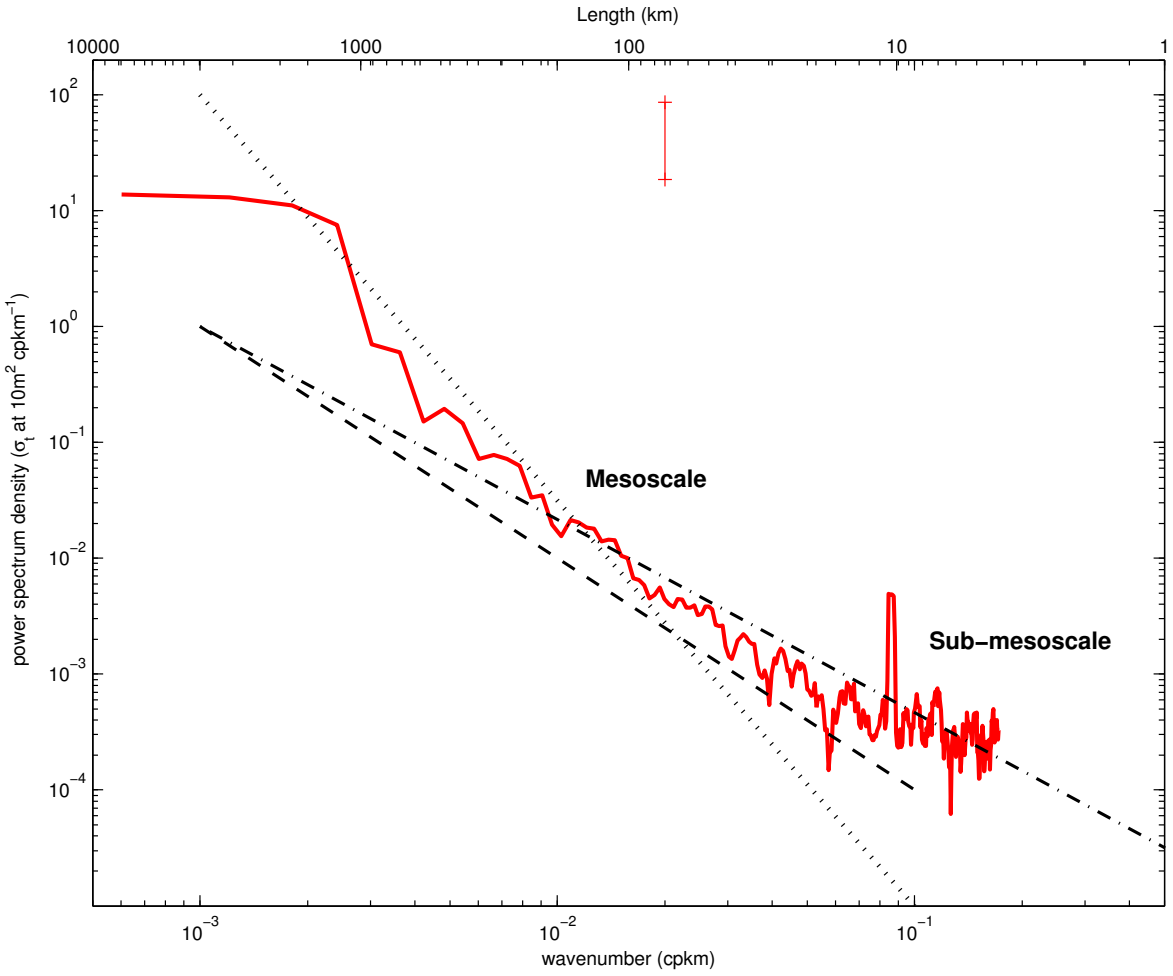

Figure 4.7: Multi-taper power spectrum density analysis of the SG573 density at 10 m (red line) using 7 tapers with the error bar indicated. The -5/3 (dot-dashed), -2 (dashed) and -3 (dotted) spectrum slopes are represented.

result of the inconsistent lateral dive distances between profiles as the glider samples with a dive distance range from 200 m to over 7 km.

4.2.2 Meso- to sub-mesoscale heterogeneity

Mesoscale

To provide spatial context to the position of glider sampling relative to the STF and SAF of the Southern Ocean, the latitudinal frontal locations with respect to each day of SOSCEx

is shown in Figure 4.3. These indicate that the glider successfully sampled the area of the SAZ, merged between the colder PFZ to the south and the warmer STZ to the north. The individual features are discussed in relation to Figure 4.3 where the glider traverses through large spatio-temporal gradients in both MADT and SST. What is clear in Figure 4.3 is that the glider successfully samples across large lateral mesoscale gradients that change in both space and time.

Sub-mesoscale

Through obtaining a robust length scale of λ, this study will determine if observations of the sub-mesoscale are made and additionally compare to the spike of variability observed in the Multi-taper analysis. A map of λ is calculated from an Argo float dataset of 10 years for the Atlantic sector of the SAZ (Figure 4.8). For the region of this experiment, $\lambda \sim$15 km, which is in agreement with a map of λ made by Chelton et al. (1998) using global $1^\circ \times 1^\circ$ climatologies from temperature and salinity profiles. Estimates of λ determined from the glider are found to be similar to the sub-mesoscale of the literature (9.3 ± 0.5 km), around 5 km finer than the Argo dataset and the global climatology, possibly due to the increase in resolution.

Nevertheless, the mean distance between the glider profiles (2.9 ± 1.5 km) falls well within the sub-mesoscale range, which quantitatively indicates that the glider used in this study is able to sample and resolve variability in the sub-mesoscale range.

4.2.3 Lateral gradients in near-surface density

Lateral gradients in the near-surface (10 m) density structure is very useful in determining sub-mesoscale surface ML fronts. Sharp gradients are indicative of sub-mesoscale features that hold the potential to relax (lighter water riding over heavier water) and generate an overturning flux which restratifies the ML. This is shown in the evolution of the 10 m density (Figure 4.9).

A gradual decrease in density is observed, which is related to the seasonal warming of the upper ocean. However, within the seasonal decline in density (-4.9 $\times$ 10^{-7} $kg\ m^{-4}$) are interspersed periods of sharp spikes with length scales of <10 km. These sharp increases and

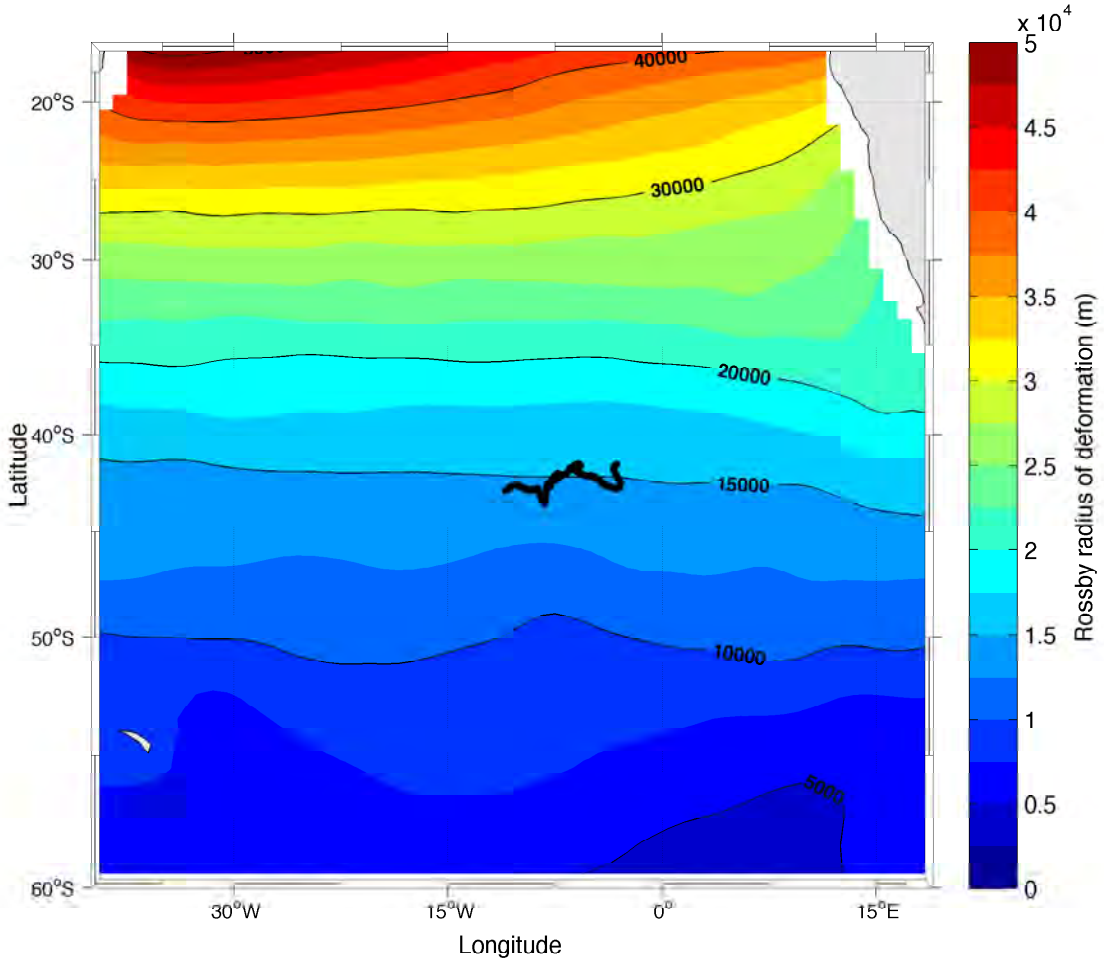

Figure 4.8: Length scale of the first baroclinic Rossby radius of deformation (λ) for the Atlantic Southern Ocean generated from Argo float profiles of 1°× 1° resolution. SG573 trajectory is indicated as black line.

decreases illustrate lateral density gradients near the surface of the ocean, which seem to be prominent throughout the spring and summer periods.

4.2.4 Seasonal lateral buoyancy field

The absolute buoyancy term (b) is calculated for each of the profiles with the lateral gradient (b_{xy}) applied to the 10 m density. Larger gradients are understood to hold greater potential for overturning where relaxing of the gradient would cause rearrangement of the buoyancy term in the xy-z plane. The interest lies in the relative seasonal abundance of b_{xy} as z-plane readjustments are key in restratifying the ML. For example, in spring it is of interest

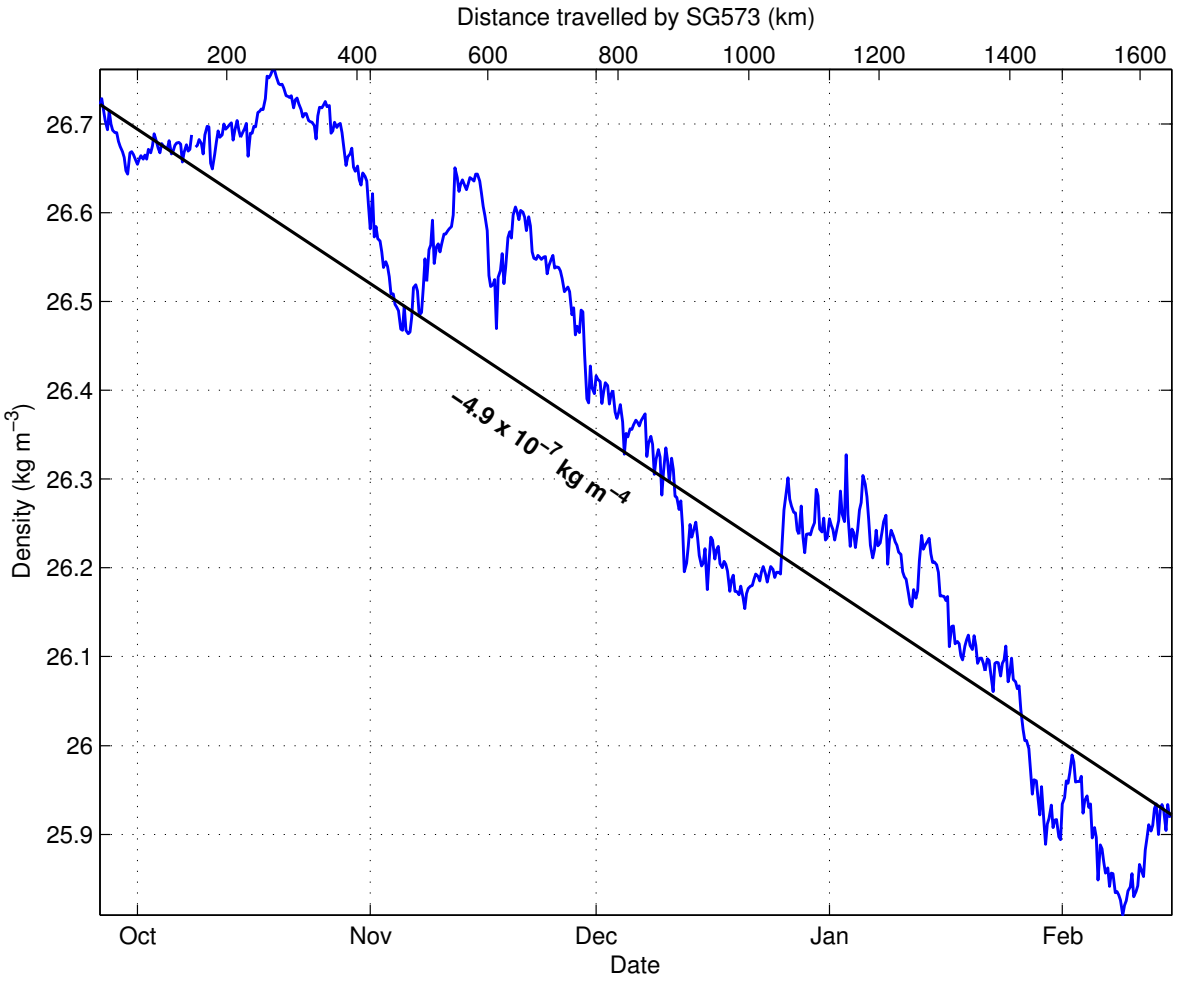

Figure 4.9: Density at 10 m acquired from SG573 for the period of SOSCEx (blue line). Black line indicates the mean lateral density gradient for the duration of SOSCEx, reported at -4.9 $\times$ 10^{-7} kg m^{-4}.

to determine whether relaxation of the larger b_{xy} are generating the substantial rates of ML restratification and whether these mechanisms are prominent in the summer as well.

The seasonal comparison is performed in the form of normalized histograms (Figure 4.10). Both spring (A) and summer (B) display evidence of large b_{xy} that have comparatively similar values $>1 \times 10^{-7}$ s^{-2}. These values are important as observations of ML eddy restratification were found with values $<1 \times 10^{-7}$ s^{-2} by Mahadevan et al. (2012b). A substantial majority of the b_{xy} for both seasons (89% for spring, 82% for summer) fall below 1×10^{-7} s^{-2}, with a more even spread in the summer. Despite this, both seasons show comparative magnitudes and distributions, suggesting the potential for similar buoyancy adjustments between seasons.

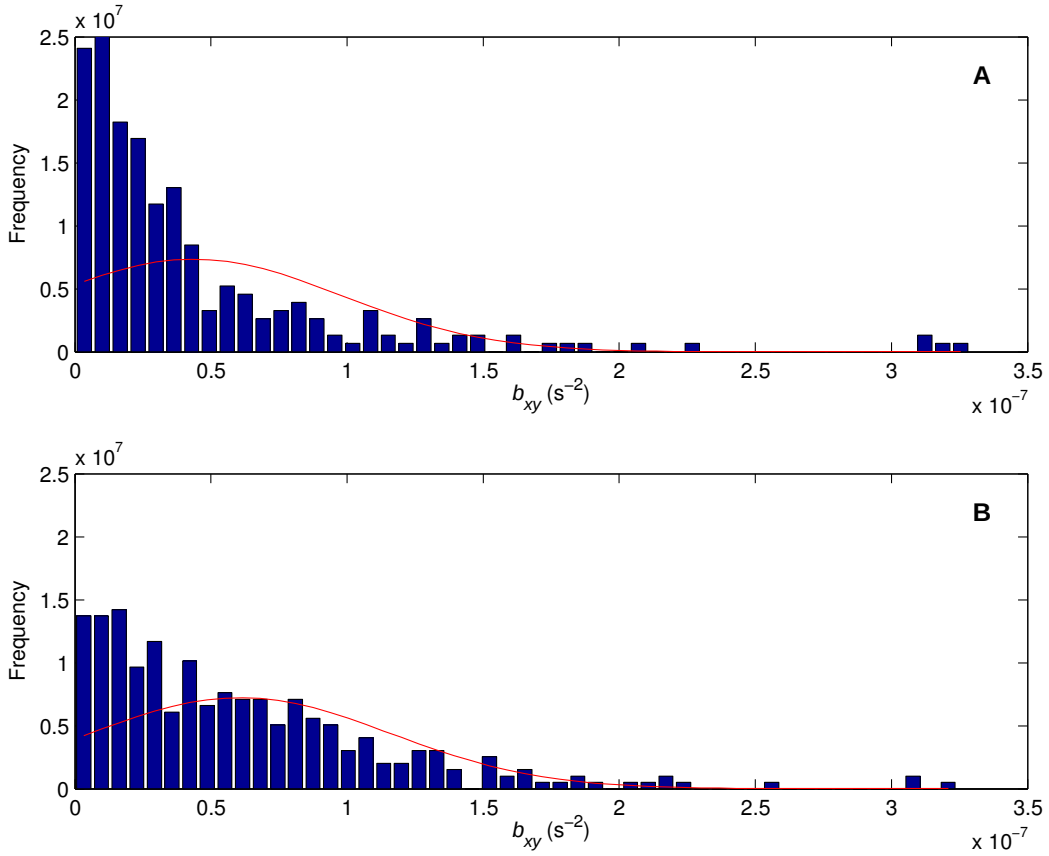

Figure 4.10: Normalized histograms indicating the distribution of b_{xy} for A) spring and B) summer during SOSCEx. Probability density function showing the overall distribution is overlaid in red.

4.3 Springtime restratification in the SAZ and its link to ML eddies

The spring ML is characterised by highly variable MLDs, ranging from 12 m to 272 m with intermittent periods of rapid shoaling and deepening throughout the season. In order to focus on what is driving the strong events of rapid variability of the springtime MLD, a timeline approach is performed. Notable occurrences whereby the MLD responds to both upper ocean buoyancy and atmospheric forcing are analysed independently in this study.

Spatio-temporal changes in the hydrographic sections are synonymous with these rapid

changes in the MLD (Figure 4.11). For example, on 6 October and 16 November the MLD shoaled by 157 m and 90 m in just a day respectively, while on 18 October, the MLD deepened 137 m in a period of one day.

The events of rapid restratification of the MLD occur when an increase of N^2 at around 20 m shoals the MLD above the deeper core of stratification. This increase in N^2 is referred to as a 'tail of restratification'. The stratification core is related to the seasonal pycnocline and its upper bound varies from around 150 m for the first half of October and November onwards to below 300 m towards the latter half of October. In the case of a well mixed upper ocean, the N^2 is almost fully erased above the seasonal pycnocline, where the MLDs reach their maximum depth. Therefore, surface ocean processes that are generating a fresh layer of stratification above the seasonal pycnocline are causing a rapidly restratifying MLD. These events are found mostly < 100 m. Therefore, a mean N^2 of the upper 100 m and the mean of 100-300 m separates variations from events of restratification (N^2_{0-100m}) and the seasonal pycnocline ($N^2_{100-300m}$) (Figure 4.12A). In order to explain the variations of these parameters, time series of springtime MLD (Figure 4.12B), wind stress (C), lateral buoyancy gradient (D), MADT (Figure 4.13A), temperature (B), salinity (C) and density (D) of the upper 100 m, which indicate the ML water mass properties, are shown. Next, a series of 4 dynamical regimes that assist in characterising the spring ML and stratification behaviour are analysed.

4.3.1 Mesoscale eddy

Upon deployment, the glider navigated eastward through the centre of a cold-core cyclonic eddy (∼8 °C, ∼34.3 at surface core) (Figure 4.14A and B). The eddy is identified by using satellite altimetry and SST (Figure 4.14A and B respectively) and is marked by the grey shaded area between deployment and 7 October in Figures 4.12 and 4.13. It is characterised cyclonic rotation of the surface current as well as a decrease in sea level of 0.15 *dynamic* m and SST by 0.7 $°C$ from the edge to the core (Figure 4.14A and B). This occurs due to the equilibrium established between the Coriolis force and pressure gradient. As a result, cold, fresh and lighter water (∼1 °C, ∼0.3, 0.08 kgm^{-3}) is upwelled at the core from >200 m and completely mixed within the eddy as a likely result of the strong horizontal stirring, which

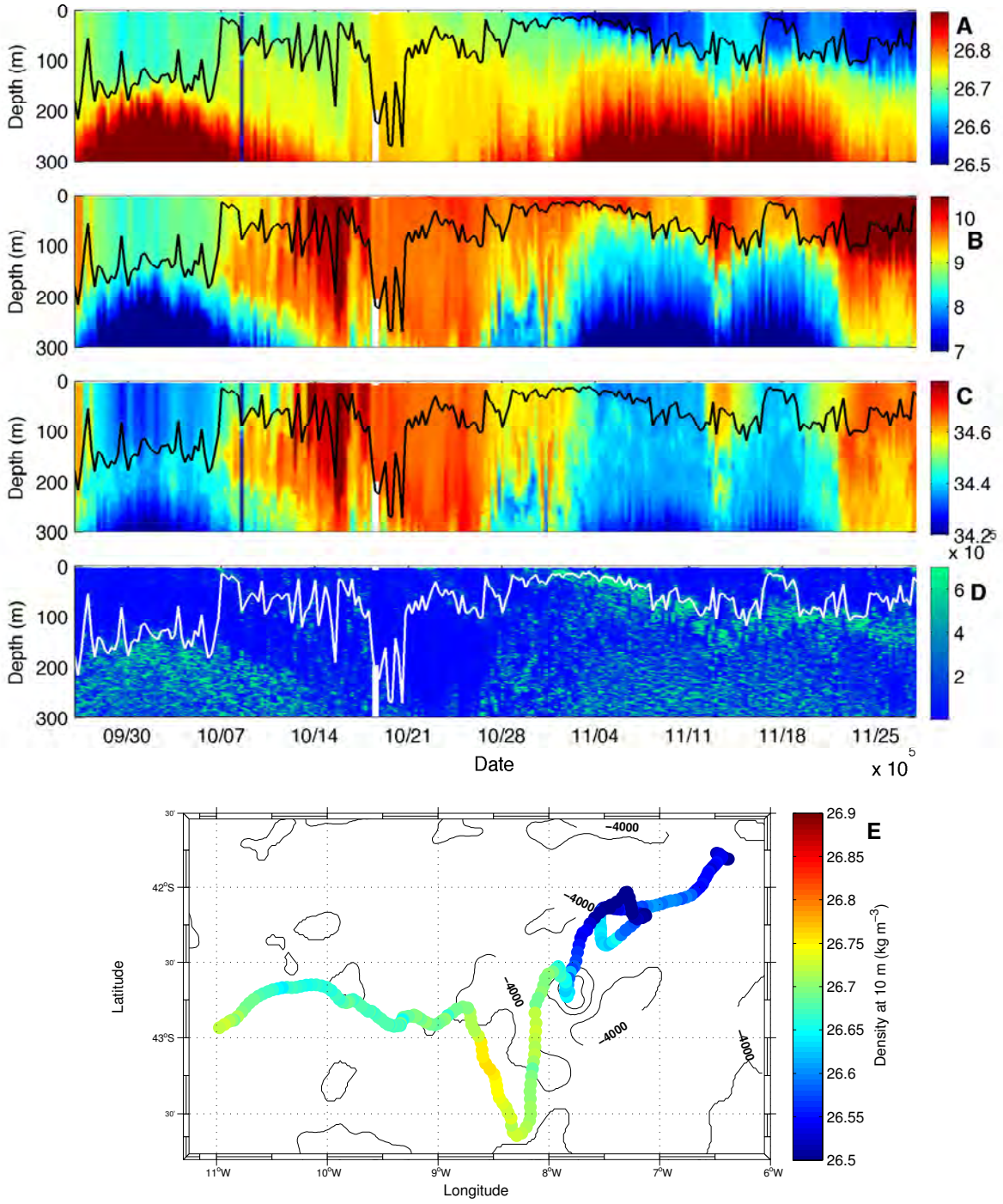

Figure 4.11: Sections of A) density ($kg\ m^{-3}$), B) temperature ($°C$), C) salinity and D) Brunt-Väisälä frequency (N^2) for the upper 300 m of SG573 for the spring period of SOSCEx (26 September - 28 November). The MLD is overlaid in black for A, B, C and in white for D. E) SG573 springtime trajectory with colour indicating the 10 m density field.

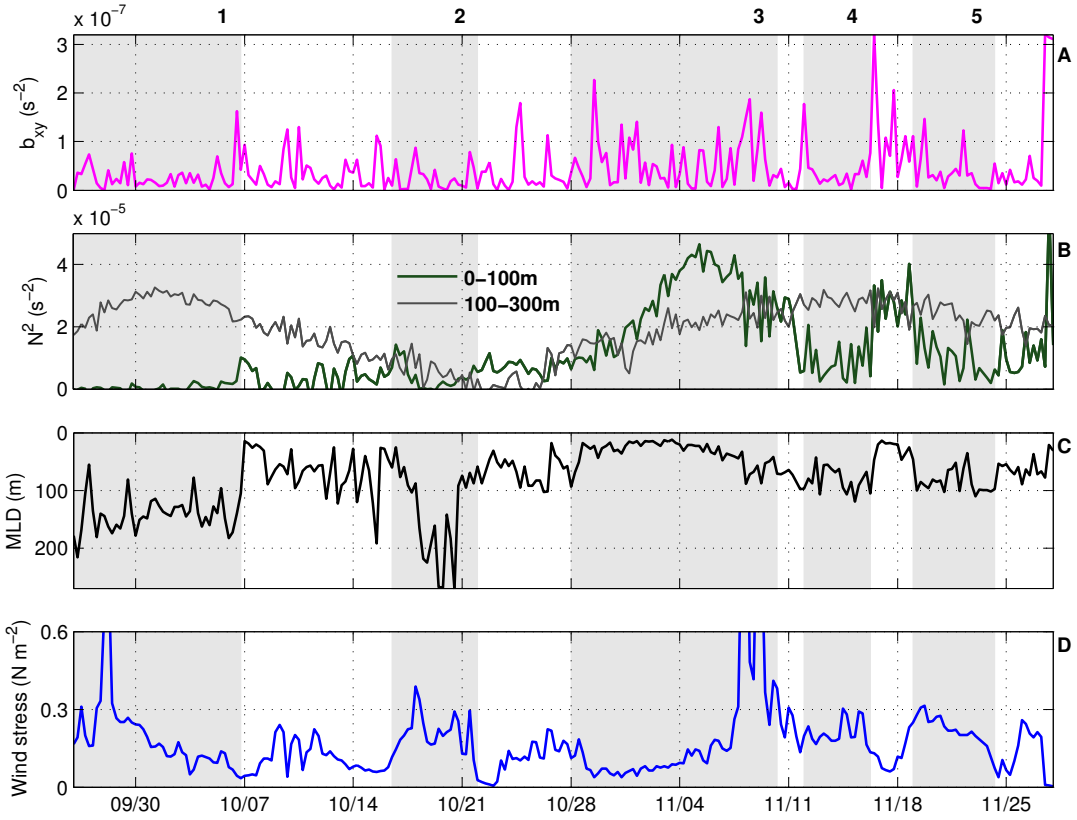

Figure 4.12: Spring time series of SG573 for A) the lateral buoyancy gradients between profiles (in s^{-2}). B) Brunt-Väisälä frequency (N^2 in s^{-2}) averaged for the upper 100 m (dark green line) and 100-300 m (light grey line), C) the MLD (in m) and D) wind stress ($N\ m^{-2}$).

eradicates the any near surface stratification.

This means that the MLD follows the seasonal pycnocline, which resembles a bell shape as a result of upwelling in the core creating a rise of stratification closer to the surface. This resulted in the $N^2_{100-300m}$ increasing from $\sim 2 \times 10^{-5}\ s^{-2}$ to $\sim 3 \times 10^{-5} s^{-2}$ from the edge to the core (Figure 4.12A), with the MLDs shallower at the core ($\sim 130m$) than at the edge ($\sim 180m$). The deeper MLDs at the edge of the eddy are likely caused by a downwelling process that generates deeper mixing and therefore pushing the stratification down.

As the glider traverses out of the eddy (7 October on Figure 4.14A and B), the N^2_{0-100m} spikes to $\sim 1 \times 10^{-5}\ s^{-2}$, resulting in the rapid shoaling of the MLD from 183 m to 15 m in 24 hours over a lateral displacement of 9 km. This falls within the sub-mesoscale range.

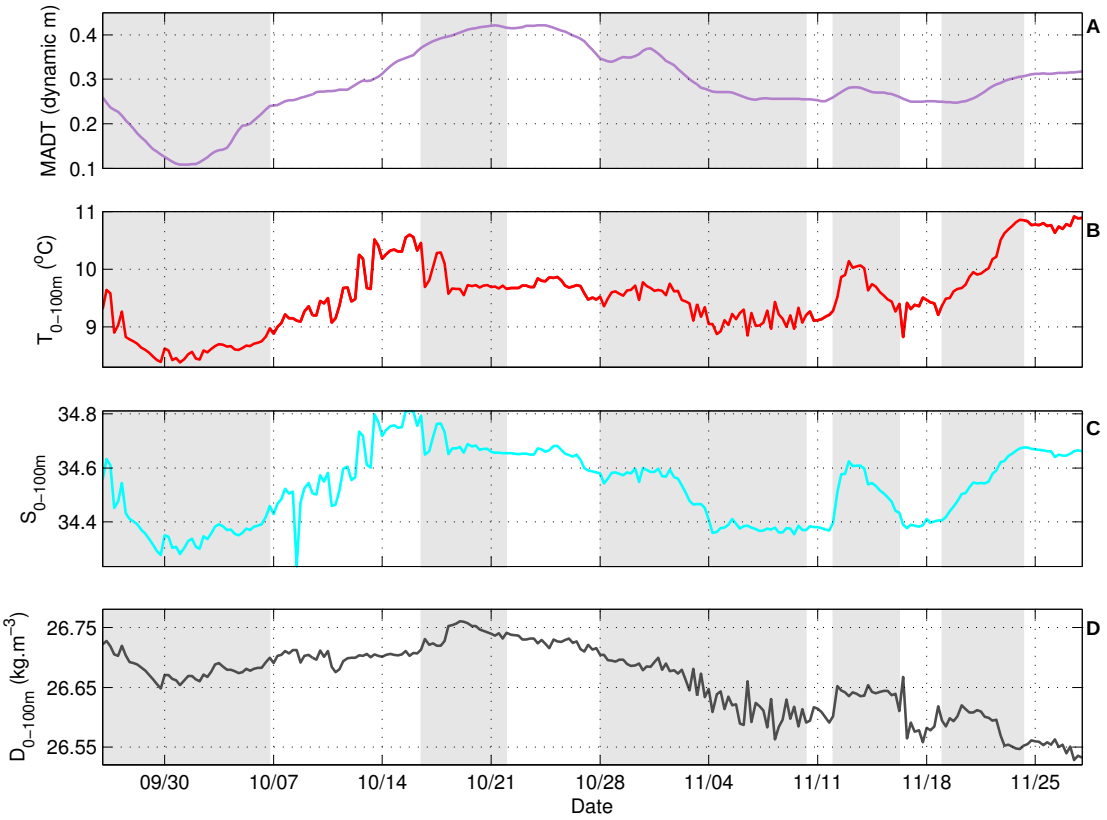

Figure 4.13: Spring time series from SG573 for A) satellite altimetry in *dynamic* m as well as the mean values for the upper 100 m of B) temperature (°C), C) salinity and D) density $kg\ m^{-3}$.

The likely advection of lighter surface water from the eddy over surrounding the water mass meant that as the glider leaves the eddy, it encounters strong vertical stratification, which is observed as a slumping of the vertical density profiles (Figure 4.14C). It is seen as a tail of increased N^2 which is strongest and most shallow closest to the eddy (Figure 4.11D), before extending down to ∼80 m further away from the eddy.

An explanation for the restratification at the ML front could be that the stratifying surface buoyancy flux $\langle w\prime\, b\prime \rangle_e$ needs to overcome destratifying effects by surface cooling $\langle w\prime\, b\prime \rangle_{cool}$ and a down-frontal wind stress $\langle w\prime\, b\prime \rangle_w$. The instantaneous changes in wind direction relative to the frontal axis means that it is too difficult to determine whether the wind direction is up- or down-front. Therefore, for this study the wind direction is assumed down-frontal based on the meridional gradients in large scale fronts (Figure 4.3) and the persistently westerly winds (Figure 4.15). This is also undertaken in order to ensure that potential mixing from

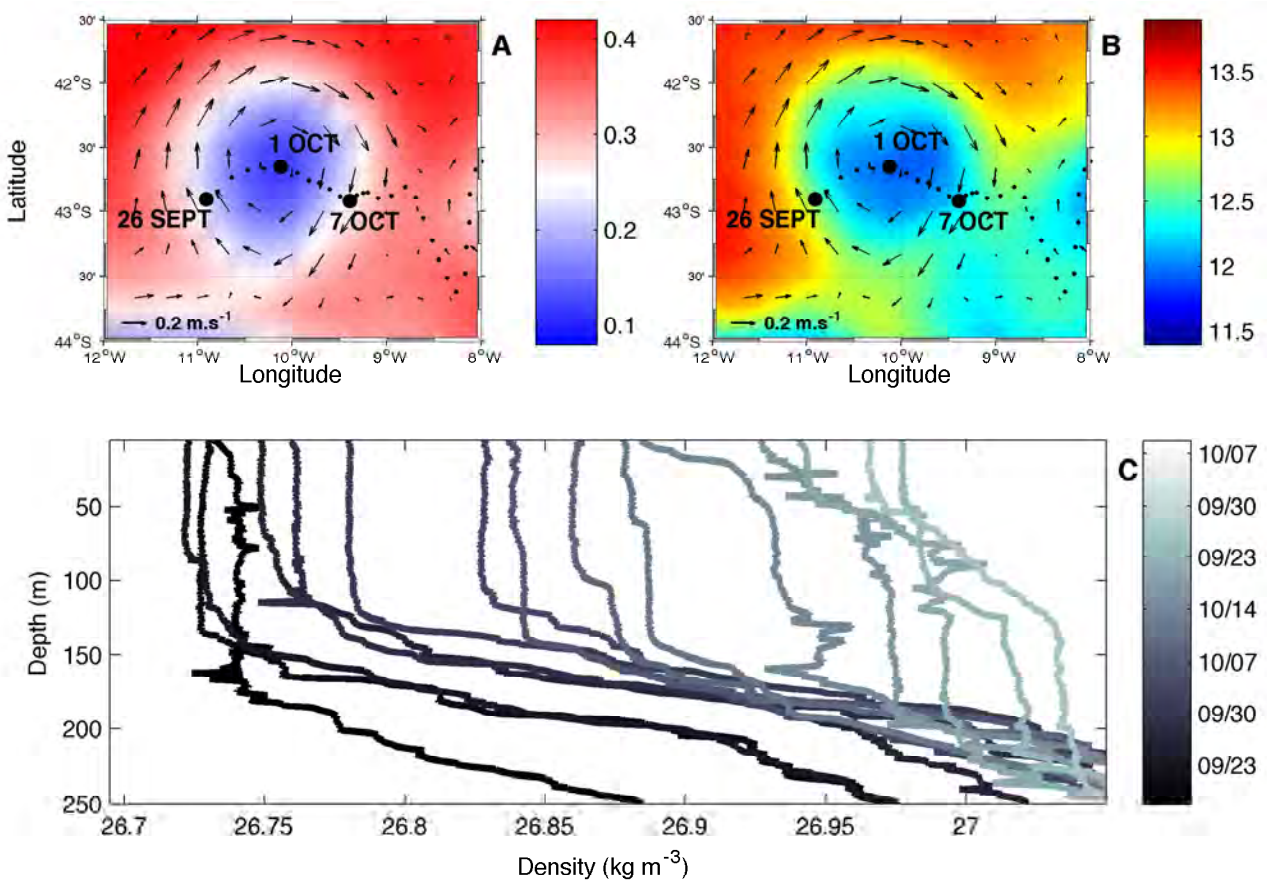

Figure 4.14: A) Satellite altimetry (*dynamic m*) and B) SST (°C) averaged for the period 26 September to 7 October indicate the presence of a cyclonic mesoscale eddy with strong cyclonic surface velocities shown by direction and strength of arrows. Black dots indicate daily SG573 profile locations. C) The daily time evolution of isopycnals for the same period have been separated by 0.03 $kg\ m^{-3}$ for clarity and represent SG573 traversing through the eddy and across its edge.

down-frontal winds is not ignored and ML eddy restratification is not biased.

The surface buoyancy flux equations are computed using $f = 1.33 \times 10^{-4}\ s^{-1}$, $b_{xy} = 0.72 \pm 0.75 \times 10^{-7}\ s^{-2}$, $\tau = 0.05 \pm 0.02\ N\ m^{-2}$, $MLD = 123 \pm 68\ m$ and $Q = 46 \pm 290\ W\ m^{-2}$ and $g = 9.81\ m\ s^{-2}$. These parameters represent the mean and standard deviation values as the glider crossed the ML front and the ML restratified, totalling 12 km over the period of one day.

The resultant $\langle w\prime\, b\prime \rangle_e$ equated to be larger than the combination of $\langle w\prime\, b\prime \rangle_{cool} + \langle w\prime\, b\prime \rangle_w$, thereby supporting the notion of restratification by the overturning buoyancy flux induced by ML eddies.

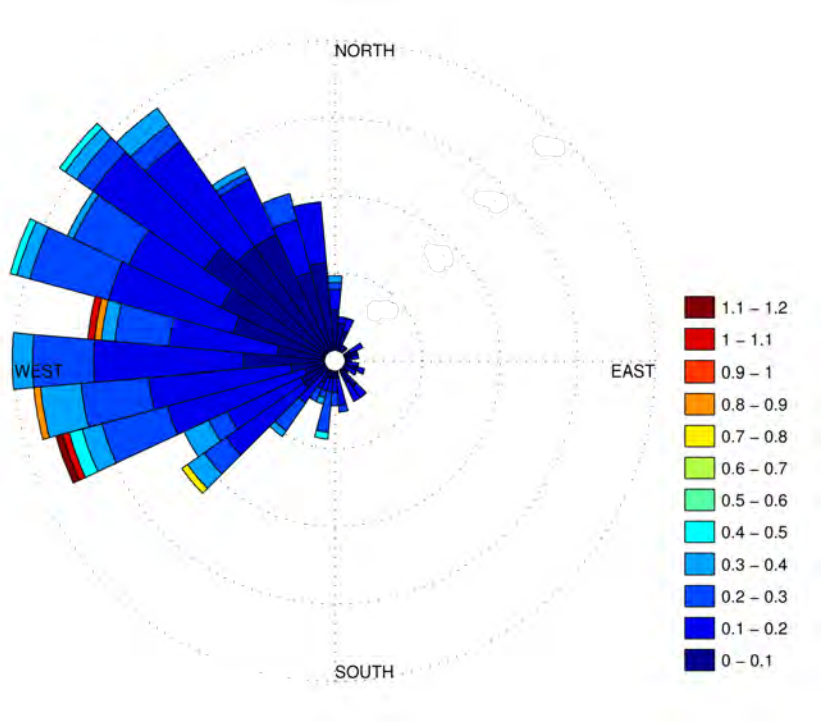

Figure 4.15: Wind rose indicating the wind direction and stress at the location of SG573 for the duration of SOSCEx. The legend values indicate wind stress ($N\ m^{-2}$).

4.3.2 Eddy-induced overturning at a mesoscale front

The sampling across a mesoscale meander that is assumed to be in geostrophic balance occurs between 7 to 16 October (Figure 4.16 A).

This resulted in a net increase of T_{0-100m} and S_{0-100m} by ∼1.5 °C and 0.4 respectively (Figure 4.13B and C). Intermittent periods of variability (*e.g.* ∼1 °C and 0.2 in a day) were likely related to lateral gradients in small scale features (Figure 4.12D) with enhanced N^2_{0-100m} generating a thin layer of stratified water above the seasonal pycnocline. The MLD followed this restratification, occurring mostly above 100 m with large shoaling and deepening (15-190 m) of similar variability to that of the lateral surface buoyancy gradient (Figure 4.12B and D). It is speculated that sub-mesoscale meanders and fronts drive the observed variability in lateral buoyancy gradients, which are noticeably large on 9, 10 and 15 October (b_{xy} >1.1 × $10^{-7}\ s^{-2}$). By averaging the surface buoyancy flux parameters across the front, the evolution of the lateral buoyancy field budget across the front is established. The averaged parameters

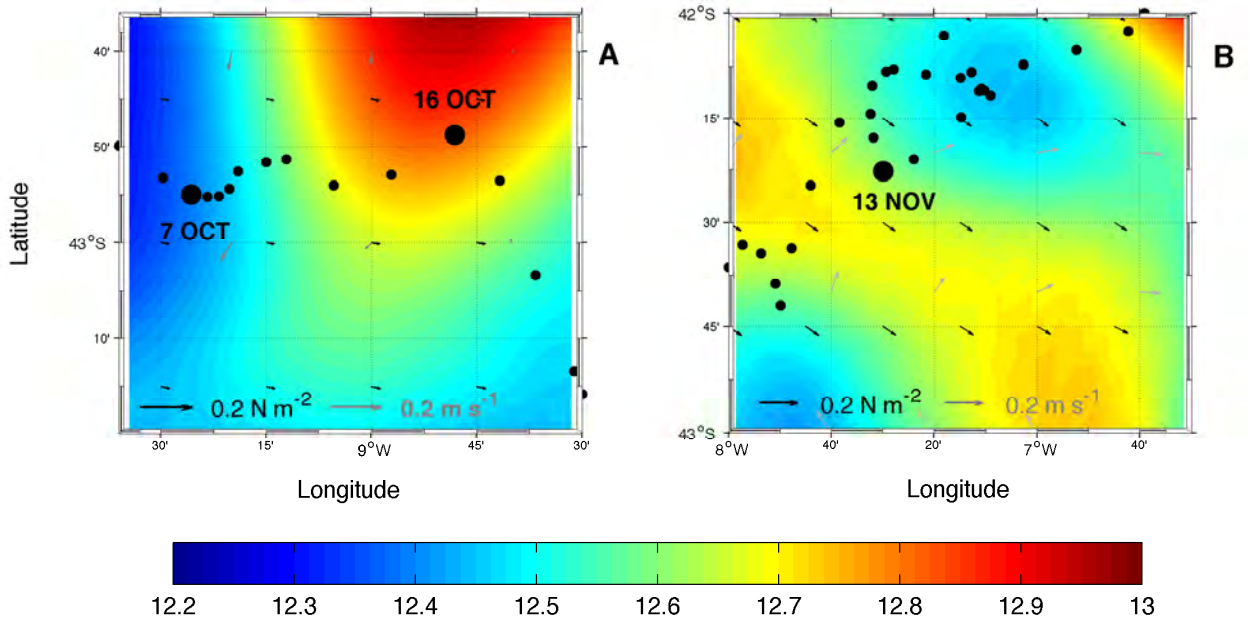

Figure 4.16: Mean SST (°C) for the period of A) 7 and 16 October and B) 13 November. Black dots indicate SG573 profile locations while black arrows show mean wind speed and direction during the respective dates. Grey arrows show direction and strength of surface velocities.

$b_{xy} = 0.36\times\ 10^{-7}\ s^{-2}$, $\tau = 0.11\ N\ m^{-2}$, $MLD = 65\ m$ and $Q = 180\ W\ m^{-2}$ indicate that $\langle w\prime\, b\prime\rangle_e > \langle w\prime\, b\prime\rangle_{cool} + \langle w\prime\, b\prime\rangle_w$. This supports the hypothesis that a positive surface buoyancy field is restratifying the ML above the seasonal pycnocline.

4.3.3 Evidence of wind-induced MLD deepening

The glider changed to a poleward direction on 17 October (marked by second grey area of shading in Figures 4.12 and 4.13) while the wind stress increased to >0.3 $N\ m^{-2}$. The rise in wind stress is likely responsible for an erosion of N^2_{0-100m} from $>1\ \times\ 10^{-5}$ to $\sim 0\ \times\ 10^{-5}$ s^{-2}, deepening the MLD to the seasonal pycnocline and subsequently reaching the maximum measured depth of 272 m. Three days later, the wind stress sharply decreased from ~0.3 to ~0 $N\ m^{-2}$ in 12 hours when a subsequent small increase of N^2 developed around 80 m with the N^2_{0-100m} increasing to $>1\ \times\ 10^{-5}\ s^{-2}$. The MLD shoaled to meet the elevated N^2 above 100 m and continued to follow the depth of restratification above the seasonal pycnocline, despite the wind stress increasing to above 0.2 $N\ m^{-2}$ again.

Following a drop in the wind stress (<0.1 $N\ m^{-2}$) on 28 October, (third grey shaded area in (Figures 4.12 and 4.13) a sustained low wind stress for around a week with an average of 0.08 $N\ m^{-2}$ occurred synonymously with the formation of a cap (∼20 m) of low density water (∼26.5 $kg\ m^{-3}$) with a gradually increasing depth in time. A resulting increase in N^2_{0-100m} from ∼1 to ∼4 × $10^{-5}\ s^{-2}$ generates an intense increase in N^2 ∼20 m, shoaling the MLD for the week. It is likely that the combination of low wind stress and an increasing Q_{net} (Figure 4.1B) over this period considerably enhanced the stratification. Additionally, the springtime maximum in N^2 of 80 × $10^{-5}\ s^{-2}$ that forms the MLD pycnocline is reached. This intense stratification is considered a transitional phase in the ML, whereby from this point onwards the MLD does not deepen past 120 m again.

This statement is emphasised between 5 to 7 November, when the wind stress steadily increases from ∼0.1 to ∼0.3 $N\ m^{-2}$, decreasing N^2_{0-100m} from ∼4.6 × 10^{-5} to ∼3.8 × 10^{-5} s^{-2}. On 8 November, the wind stress strengthens to >1 $N\ m^{-2}$ for 2 days, the strongest of the entire dataset leading to a subsequent decrease in N^2_{0-100m} of ∼1.5 × $10^{-5}\ s^{-2}$. The tail of stratification marking the MLD remains relatively high with values exceeding >20 × $10^{-5}\ s^{-2}$. However, the maximum extent of the stratification deepens from ∼20 m to ∼90 m, synonymous with the MLD. This is likely due to the turbulent mixing generated from the strong surface wind forcing.

The Q_{net} remains positive during this period, except for 10 November (-25 $W\ m^{-2}$), suggesting that although wind stress induced turbulence erodes vertical stratification, a heating contribution to the surface ocean aids the existing stratification. Despite the strongest wind stress of the survey period, the MLD did not extend beyond 100 m, which is in contrast to the deep MLDs observed around 17 October when wind stress values were around 0.3 $N\ m^{-2}$. The key difference in mixing depth between the two scenarios is the pre-existing stratification state prior to the respective wind events.

During the initial event, N^2_{0-100m} was just over 1 × $10^{-5}\ s^{-2}$ with $N^2_{100-300m}$ of similar value, which meant that vertical stratification was quickly eroded allowing for deep turbulent

mixing and deep MLDs, whereas prior to the subsequent event, the pre-existing enhanced stratification near ∼20 m increased the N^2_{0-100m} to >4 × 10^{-5} s^{-2}, with a deeper maximum of stratification below 100 m where $N^2_{100-300m}$ >2 × 10^{-5} s^{-2}. The high N^2_{0-100m} was not eroded sufficiently during the wind event, allowing the MLD to remain shallower than 100 m.

On 12 November, the glider samples a warmer (∼1 °C) and saltier (∼0.2) water mass, likely to be of Subtropical origin (Figure 4.13B and C). ML properties identified by T_{0-100m} and S_{0-100m} suggest that it is Subtropical Surface Water (STSW) that is being sampled (T_{100m} >10 °C, S_{100m} >34.6, Orsi et al., 1995). Glider location and the respective SST product on 13 November (when the most prominent characteristics of the water mass is sampled) indicates that only the edge of the STSW mass is sampled.

Notable from a T-S diagram (Figure 4.17) is the contrast of the ambient water mass properties to the STSW properties. A large departure in salinity from <34.4 to ∼34.6 occurs within the ML, with traces of STSW below the ML at ∼200 m. This is additionally evident in the temperature, with warming from ∼9.3 °C to >10 °C within the ML. The core of the STSW extends down to ∼150 m, suppressing the seasonal pycnocline and as a result decreasing N^2_{0-100m} from >3 × 10^{-5} s^{-2} to <2 × 10^{-5} s^{-2} and increasing the $N^2_{100-300m}$ from ∼2.5 × 10^{-5} s^{-2} to >3 × 10^{-5} s^{-2}.

The increase in D_{0-100m} of the STSW indicates that the increase in salinity dictates the buoyancy term, with a more salty core extending to ∼100 m. This generates stratification within the STSW with a shallower pycnocline above the seasonal pycnocline that defines the MLD.

On 16 November, the T_{0-100m} and S_{0-100m} indicates that the glider departed the STSW and sampled more characteristically Subantarctic water. A synonymous decrease in the wind stress from ∼0.3 to ∼0.1 N m^{-2} with the crossing of a substantial lateral buoyancy front (∼3 × 10^{-7} s^{-2}) resulted in restratification near the surface with an increase in N^2_{0-100m} by >2 ×10^{-5} s^{-2} and a shoaling the MLD from 100 m to 20 m in one day over a lateral distance of 4.6 km. The competition of surface buoyancy flux between overturning at the front and mixing from down-frontal winds and cooling show that $\langle w\prime\, b\prime \rangle_e > \langle w\prime\, b\prime \rangle_{cool} + \langle w\prime\, b\prime \rangle_w$ (τ = 0.13 N m^{-2}, Q = 201 W m^{-2}, f = 1.33 ×10^{-4} s^{-2} and MLD = 100 m). This suggests that

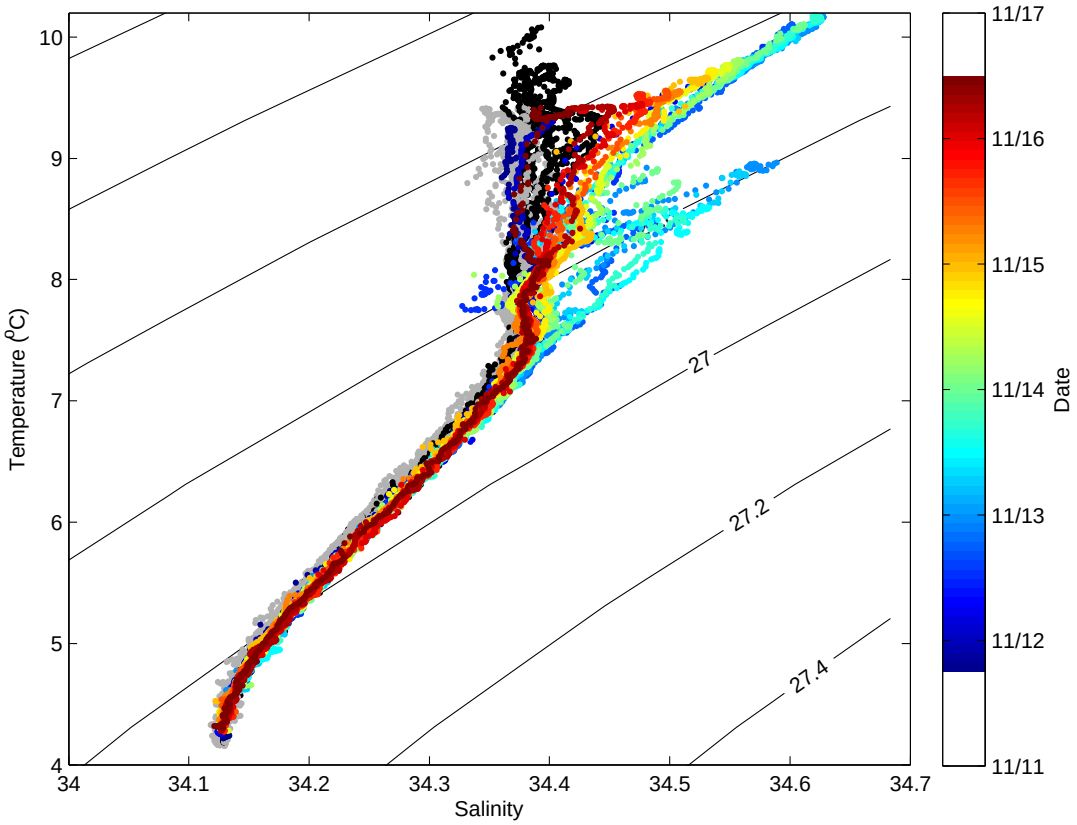

Figure 4.17: Temperature-salinity diagram for 12 - 16 November shown by colour profiles. Grey profiles represent two days before (10 and 11 November), while black profiles represent two days after (17 and 18 November) the sampling of the STSW feature (colour).

the presence of sub-mesoscale features and the heating from a strongly positive Q_{net} create an environment for rapid restratification to take place. The evolution of the vertical density profile from the vertical to the horizontal illustrates the isopycnal tiling as the positive buoyancy field restratifies the ML.

For the 5th grey shaded area in Figures 4.12 and 4.13 on 19 November, erosion of the stratification by ML eddies means that the MLD is once again determined by the deeper pycnocline at $\sim$100 m (Figure 4.11D). This is likely due to an increase in the wind stress from $\sim$0.05 to $\sim$0.3 $N\ m^{-2}$ over a single day. As a result, a large decrease in the Q_{net} is observed, with a mean value of -115 $W\ m^{-2}$ on 19 November, quickly increasing to 114 $W\ m^{-2}$ the following day. The N^2_{0-100m} decreases by $>2 \times 10^{-5}\ s^{-2}$ over the same period that the wind stress increases, along with the MLD from $\sim$20 to $\sim$100 m. By applying the mean

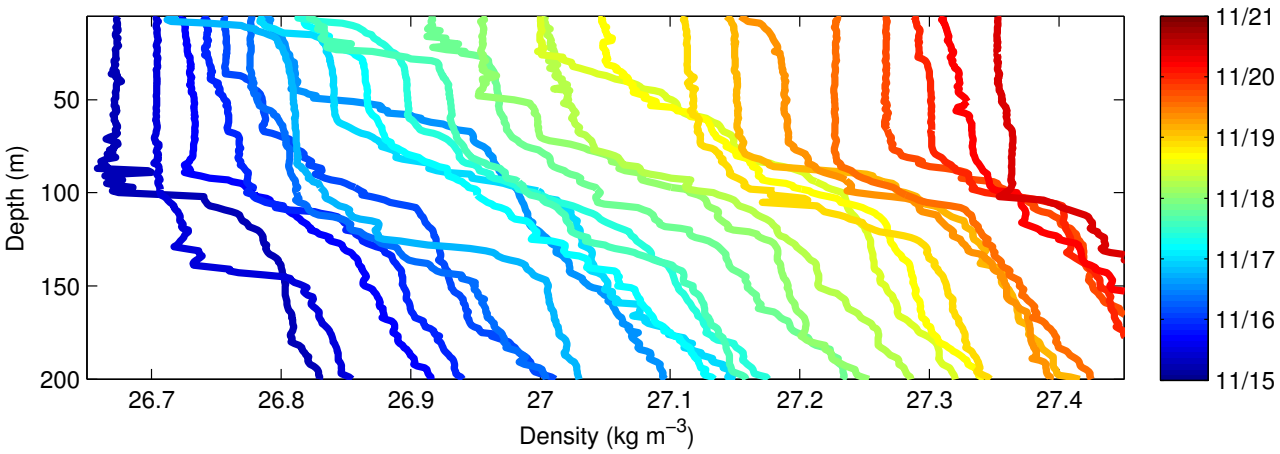

Figure 4.18: Evolution of the vertical density profiles ($kg\ m^{-3}$) from 15 to 21 November. The isopycnals have been separated by 0.03 $kg\ m^{-3}$ and represent the time evolution of the 6-hourly SG573 profiles.

parameters over the period of increasing wind stress (two days and 32 km covered by the glider) ($b_{xy} = 0.8 \pm 0.4 \times 10^{-7}\ s^{-2}$, $\tau = 0.18 \pm 0.09\ N\ m^{-2}$, $Q = 40 \pm 293\ W\ m^{-2}$, $f = 1.33 \times 10^{-4}\ s^{-2}$ and $MLD = 43 \pm 30\ m$) to the buoyancy flux equations, it is found that $\langle w\prime\, b\prime \rangle_e < \langle w\prime\, b\prime \rangle_{cool} + \langle w\prime\, b\prime \rangle_w$. This indicates that the restratification driven by ML eddies was destroyed in the space of one day. This is manifested as a $'$pushing up$'$ of the vertical density profiles with a complete homogenising of the top 100 m (Figure 4.18). Throughout this process, density characteristics between 100-200 m does not suggest interaction of varying water mass properties, as suggested by increases in T_{0-100m} and S_{0-100m}.

From this point in time (28 November), the physical characteristics of the summer ML are assumed to dominate therefore marking what is classified the end of the spring period.

4.4 Assessing the sub-seasonal coupling between wind and MLD

During summer, the amplitude of the MLD variability lacks proportionality to that of the springtime (12-272 m), with a range of 12-90 m. This is also represented in the mean restratification rates of the springtime MLD ($22 \pm 24\ m\ 6hr^{-1}$), which are more than double that during the summer ($10 \pm 7\ m\ 6hr^{-1}$), with a threefold difference in standard deviation.

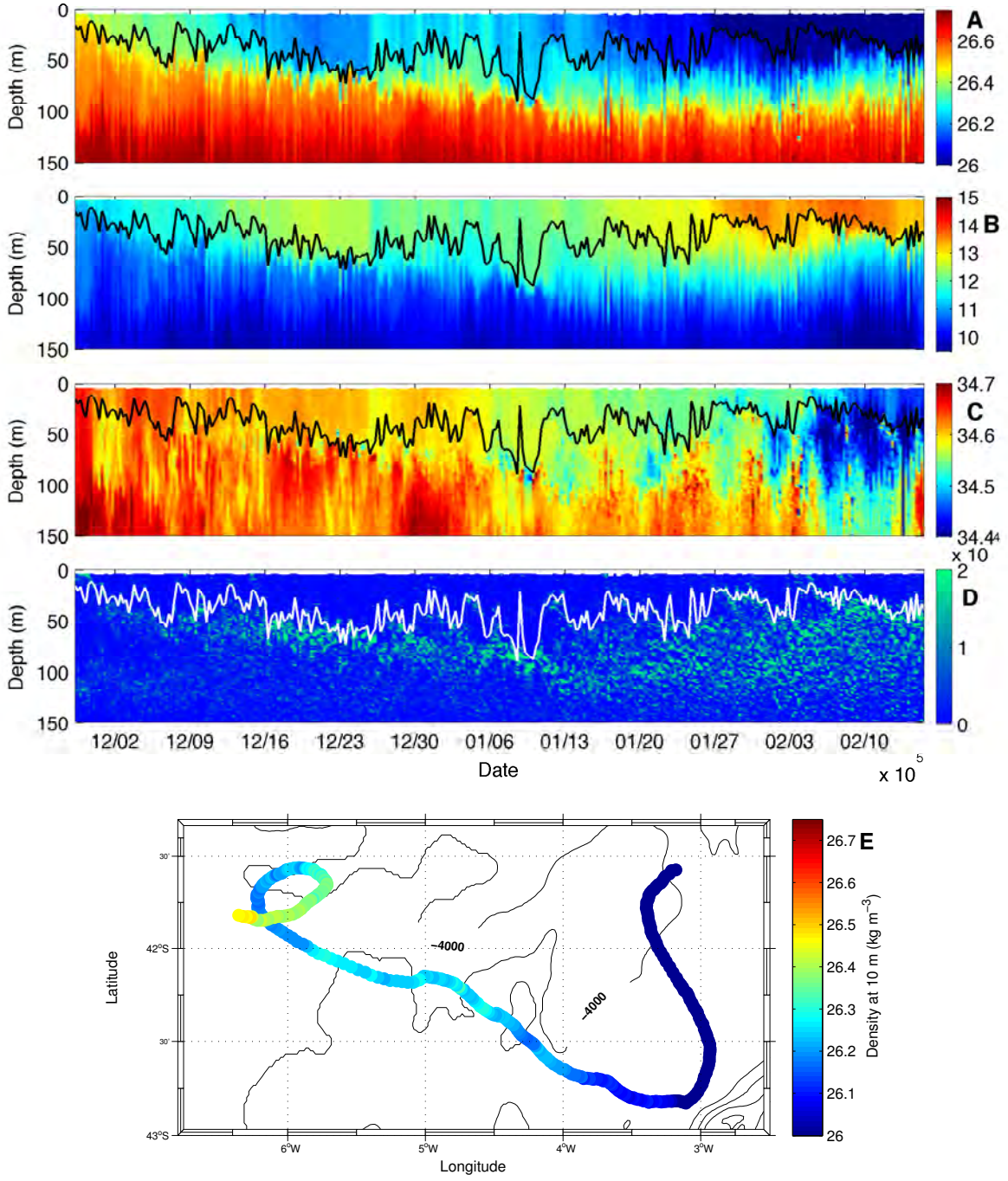

Figure 4.19: Sections of A) density ($kg\ m^{-3}$), B) temperature ($°C$), C) salinity and D) Brunt-Väisälä frequency (N^2) for the upper 150 m from SG573 during the summer period of SOSCEx (28 November 2012 - 15 February 2013). The MLD (m) is overlaid in black for A, B, C and in white for D. E) SG573 trajectory with colour indicating the 10 m density field.

The MLD is unable to penetrate deeper than 90 m in summer as a mean 2.8 $°C$ increase in the average top 100 m temperature between spring and summer (Figure 4.19C) increases the mean seasonal stratification in the upper 100 m from 1.1 $\times$ 10^{-5} to 6.4 $\times$ 10^{-5} s^{-1} (Figure 4.19D). The warming surface trend results in the entire ML temperature (T_{0-100m}) increasing from the summer minimum of 10.8 $°C$ in early December to the summer maximum of 13.6 °C in February (Figure 4.21B). The increase in ML temperature is synonymous with consistently (313 of 317 days) positive Q_{net} that has a mean of 178 $\pm$ 89 W m^{-2} over the summer period (Figure 4.20A).

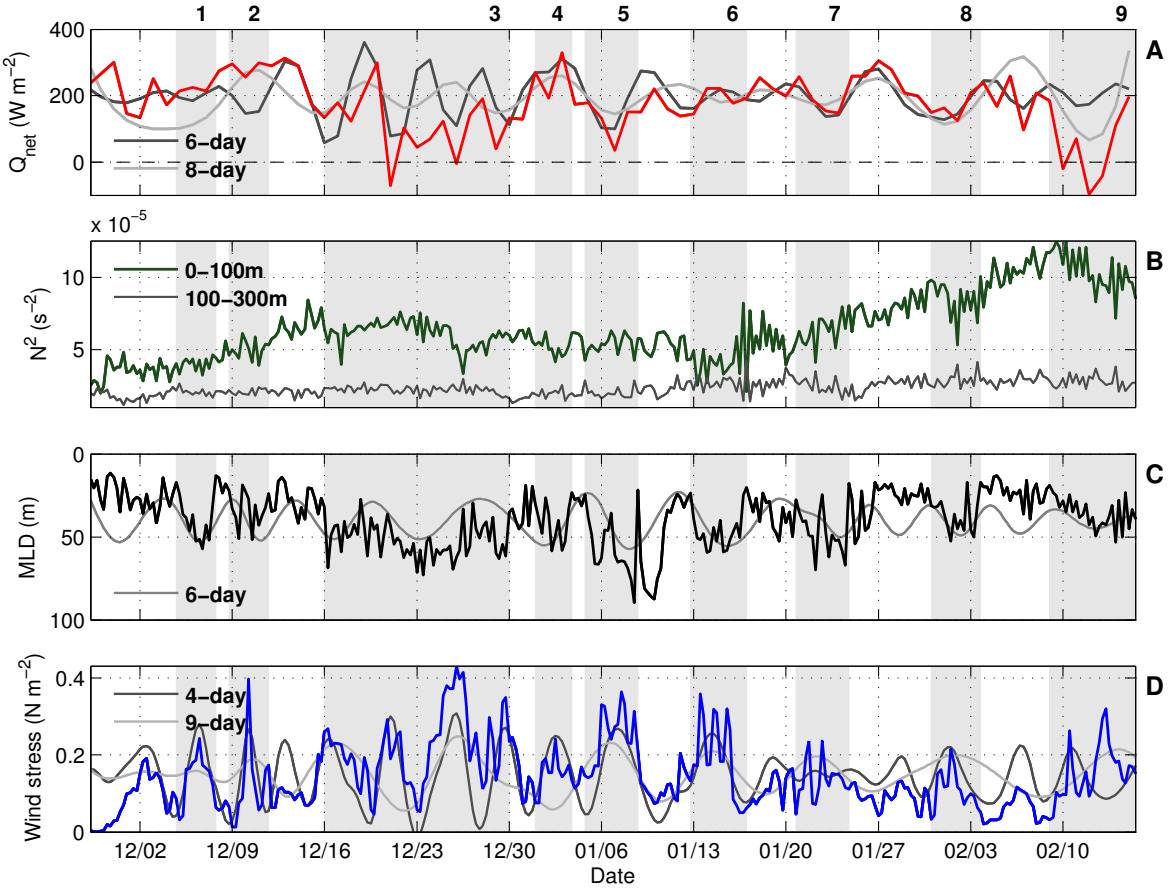

Figure 4.20: Summer time series for A) Q_{net} (red line, W m^{-2}) with 6-day and 8-day IMFs (dark and light grey respectively), B) N^2_{0-100m} in the dark green line and $N^2_{100-300m}$ in the dark grey line, both in s^{-2}, C) MLD (black line) and the 6-day IMF as light grey line and D) wind stress (blue line, N m^{-2}) with the 4-day IMF as the dark grey line and 9-day IMF as the light grey line. Event labels referred to in the text are displayed above panel A.

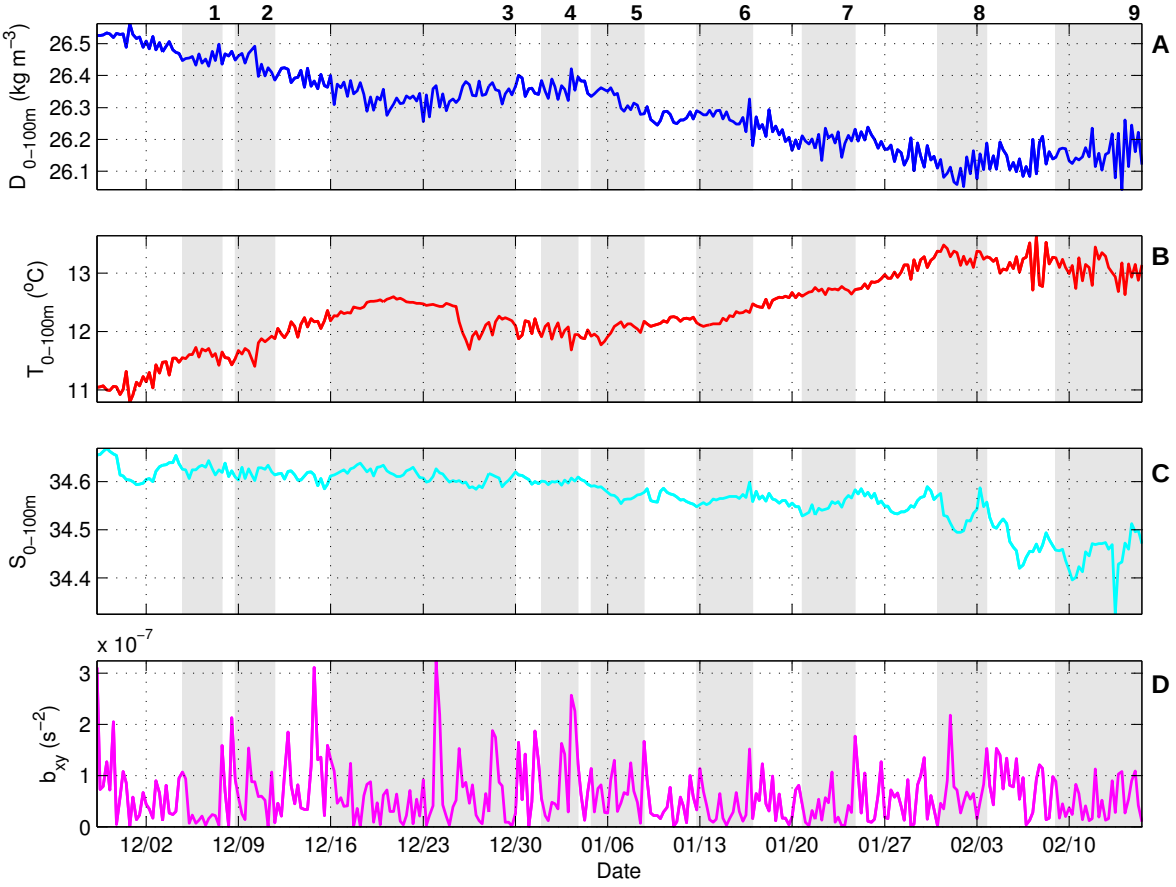

Figure 4.21: Summer time series for the ML properties (averaged in the upper 100 m) of A) density ($kg\ m^{-3}$), B) temperature (°C) and C) salinity. D) the lateral buoyancy gradient (s^{-2}).

4.4.1 Sub-seasonal MLD variability

Despite the restraint on mixing to comparable depths of spring, there is still a notable amount of sub-seasonal variability of the MLD, such as the period of 6 - 13 January, where the MLD deepens to its maximum summer depth of 90 m and shoals back to approximately 20 m before deepening back past 50 m. This does not seem to be related to the variability of water masses as there is only one instance where a sharp deviation in the T_{0-100m} occurs (25 December) (Figure 4.21B).

The destabilising effect of wind-induced turbulence indicates a noteworthy amount of sub-seasonal variability $0.14 \pm 0.09\ N\ m^{-2}$ and it is speculated that it amplifies the variability of

the MLD as wind stress modulates. Additionally, the variations in the MLD suggest characteristics of sub-mesoscale lateral buoyancy adjustment, such as 8 December and 10 January, where the MLD shoals by 40 m and 70 m in just one day respectively.

Decomposing temporal modes of variability

In order to decompose the sub-seasonal variability of the MLD and atmospheric parameters in terms of a modulating time scale, an EMD is imposed on the summertime wind stress, MLD and Q_{net}. For the wind stress and MLD summer time series, 6 Intrinsic Mode Functions (IMFs) were identified, while for Q_{net} there were 5 IMFs. An example of the 5 IMFs of Q_{net} produced by the EMD is shown in Figure 4.22.

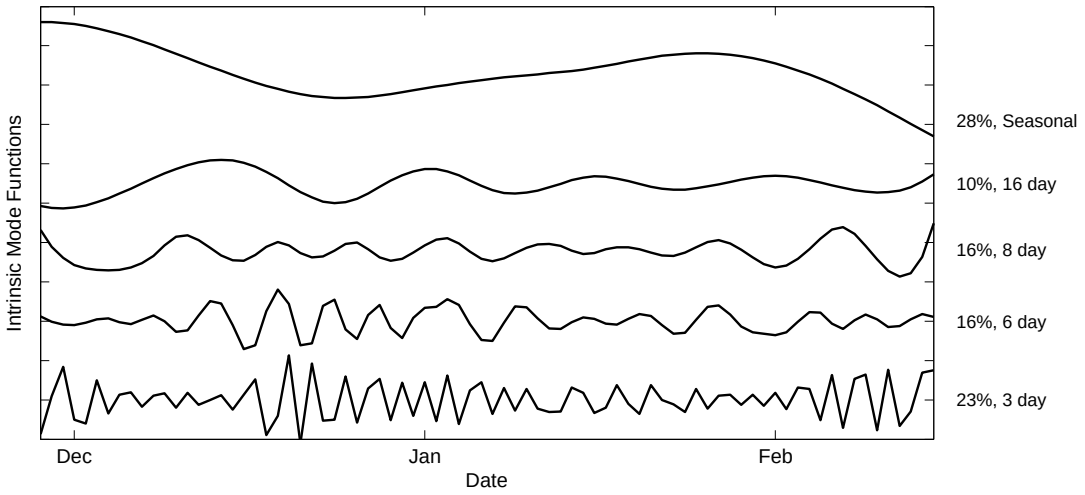

Figure 4.22: Five different modes of variability (IMFs) identified using an EMD on the Q_{net}. The percentages of the r^2 values, which explain the amount of variance as well as the temporal modulation are shown to the right of each respective IMF. Each correlation is found to be significant above the 99% confidence interval.

The temporal modulation of the IMF as well as the square of the correlation (r^2), represented as a percentage, is indicated in Table 4.1. All correlations are significant above the 99% level.

In all three EMDs, the lMF pertaining to the longest mode of variability is ignored as it represents the seasonal mode and does not indicate any sub-seasonal variability.

#IMF	Q_{net}	MLD	Wind stress
1	3 day (23%)	1 day (15%)	1 day (10%)
2	6 day (16%)	1.5 day (15%)	1.5 day (6%)
3	8 day (16%)	3 day (11%)	4 day (28%)
4	16 day (10%)	6 day (6%)	8 day (19%)
5		15 day (4%)	17 day (12%)

Table 4.1: Temporal modulations and the respective square of the correlation percentage (r^2, significant above the 99% level) defining explained variance for each of the IMFs (except seasonal) calculated for Q_{net}, wind stress and MLD over the summer period of sampling for SG573.

The EMDs for MLD and wind stress identified 5 sub-seasonal IMFs, while Q_{net} captured 4. The reason Q_{net} identified one less IMF is likely because the EMD was performed on the mean daily product for Q_{net}, therefore missing variability occurring at the diurnal scale, which was picked up by both the MLD and wind stress. There is not one particular IMF, and therefore temporal mode of variability, that dominates the explained variance in the atmospheric forcing parameters. The IMFs occurring at the synoptic scale of variability, however, seem to be more coherent than others (16% in the 6- and 8-day Q_{net} IMFs and 28% and 19% in the 4- and 9-day wind stress IMFs with a minimum of 6% in the 1.5-day wind stress IMF). The synoptic scale IMFs for the MLD do not suggest agreement with the atmospheric forcing parameters (11% and 6% in the 3- and 6-day IMFs), with strongest agreements found in the 1- and 1.5-day IMFs (15%). The synoptic scale IMFs are plotted against their respective time series in Figure 4.20A, C and D.

Through visual comparison, the 6-day Q_{net} IMF and 4-day wind stress IMFs agree well with their respective time series. Certainly for almost all occurrences of the 4-day modulation in wind stress, the IMF captures an increase in the τ by approximately 0.1 $N\ m^{-2}$ or more. However, on two occasions, namely around 12 December and 23 January, the IMF captures more peaks in the wind stress than there are storms. If the two 'over-capturing' peaks are ignored, the IMF is likely to be modified to a 5-day mode. This 4- to 5- day mode of variability

in the wind stress relates similarly to the storm variability of the Southern Ocean as observed by Patoux et al. (2009) and additionally, a visual inspection suggests that it is more coherent with changes in wind stress than the 6-day IMF does with Q_{net}. Therefore, this result of 'best-fit' in the 4-day (28%) wind stress IMF supports synoptic scale variability explaining a notable amount of sub-seasonal variability compared with changes in Q_{net}.

4.4.2 Wind deepening events

During the summer period, 9 occurrences are identified whereby the MLD deepened to below 50 m, indicated by shaded grey areas in Figure 4.20C. The outer limits of the grey shaded events indicate when the MLD began to deepen to past 50 m and when it shoaled above 50 m. Barring an extended event of 14 days, which occurred between 16 December and 30 December (third from left), the mean length of the events is 4 days.

In all events, the wind stress increased to above 0.2 $N\ m^{-2}$, with the mean values of wind stress and MLD for each event compared in Figure 4.23. In general, an increasing wind stress relates to deepening of the MLD with some variance around the lower wind stress values. A linear regression applied to the scatter with a squared correlation value of $r^2 = 0.76$ (significant to within the 99% level) suggests that on an event scale, the wind stress is able to explain 76% of the variability of the MLD. The mean Q_{net} over each respective event shows indication that stronger winds are associated with less heat entering the ocean. Event 9 indicates otherwise, with the lowest Q_{net} from all events (mean of 52 $W\ m^{-2}$ for the event) and a relatively strong wind stress of 0.15 $N\ m^{-2}$. This is likely due to the upper water column experiencing the strongest pre-existing stratification ($11.7 \times 10^{-5}\ s^{-2}$) in comparison to the other 8 events (second strongest is event 8 with $9.8 \times 10^{-5}\ s^{-2}$). For events marked 1 and 2 (Figure 4.20), wind stress values of 0.24 $N\ m^{-2}$ and 0.4 $N\ m^{-2}$ are synonymous with the MLD deepening from 40 m to 57 m and from 33 m to 52 m respectively. Despite a stronger wind stress during the second event, the MLD was unable to penetrate as deep as the first event, possibly due to an increase in the pre-existing surface layer stratification ($>2 \times 10^{-5}\ s^{-2}$).

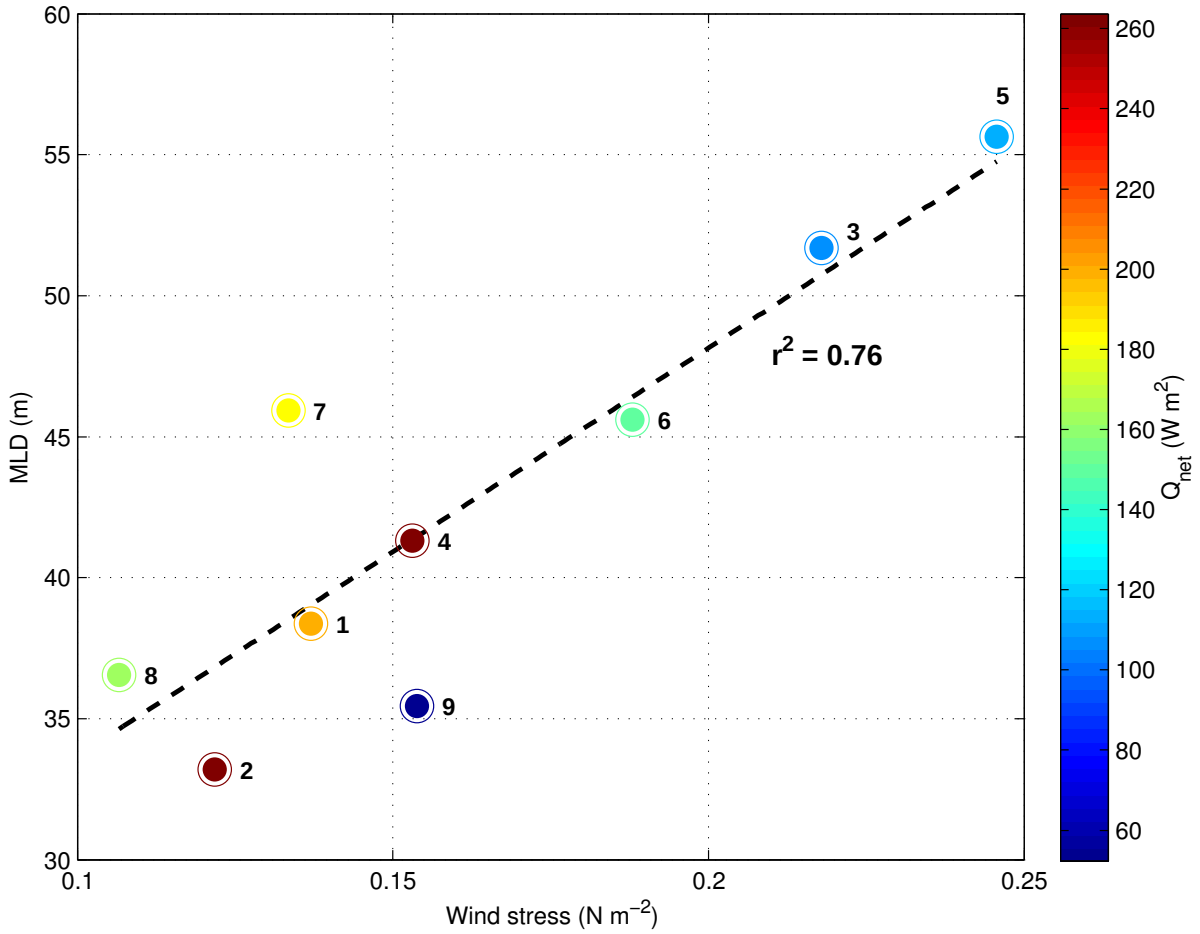

Figure 4.23: Scatter comparison of the average wind stress and MLD values for each of the nine events described in Figure 4.20. Averaged values are taken from when the MLD began to deepen to when the MLD shoaled the post wind event. The colour represents the mean Q_{net} over the event periods. Black dashed line indicates the linear regression applied to the scatter with an explained variance of $r^2 = 0.76$, significant to the 99% level. Event numbers corresponding to Figures 4.20 and 4.21 are shown to the right of each event.

Sustained mixing along a front

The passing of a storm (16 December, event 3) saw an increase in wind stress from 0.09 $N\ m^{-2}$ to 0.26 $N\ m^{-2}$ in one day, weakening the N^2_{0-100m} by $\sim 4\ \times 10^{-5}\ s^{-2}$. This corresponds to the MLD deepening from 27 m to 69 m in the same period. Throughout the event (16 - 30 December), 3 more storms are observed (0.29, 0.43 and 0.35 $N\ m^{-2}$ on 21, 25 and 30 December) along with 3 periods in between the storms whereby the wind stress decreased to 0.05, 0.06 and 0.12 $N\ m^{-2}$ respectively. Despite the intermittent decreases in wind stress, the MLD remains deeper than 30 m (mean of 52 m) throughout, where previously the MLD

shoals to 20 m after the storm.

To understand this better, a map of the mean SST overlaid with the mean wind stress and direction during the period of the event (16 - 30 December) is shown against the location of the glider (Figure 4.24). Contours of SST indicate the mesoscale frontal setting, with a meridional gradient of warmer water to the north, and colder water to the south. The black arrows in Figure 4.24 suggest that the mean wind direction is down-front, inline with the surface velocities indicated by the light grey arrows. The sampling locations during this period (larger dots on Figure 4.24) shows that the glider tracts along the front and during this time the lateral dive distance increases, suggesting the sampling of intense horizontal flow at the front.

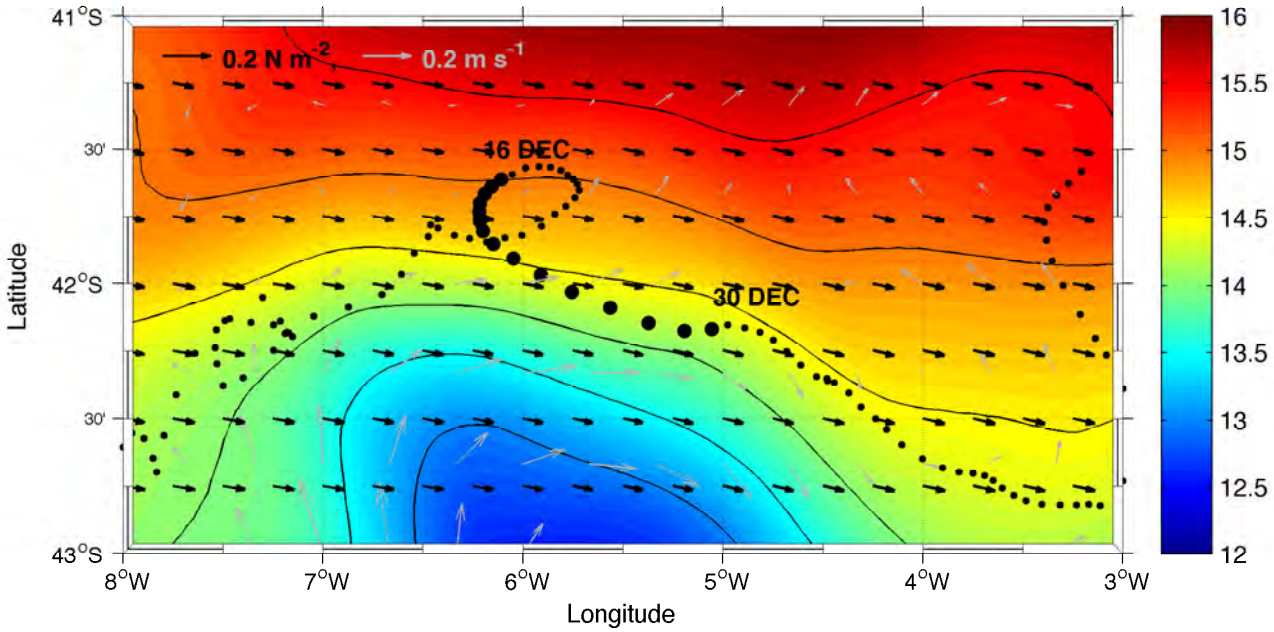

Figure 4.24: Mean SST for the period of 16 - 30 December in colour with mean wind direction and stress for the same period shown by the direction of the black arrows. The mean surface velocities are shown in light grey arrows. Dots indicate SG573 profile locations with larger sized dots showing the sampling period 16 - 30 December.

Aside from one occurrence on 24 December, there are no particularly large lateral buoyancy gradients compared to the rest of the summer period. With the set-up of the front having

colder (likely heavier) water to the south and warmer (likely lighter) water to the north, along with a down-front wind direction, theory suggests that the overturning of denser poleward water over lighter equatorward water keeps the ML well mixed through Ekman surface advection (Mahadevan et al., 2010). The total length of the front measured during the two weeks is 165 km. Vertical buoyancy flux calculations are applied with the mean parameters across the front: $b_{xy} = 0.59 \pm 0.75 \times 10^{-7}\ s^{-2}$, $\tau = 0.22 \pm 0.09\ N\ m^{-2}$, $MLD = 52 \pm 11\ m$, $Q = 106 \pm 273\ W\ m^{-2}$ and $f = 1.33 \times 10^{-4}\ s^{-2}$ result in $\langle w\prime\, b\prime \rangle_e < \langle w\prime\, b\prime \rangle_{cool} + \langle w\prime\, b\prime \rangle_w$. This indicates that wind-induced overturning at the front ($\langle w\prime\, b\prime \rangle_w$) overcame restratification and is the likely explanation for the consistently deep MLD during event 3. It cannot be explained by surface cooling as the ocean is gaining heat.

On 24 December, a lateral buoyancy gradient of $b_{xy} \sim 3.2 \times 10^{-7}\ s^{-2}$ was sampled which was the largest during both seasons. Buoyancy gradients similar to this magnitude have been shown to result in ML eddy-induced restratification in the spring. However, during event 3 the ML remains well mixed with no noticeable increase in the N^2_{0-100m}. Buoyancy flux calculations using the parameters across the profiles on 24 December: $b_{xy} = 3.2 \times 10^{-7}\ s^{-2}$, $\tau = 0.14\ N\ m^{-2}$, $Q = 44\ W\ m^{-2}$ and $MLD = 53\ m$, show that $\langle w\prime\, b\prime \rangle_e < \langle w\prime\, b\prime \rangle_{cool} + \langle w\prime\, b\prime \rangle_w$, thereby wind-driven overturning overcoming restratification and keeping the MLD from restratifying. If the vertical buoyancy flux equations are rearranged so that $\langle w\prime\, b\prime \rangle_w = \langle w\prime\, b\prime \rangle_e < \langle w\prime\, b\prime \rangle_{cool}$, the wind stress would need to decrease to 0.06 $N\ m^{-2}$ in order for the ML to restratify under same lateral buoyancy gradient.

Rapid restratification post wind-induced deepening of the MLD

Beginning 1 January (event 4), an increase in wind stress from 0.08 $N\ m^{-2}$ to 0.24 $N\ m^{-2}$ in two days resulted in a deepening of the MLD from 30 m to 58 m in 12 more hours. A tail of restratification above the seasonal pycnocline shoals the MLD from 58 m to 23 m in one day (3 January, Figure 4.19D). It occurs synonymously with a relaxation of wind stress to 0.15 $N\ m^{-2}$ at the lateral crossing of a buoyancy front of $b_{xy} \sim 2.2 \times 10^{-7}\ s^{-2}$.

Figure 4.25 shows the evolution of the vertical density profiles from 1 January, when the wind began to increase, to 4 January, where restratification occurs at 23 m. Vertical buoyancy

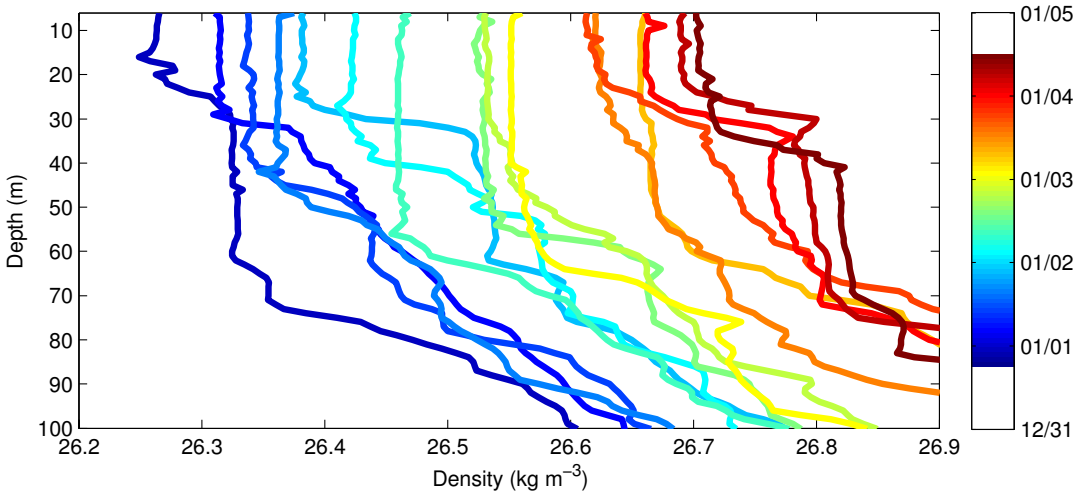

Figure 4.25: Vertical density profiles of SG573 for the period of 1 - 4 January. An increase from blue to red indicates the time progression of isopycnals in chronological order. The isopycnals have been offset by 0.03 $kg\ m^{-3}$ to the right for clarity and represent the time evolution of the 6-hourly spaced profiles.

flux calculations using the parameters across the buoyancy front of 6.6 km over the period of one day: $b_{xy} = 1.7 \pm 0.9 \times 10^{-7} s^{-2}$, $\tau = 0.15 \pm 0.02\ N\ m^{-2}$, $Q = 330 \pm 249\ W\ m^{-2}$ and $MLD = 42 \pm 16\ m$ indicate that $\langle w\prime\, b\prime \rangle_e < \langle w\prime\, b\prime \rangle_{cool} + \langle w\prime\, b\prime \rangle_w$. This suggests that wind-driven overturning should destratify the ML. However, restratification is observed likely due to the spin-off of sub-mesoscale instabilities causing the wind direction to be misaligned with the frontal axis. By equating $\langle w\prime\, b\prime \rangle_w$ to $\langle w\prime\, b\prime \rangle_e + \langle w\prime\, b\prime \rangle_{cool}$ under the same conditions as above except the wind stress, it is found that a down-front wind stress of 0.12 $N\ m^{-2}$ is required to keep the front destratified.

The deepest MLDs of the summer period occurred during the event 5 (90 m) with a strong wind stress maximum of 0.36 $N\ m^{-2}$ destroying the tail of restratification, pushing mixing down to the seasonal pycnocline. Despite the wind stress subsiding to ~0.08 $N\ m^{-2}$, the ML remains deeply mixed for another day when again restratification of the ML generates a shoaling of the MLD as a tail of stratification above the seasonal pycnocline on 12 January. In this instance, even if the wind direction was aligned down-front, the vertical buoyancy flux calculations using the parameters at the date of restratification: $b_{xy} = 0.8 \times 10^{-7}\ s^{-2}$, $\tau = 0.08\ N\ m^{-2}$, $Q = 221\ W\ m^{-2}$ and $MLD = 90\ m$ show that $\langle w\prime\, b\prime \rangle_e > \langle w\prime\, b\prime \rangle_{cool} + \langle w\prime\, b\prime \rangle_w$,

allowing restratification of the ML. The extended lag of deep MLDs after the wind stress subsided on 8 January is possibly due to the lack of lateral buoyancy gradients present at the time. This suggests that without the presence of strong lateral buoyancy gradients, the MLD requires more time to shoal when the wind relaxes than would be the case when lateral buoyancy gradients are present.

From the event 6 (13 January), a break down of the restratification and an uplift of the seasonal pycnocline to the base of the MLD (Figure 4.19D) means that a relatively strong wind stress of 0.36 $N\ m^{-2}$ was only able to generate mixing down to 60 m, 30 m shallower than the previous event. Despite this, rapid restratification of the MLD to $\sim$20 m occurs approximately a day after the wind relaxes from 0.32 $N\ m^{-2}$ to 0.08 $N\ m^{-2}$ in 12 hours. A similar process occurs over the final three events, where the seasonal pycnocline is pushed down with the increase in wind stress. In each case, restratification occurs roughly one day after the wind stress decreases. During this time, the seasonal pycnocline increases in strength, with N^2_{0-100m} rising from $\sim$5 $\times 10^{-5}\ s^{-2}$ on 20 January to a maximum of $\sim$13 $\times 10^{-5}\ s^{-2}$ on 10 February. This is speculated to be due to continued positive Q_{net} (166 $\pm$ 98 $W\ m^{-2}$) as the T_{0-100m} increased by 1 $^{\circ}C$ over the same period. The increase in surface stratification and shoaling of the seasonal pycnocline (Figure 4.19D) to $\sim$25 m inhibits mixing to a maximum of depth of 53 m, despite the wind stress reaching 0.32 $N\ m^{-2}$.

4.4.3 Lag correlating wind stress to MLD

Based on the general agreement between increasing wind stress and decreasing MLD, a lag correlation shows a maximum positive correlation of $r = 0.51$ significant to above the 99% level after an 18 hour lag. It is worth noting that the maximum correlation during spring is within the first 6 hour period, with $r = 0.24$. This shows that an increase in the mixing depth is in best agreement with an increasing wind stress after a lag of 12-18 hours. The square of the correlation gives $r^2 = 0.26$, indicating that the wind stress variability explains 26% of the variance of the MLD after 12-18 hours.

The relationship between the wind stress and the MLD after the time lag at the maximum correlation for each season (no lag for spring, 12-18 hours lag for summer), is shown in

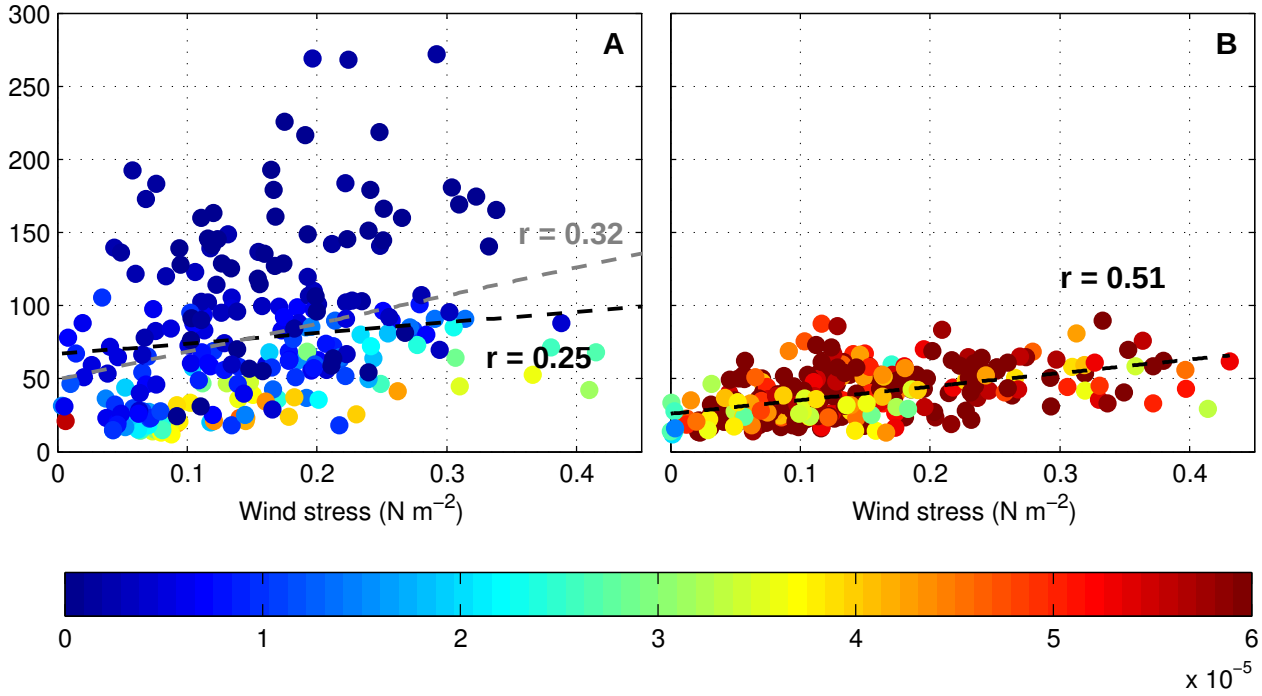

Figure 4.26: Regressions of the wind stress ($N\ m^{-2}$) and MLD (m) at the maximum lag correlation for both spring (A, $r = 0.25$, $p < 0.001$) and summer (B, $r = 0.51$, $p < 0.001$). Regression lines are shown as dashed black lines. Colour indicates N^2_{0-100m} (s^{-2}) at the time of each wind stress measurement. Dashed grey line indicates the regression ($r = 0.32$, $p < 0.001$) line for the springtime maximum lag correlation that ignores 6 data points pertaining to the largest wind event on 8 November.

Figure 4.26. The N^2_{0-100m} corresponding to the time of the wind stress is considered to be the pre-existing stratification of the respective wind forcing, and is shown as the colour of the respective data point in Figure 4.26. The linear regressions that encompasses all data points during each season (black dashed lines) suggest similar gradients, although there is a great deal more scatter between wind stress and MLD in spring compared to summer (Figure 4.26B). The gradient of the linear regression during spring has been decreased a result of 6 data points pertaining to the large wind stress values (>1.2 $N\ m^{-2}$) around 8 November (Figure 4.20D). These values are subsequently removed, improving the correlation to $r = 0.32$. The gradient of the linear regression indicates a more realistic balance between weakly stratified deep MLDs and more strongly stratified shallow MLDs (Figure 4.26A). Interestingly, the strength of the pre-existing stratification within the upper 100 m seems to exert a considerable control on the depth of wind-driven mixing. It indicates that if the surface stratification is $>1.1 \times 10^{-5}$ s^{-2} at the time of wind stress, the MLD is unable to deepen past 100 m, no matter if this

happens in the spring or summer periods. During spring, the maximum correlation between wind stress and MLD ($r = 0.25$, $p < 0.001$) occurs after no time lag. This implies that wind-induced mixing in the spring is significantly more responsive than during summer. A likely reason for this is the much weaker surface stratification in spring compared to summer which leads to a quicker and enhanced response of the surface ocean to surface wind stress.

Discussion

The SAZ is currently understood to be region of high primary productivity where phytoplankton blooms photosynthetically fix carbon at globally important rates (Thomalla et al., 2011). Springtime increases in light, combined with a weakening of the surface forcing and shallowing of the MLD means that phytoplankton are retained above the surface light level, promoting rapid growth. Therefore, investigating the physical forcing mechanisms that explain the onset of springtime restratification as well as its subsequent sub-seasonal variability into summer has significant implications in determining estimates for upper ocean primary productivity. This is especially important in predicting the impacts of a changing climate on the biogeochemistry, and subsequent carbon export (Sarmiento et al., 2004; Monteiro et al., 2011; Swart et al., 2014). Recent work in both the modelling and observational regimes are beginning to emphasise the importance of sub-mesoscales in generating the initial springtime onset of restratification (Fox-Kemper et al., 2008, Lévy et al., 2009, Taylor and Ferrari, 2011, Mahadevan et al., 2012b). However, these ideas have yet to be tested in Southern Ocean observational studies. In addition, understanding the physical-biological coupling of wind-induced mixing and sustained Southern Ocean phytoplankton growth at sub-seasonal scales is becoming increasingly important during summer, when productivity is limited due to nutrient depletion (Fauchereau et al., 2011; Swart et al., 2014). These findings promote a need for sampling at the sub-meso and sub-seasonal scales, which are often too difficult to observe as their spatial (1-10 km) and temporal scales (from a few hours to a few days) are too rapid and fine scale to observe using traditional measuring platforms, such as ships, floats and satellites.

Recent developments in autonomous ocean glider technology (Eriksen et al., 2001) have shown their ability to sample at these necessary scales (Mahadevan et al., 2012b; Olita et al., 2014). An experiment was performed whereby Seaglider observations from the SAZ provided >5.5 months of high spatial and temporal resolution hydrographical data, which has proved to be a significant improvement when compared to an alternative time and space sampling platforms such as of Argo floats (Figure 4.1). A power density spectrum of near surface density characterises the length scales of the hydrographic features from the glider observations (Figure 4.7). Mesoscale features dominate with lengths ∼100 km with a spectrum slope

lying between -2 and -5/3. This indicates that within the mesoscale, there is a transition down to the sub-mesoscale in the horizontal density structures (Capet et al., 2008). As the varying horizontal dive distance of the glider (0.2-7 km range) spans the majority of the sub-mesoscale regime (<10 km), it generates some uncertainties around the resolution of the variability resolved. Rudnick and Cole (2011) identifies that although glider observations are a significant improvement from ship measurements for high frequency variability, they can only accurately resolve features exceeding 30 km. This is true in that gliders are slow moving platforms (33 $cm\ s^{-1}$ average for this study) and can contain aliasing of data when the rate of development and displacement of the feature/structure studied is fast relative to dive time and/or the glider is sampling in a different direction to the feature, thus exiting the feature and sampling a contrasting structure with different properties. Thus, careful consideration is given to when not isolated events are analysed and ML variability is not necessarily due to external forcing but rather a product of the glider sampling two separate features. However it is also noted that the 2.5 hour mean dive distance of SG573 falls well within the evolutionary period of oceanic sub-mesoscale structures (order of a few days, Fox-Kemper et al., 2008), and that the first baroclinic Rossby radius of deformation similar to that of Chelton et al. (1998) (Figure 4.8) revealed that the scale at which sub-mesoscale features develop is well above the mean dive distance of glider observations (2.9 $km \pm 1.5\ km$). Therefore, the glider observations are assumed to be associated with ML eddies (Figures 4.9 and 4.10) and that the determination and evolution of density/buoyancy fronts over the period of a few days is analysed by focusing on certain events that lead to variability of stratification and the MLD. This is particularly important when analysing events in this work as numerous profiles are considered when discussing the evolution of ML eddies. Therefore, the fine sampling scales of this study that are necessary to determine the interplay between meso- to sub-mesoscale surface features are achieved with the recognition that the evolution of meso- to regional-scale frontal features in both space and in time may crossed by the glider (Figure 4.3), thereby easily misinterpreting the ML variability as either a spatial or temporal change in water mass properties. This analysis followed the isolating of specific events that were influential in MLD variability and the stratification dynamics attaining to it, independent analysis was performed and the space-time bias was negated.

The complete glider dataset of 144 days was separated into two periods, depicted by contrasting upper ocean physics (Figure 4.2). The spring and summer periods had characteristically different upper ocean hydrography which has significant implications on the vertical stratification dynamics, and therefore the variability of the MLD.

Spring: ML eddies drive stratification

The spring period, which encompassed the first 64 days of the experiment, was characterised by generous amounts of variability in the ML temperature ($\sim$2 $^{\circ}C$) and salinity ($\sim$0.5). Weak stratification of the upper 100 m resulted in a high MLD range that displayed typical excursions characteristic of both deep winter MLDs (272 m) and shallow summer MLDs (12 m) in the SAZ (Rintoul and Trull, 2001; Dong et al., 2008; Sallée et al., 2010) (Figure 4.1A). Increases in the surface stratification occurred when a new layer of enhanced stratification was generated at around 20 m depth, well above the seasonal pycnocline. This was observed when the N^2_{0-100m} increased by 1-3 $\times$ 10^{-5} s^{-2} day^{-1} and lasted between $\sim$1 day (*e.g.* 6 October) to >1 week (*e.g.* 28 October - 4 November). The generation of new surface stratification was often associated with large rates of rapid restratification as deep MLDs (>100 m) would shoal to the layer of restratification, such as 6 October and 16 November where the MLD shoaled by 157 m and 90 m in one day respectively (Figure 4.11D). These rates of restratification cannot be explained by surface heating alone and agree well with the rapid MLD adjustments that were found in the observations of springtime restratification due to ML eddies (Mahadevan et al., 2012b).

Mahadevan et al. (2012b) state that when surface buoyancy forcing is greater than -100 W m^{-2}, the environmental conditions are conducive to sub-mesoscale lateral buoyancy adjustments. This occurred in the form of an eddy overturning buoyancy flux that was parameterised by Fox-Kemper et al. (2008). In this work, the ML eddy-induced overturning flux was postulated to generate the rapid restratification as surface heating was above -100 W m^{-2} for the experiment (Figure 4.1B). It was hypothesised that increases in wind stress above the level at which the lateral buoyancy gradients are important destabilised the near surface stratification

and generated convective mixing (Taylor and Ferrari, 2010). Therefore, this study brought forward the idea that within the SAZ, a competition exists between the stratifying effects of positive surface heating and ML eddy restratification against destratifying effects of surface buoyancy loss and wind-induced mixing, such as is the case in the North Atlantic (Mahadevan et al., 2012b).

Similar to the North Atlantic study (Mahadevan et al., 2012b), a general decline in the near surface density occurred throughout the experiment, albeit theirs is due to a latitudinal decrease in density, while in this study it was primarily due to seasonal heating (Figure 4.9). Nevertheless, in both cases, sharp gradients in the near surface density were observed over the period of around a day and within a few kilometres. These occurred as elevated lateral buoyancy gradients (b = -$g(\rho$ - $\rho_0)/\rho_0$) (Figure 4.12D) in the presence of mesoscale frontal features (Figures 4.14A and B and 4.16). In these instances, quantitative analysis of the competition between vertical buoyancy flux overturning by ML eddies, surface buoyancy forcing and a down-front wind stress using parameterisations developed by Fox-Kemper et al. (2008) showed that in the presence of large buoyancy gradients (0.36 to >2 $\times$ 10^{-7} s^{-2}) in combination with strong seasonal heating (162-201 W m^{-2}), the environmental conditions were suitable for restratification of the ML. This was despite wind stress values of up to 0.13 N m^{-2}. The process of ML eddy restratification explained the rapid shoaling of the MLD on 6 October and 16 November in addition to a layer of elevated stratification that occurred between 7 and 16 October. It is worth noting that without satellite products of sufficient resolution that were required to identify the direction of the sub-mesoscale flow field frontal axis relative to the wind direction, the wind direction was assumed to be down-front as this avoids biasing in favour of ML eddies. The evolution of the vertical density profiles illustrated that at the lateral buoyancy fronts, the well-mixed vertical density profiles tilted towards the horizontal (Figures 4.14C and 4.18) and generated stratification, increasing the N^2_{0-100m} up to 3 $\times$ 10^{-5} s^{-2} day^{-1}.

The restratifying effects due to ML eddies were opposed by elevated wind conditions that destabilised the stratification. Storms with wind stress values in the order of 0.3 N m^{-2} or

greater (shown as the second, third and last shaded grey areas in Figure 4.12C) weakened the vertical stratification to 1×10^{-5} s^{-2}, even while in the presence of strong lateral buoyancy gradients of 2×10^{-7} s^{-2} (*e.g.* 8 November). The variability of the MLD in response to the increased wind stress was not linear as it depended on the strength of the stratification that underlies the MLD as well as the wind stress itself. This was exemplified in two contrasting wind events between 16 - 22 October and 7 - 10 November. The former event was characterised by low ML stratification, which was destroyed within a day when the wind stress increased to above 0.2 N m^{-2} with the response of the MLD deepening to (the maximum observed) 272 m. In contrast, event 2 was characterised by strong stratification four times larger than the former event, whereby a wind stress of 1.2 N m^{-2} (seasonal maximum observed) was only able to weaken the ML stratification thereby maintaining the MLD to the upper 100 m.

Summer: synoptic scale wind and ML coupling

In summer, there is a threefold decrease in ML salinities and temperature variance (Figure 4.5). The summer MLD is therefore almost completely controlled by the changes in the thermocline, with the band of stratification that forms the seasonal pycnocline and base of the MLD increasing, making it more difficult for mixing effects to penetrate through this layer and deepen the MLD to the comparable depth of spring (Figure 4.2B, D). Despite this control of ML variability from changes in the thermocline, the MLD is still observed to undergo rapid restratification rates of >40 m day^{-1}.

For the remainder of the time series, the seasonal southward progression of surface heating (Figure 4.3B) due to the persistence of a positive incoming solar radiation (Figure 4.1B) warmed the surface ocean and increased the surface buoyancy by raising the ML temperature from ~ 9 $^{\circ}C$ in the spring (Figure 4.13B) to ~ 13 $^{\circ}C$ in the summer (Figure 4.21B). This intensified the thermal gradient between the warmed surface waters and colder deeper water and thereby strengthened the thermocline and vertical stratification. A merging of the seasonal pycnocline and the MLD (Figure 4.2D) meant that negative buoyancy forcing no longer had to penetrate through a tail of restratification, but rather an enhanced stratification maximum. This suggested that in order for the MLD to reach depths comparable to spring, it had to

break through more intensified stratification, thereby requiring stronger mixing terms. As a result, the MLD remained shallower than 100 m as the amplitude of MLD variability was significantly reduced (Figure 4.2).

In this study, 9 events were observed where the wind stress increased above 0.2 Nm^{-2} and lead to the MLD deepening from ∼20 m to below 50 m. The temporal modulations of these 9 events related well to the synoptic scale period of storms in the Southern Ocean (Trenberth, 1991; Parish and Bromwich, 1998), where similar modes of variability were observed in the wind stress, heat flux product and MLD. The coherence between wind stress and heat flux was likely due to the development of clouds during storm events. Typically, this would result in an increase in reflectance of incoming shortwave radiation thereby decreasing the Q_{net}. Additionally, the decrease in the Q_{net} was likely to decrease the air temperature at the air-sea interface, which could have resulted in cooling of the ocean (when $T_{air} < T_{sea}$). Furthermore, an increase in the wind stress could have allowed for further evaporation and heat loss from the ocean. However, further *in-situ* measurements of T_{air} and other atmospheric parameters were required for a more conclusive analysis.

At the event scale, the relationship between the strength of the wind stress and the MLD agreed well ($r^2 = 0.76$), whereby stronger winds generated a deeper MLD. However, this relationship decreased ($r^2 = 0.26$) when compared to direct point on point values, which was because the MLD lagged the wind by 12-18 hours. The decline was likely further enhanced due to inaccuracies in satellite sampling of the wind stress product in addition to ML eddies that remained ubiquitous during the summer and complicated the MLD. When the storms passed and the wind stress decreased to below 0.2 $N\ m^{-2}$, the alignment of the wind direction and lateral buoyancy frontal axis became important. In the presence of a down-front wind at intensified surface flow, the MLDs remained deep due to wind-induced overturning, while rapid restratification of the MLD of over 40 $m\ day^{-1}$ could occur if the wind direction was misaligned with the frontal axis and the buoyancy gradient was strong enough to allow ML eddy overturning (*e.g.* 3 and 12 January).

This relationship between wind stress and MLD was more cohesive in the summer months in comparison to the spring. This was not surprising given that during spring, weak stratification of the upper 100 m ($<1.1 \times 10^{-5}\ s^{-2}$) meant that the MLD deepened well below 100 m. This did not apply to a specific threshold of wind stress, as long as the pre-existing stratification was weak. In summer, the stratification of the upper 100 m was persistently greater than $1.9 \times 10^{-5}\ s^{-2}$, and therefore the MLD remained above 100 m for the entire season, even in the presence of wind stress of over 0.4 $N\ m^{-2}$. This meant that the linear regression during summer was notably more well fitted to the scatter than during spring, where a balance was found between the weakly stratified deep MLDs and more stratified ($>1.1 \times 10^{-5}\ s^{-2}$) shallow MLDs. This was seen as an improvement in the maximum lag correlation from $r = 0.32$ in spring to $r = 0.51$ in summer.

Additionally, in summer the maximum wind-MLD lag correlation occurred after 12 - 18 hours, whereas for spring the maximum correlation occurred at no lag. This infers that during spring, the MLD was significantly more reactive to variations in the wind stress as there was less of a 'barrier' of stratification to break down. The value of $1.1 \times 10^{-5}\ s^{-2}$ for N^2_{0-100m} formed a threshold value that is repeatedly crossed during spring, allowing the MLD to either remain shallower or deepen well beyond 100 m, forming the environment for rapid restratification due to ML eddies, which then potentially increased N^2_{0-100m} to above the threshold value. This constant 'battle' between creating and destroying the upper ocean stratification during spring is likely to be relevant to phytoplankton growth in estimating the amount of time the MLD can remain shallow above the light level. However, further in-depth studies need to focus on the specific MLD depth required for phytoplankton to significantly grow and then further suggestions can be made as to what sort of stratification values do ML eddies contribute, which can help to quantify their importance.

Summary

The SAZ region of the Southern Ocean is ubiquitous with mesoscale activity (Orsi et al., 1995; Belkin and Gordon, 1996) and forms a meeting place for warmer water from the north and colder water from the south (Rintoul and Trull, 2001). This sets up large lateral gradients in density at the ocean surface. Model studies (Tandon and Garrett, 1994; Boccaletti et al., 2007; Fox-Kemper et al., 2008) and observational studies in the Northern Hemisphere (Mahadevan et al., 2012b; Olita et al., 2014) have shown that at the sub-mesoscale, restratification of the ML occurs when these lateral gradients are able to relax, with the lighter water advecting over the heavier water. This process of ML eddy restratification in the North Atlantic (Mahadevan et al., 2012b) has yet to be examined in the SAZ where similarly, the seasonal cycle is the strongest mode of variability in the climate forcing (Monteiro et al., 2011). In winter, the combination of low solar radiation and turbulent winds generate deep mixing, when during springtime, increased in solar radiation along with the availability of light and a shallowing of the MLD promotes rapid phytoplankton growth (Sverdrup, 1953). Currently, the physical processes dictating the onset of springtime stratification are not well understood in the SAZ, meaning that high sub-seasonal and sub-mesoscale variability in the physical processes driving stratification exist (Swart et al., 2014).

Recent models (Lévy et al., 2009) and observations (Fauchereau et al., 2011; Swart et al., 2014) have shown the importance of sub-seasonal wind forcing on deepening the MLD below the nutrient depth during summer, thereby sustaining summertime phytoplankton production. This calls for a need to better understand the relationship between wind forcing and MLD deepening as a change in climate could potentially lead to changes in summer MLDs, affecting nutrient supply to phytoplankton cells.

In order to fill the gaps in knowledge above, this study used data acquired from an autonomous Seaglider that spent 5.5 months during the spring and summer that sampled high resolution (average 1.4 km, 2.5-hourly) physical parameters in the SAZ (Swart et al., 2014). The hydrographic properties demonstrated the two seasonal regimes in upper ocean stratification: 1) Spring; characterised by strongly variable hydrographic properties that occurred

over the meso- to sub-mesoscale with weak upper ocean stratification and 2) Summer; the persistence of positive surface heating warmed the surface ocean which fostered a strong band of enhanced vertical stratification and inhibited deep mixing comparable to spring. This study was therefore split into spring and summer where sub-seasonal analysis was done separately.

1. Do sub-mesoscale ML eddies drive early springtime restratification in the SAZ?

In spring, the MLD shoaled from the deep winter mixing to depths characteristic of summer for 1-2 months before the onset of solar induced stratification. During this time, rapid rates of MLD shoaling (>100 $m\ day^{-1}$) occurred at sub-seasonal time and sub-meso space scales (<10 km). In early spring (before November), ML eddies developed in the presence of elevated lateral buoyancy gradients and restratified the MLD to around 20 m. However, the stratification defining the MLD was still reasonably weak $\sim 1 \times 10^{-5}\ s^{-2}$ with storm events able to destroy stratification and deepen the MLD to comparable depths of winter (272 m). With the progression of spring, the combination of a persistent positive surface warming and restratification of the MLD under large lateral buoyancy gradients generated sufficiently stronger surface stratification ($>3 \times 10^{-5}\ s^{-2}$), where strong storms were no longer able to deepen the MLD to the comparable depths of October. This was because once the surface stratification surpassed $1.1 \times 10^{-5}\ s^{-2}$, the MLD was unable to penetrate passed 100 m. Therefore, the balance of surface stratification around the $1.1 \times 10^{-5}\ s^{-2}$ threshold induced by ML eddies and positive buoyancy forcing applied considerable control on the MLD being characteristic of either deep winter/spring mixing (>100 m) or summer shallow mixing (<100 m).

2. At what sub-seasonal temporal scales do wind forcing and deepening of the MLD couple? Is there a quantified relationship between the two?

In summer, the persistently positive solar heating warmed the surface ocean by over 2 $^{\circ}C$ from spring, increasing the strength of the stratification $>1.9 \times 10^{-5}\ s^{-2}$. This enhanced the band of stratification, where wind stress >1.2 $N\ m^{-2}$ was unable to deepen the MLD below 100 m. This meant that MLDs remained above 100 m for the duration of summer. Despite the restriction on mixing depth in comparison to spring, storm events whereby wind

stress increased above 0.2 $N\ m^{-2}$ were able to deepen the MLD to below 50 m at a frequency around the synoptic scale (4-5 days). The best agreement in immediate point measurements between increases in the wind stress and deepening of the MLD was found after 12-18 hours. Interspersed between storms when the wind stress was low, the balance between ML eddies restratification and wind-induced overturning in the presence of a lateral buoyancy front explained either rapid shoaling of the MLD (>40 $m\ day^{-1}$) or sustained deep MLDs ∼50-60 m.

Relevance to carbon cycling and climate

During spring, restratification of the MLD to approximately 20 m by ML eddies is likely to provide an excess of light for phytoplankton cells. The amount of time this light is available before the layer of stratification is mixed again is dependent on the variability of wind stress and surface buoyancy forcing. In early November, the combination of surface heating and ML eddies generated intense surface stratification (>4 × 10^{-5} s^{-2}) at ∼20 m that lasted >1 week, occurring well before the onset of solar induced stratification (28 November). In comparison to the study by Mahadevan et al. (2012b), a similar process occurs whereby ML eddy restratification generates surface stratification of similar values (∼5 × 10^{-5} s^{-2}). This generated an ′early′ phytoplankton bloom, which is similar to what is observed in this dataset by Swart et al. (2014). This suggests that the timing of positive buoyancy forcing is important in addition to strong lateral buoyancy gradients, which are able to restratify the MLD and promote phytoplankton growth before the onset of solar induced stratification.

The transition to a highly stratified MLD in summer has key implication for primary production in terms of shoaling the MLD above the ferricline depth, thereby restricting the access of Fe to the ML (Thomalla et al., 2011). As summer progresses, phytoplankton growth is inhibited as nutrients are depleted. This work shows that wind events at the synoptic scale that surpass 0.2 $N\ m^{-2}$ deepen the MLD beyond 50 m. Swart et al. (2014) showed that during the summer period of this dataset, sustained phytoplankton productivity was observed. This suggests that the observed wind-MLD relationship is sufficient to sustain primary production throughout summer in the SAZ. Additionally, the potential for the deep MLDs (>50 m) to shoal rapidly under ML eddies can provide aid for phytoplankton cells as restratification at 20

m concentrates the cells within the enhanced light environment. These results indicate that the interplay between ML eddy restratification and wind-induced mixing could prove key in determining seasonal estimates of phytoplankton growth and carbon uptake.

Caveats and future work

Ocean gliders undoubtably offer an improved approach in monitoring fine-scale ocean processes. This study shows their adaptedness in sampling sub-seasonal and sub-mesoscale variability in the upper ocean. Despite this, the sampling strategy performed for SOSCEx was not designed to cross the main frontal features of the Southern Ocean, but rather a focus towards upper ocean physics and biological processes in the SAZ (Swart et al., 2012). I mention some caveats of this study and suggest improvements for future glider experiments and studies.

7.1 Assumptions in this study

The identification of lateral buoyancy gradients is key in determining restratification by ML eddies. Sampling with a glider provides complexities as the trajectory of the glider is not necessarily aligned to measure the maximum buoyancy gradient of a specific front (*e.g.* Figure 7.1). This can potentially result in a sub-optimal sampling of the maximum lateral buoyancy gradient of the front and the subsequent underestimation of the ML eddy overturning flux.

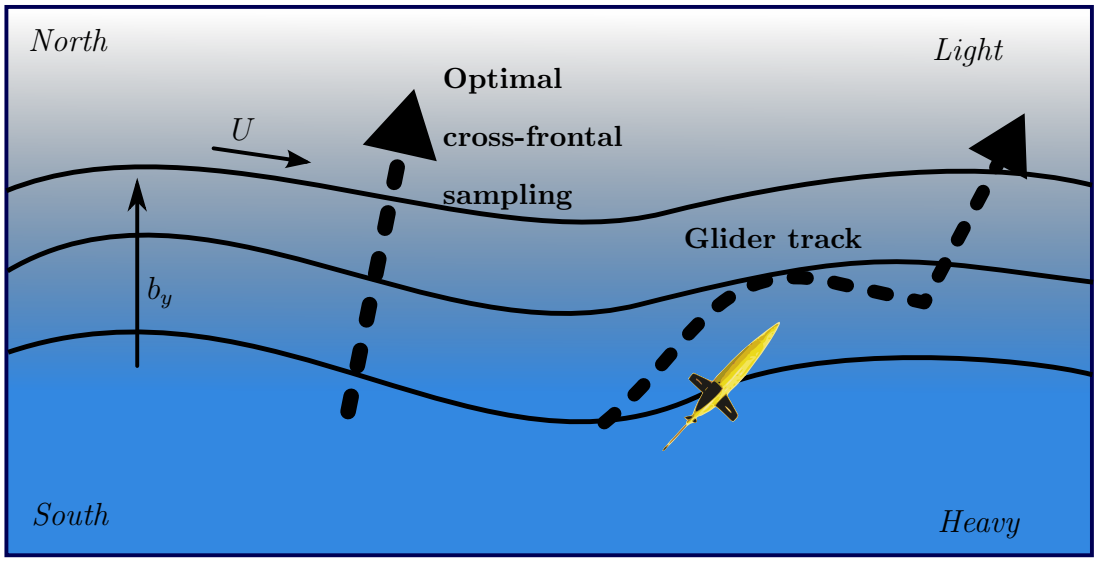

Figure 7.1: Optimal sampling of b_{xy} is directly across the front to measure the maximum lateral gradient in buoyancy. Glider sampling presents analysis complexities if the glider is not directed directly cross-frontal.

As the trajectory of the glider in this study is not consistently cross-frontal and the lateral distances of the glider dives are inconsistent, the optimal maximum lateral buoyancy gradient of the respective front may be misrepresented. Figure 7.2 shows that there is a uniform distribution of lateral buoyancy gradients with respect to dive distances. It is therefore assumed that there is no bias of lateral buoyancy gradient towards lateral dive distances. The strength of the lateral buoyancy gradients are able to accurately represent the strength of the ML front, thereby explaining restratification by ML eddies.

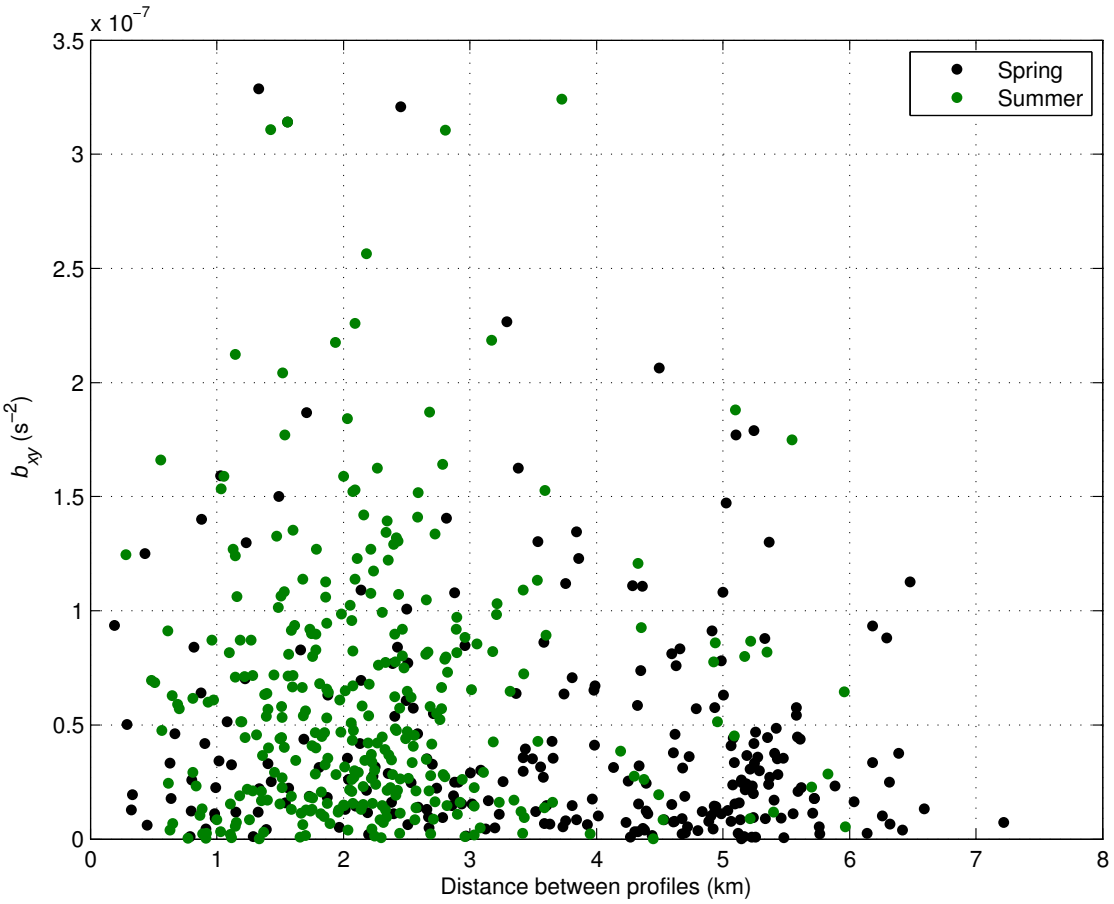

Figure 7.2: Test for bias of b_{xy} against the distance between the respective two SG573 profiles that measure the b_{xy}. Black dots indicate spring, while green dots indicate summer.

Interestingly, the distances between profiles is noticeably larger in spring (3.7 ± 1.6 km) compared with summer (2.2 ± 1 km). In summer, the problem of biofouling on the SG573 fairing (Figure 3.4), especially from the beginning of January reduced the dive efficiency and

therefore decreased the dive distance. Possible variances in piloting instructions to the glider is another likely reason for the dive distance discrepancy between seasons. Additionally, the difference in the depth averaged velocities acting either in the direction of the glider movement generating larger dive distances or against the glider movement reducing distances (Figure 7.3).

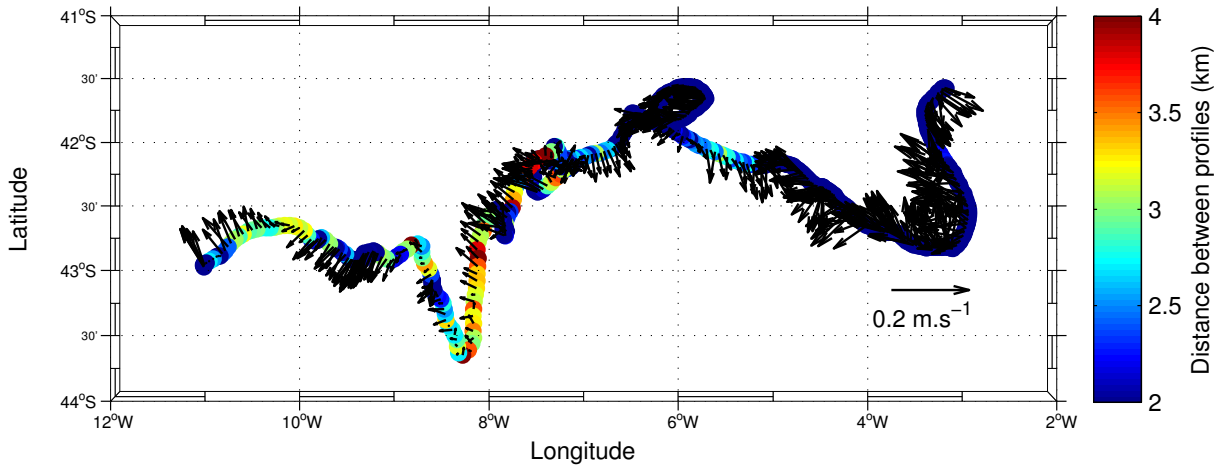

Figure 7.3: SG573 trajectory with colour scale indicating the lateral dive distance between profiles. Black arrows show direction of surface velocities acquired from SG573. Length of arrows are representative of their speed.

During summer a large period whereby the depth averaged current was against the glider trajectory could have further influenced the distances between profiles. However, future studies will have to take into consideration the surface jets propelling the glider when it is at the surface.

7.2 Potential future work

7.2.1 Identification of sub-mesoscale features

In addition to the restratification of the ML, sub-mesoscale processes also generate intense vertical velocities that are an order of magnitude larger than those that occur at the mesoscale (Thomas et al., 2008). In order to fully understand the occurrences of the sub-mesoscale flows, the gradient Rossby number must be small ($R_o \ll 1$) and the gradient Richardson number must be large ($R_i \gg 1$). Thus, sub-mesoscale flows can be identified whereby $R_o = |\zeta|/f$ and

$R_i = N^2/|\partial_z \mathbf{u_h}|^2$ are of the order of 1. In order to derive these parameters, the N^2 and f which are defined in the study can be determined from standard glider platforms. Relative vorticity can be inferred from surface velocities derived from the movement of the glider at the surface and the distance between glider profiles. However, the $|\partial_z \mathbf{u_h}|^2$ refers to the vertical shear component whereby in order to determine, one would need velocity measurements at high resolution depth intervals. This can be achieved through the installation of an Acoustic Current Doppler Profiler (ADCP) onto the glider for future missions. This was not done in SOSCEx as an ADCP consumes a considerable amount of power and it is heavy, therefore reducing the efficiency of dives.

7.2.2 Sampling strategy improvements

A Wave Glider is a surface glider that samples the atmosphere-sea interface. Wind speed and directions from the Wave Glider have a temporal resolution of 10 minutes. Sampling a Wave Glider in conjunction with a Seaglider in close proximity allows for a significant improvement of the localised wind stress and direction estimates. This sampling technique has already been completed during the second SOSCEx study. In SOSCEx II, the paired Seaglider and Wave Glider sampled in ′mooring mode′ within a radius of 8 km continually for 4 months (mid-October to mid-February). This sampling technique done by the gliders resembles that of a mooring. The co-location of the two gliders provides both surface atmospheric parameters in conjunction with depth profiles to 1000 m. Additionally, the height at which the Wave Glider samples the atmospheric parameters is at approximately 1 m above sea level, which provides a realistic $in-situ$ wind stress variable that is physically applied to the ocean surface as opposed to the 10 m reference product provided by satellite output.

The sampling strategy of a Seaglider that is directed across a large scale front with dive depths altered from 1000 m to 500 m will half the spatial and temporal resolution between profiles. In determining the evolution of lateral buoyancy gradients, this techniques could prove useful if the glider sampled in ′mooring′ mode. The co-located Seaglider profiles of resolution potentially well within 2 km and 3 $hours$ and accurate wind stress and wind direction measurements from the Wave Glider would increase the accuracy at which the relationship

between wind stress and MLD is determined. It would provide further information into variability of ML eddies and the wind-MLD relationship that if found in this study.

References

Ansorge, I. and Lutjeharms, J. (2003). Eddies originating at the South-West Indian Ridge. *Journal of Marine Systems*, 39(1-2):1–18.

Arhan, M., Speich, S., Messager, C., Dencausse, G., Fine, R., and Boye, M. (2011). Anticyclonic and cyclonic eddies of subtropical origin in the subantarctic zone south of Africa. *Journal of Geophysical Research*, 116:1–22.

Beaulieu, C., Henson, S. a., Sarmiento, J. L., Dunne, J. P., Doney, S. C., Rykaczewski, R. R., and Bopp, L. (2013). Factors challenging our ability to detect long-term trends in ocean chlorophyll. *Biogeosciences*, 10(4):2711–2724.

Belkin, I. and Gordon, A. (1996). Southern Ocean fronts from the Greenwich meridian to Tasmania. *Journal of Geophysical Research*, 101(C2):3675.

Boccaletti, G., Ferrari, R., and Fox-Kemper, B. (2007). Mixed Layer Instabilities and Restratification. *Journal of Physical Oceanography*, 37(9):2228–2250.

Bonjean, F. and Lagerloef, G. S. E. (2002). Diagnostic Model and Analysis of the Surface Currents in the Tropical Pacific Ocean. *Journal of Physical Oceanography*, 32(10):2938–2954.

Bopp, L., Aumont, O., Cadule, P., Alvain, S., and Gehlen, M. (2005). Response of diatoms distribution to global warming and potential implications: A global model study. *Geophysical Research Letters*, 32(19):L19606.

Boyd, P., LaRoche, J., Gall, M., Frew, R., and McKay, R. M. (1999). Role of iron, light, and silicate in controlling algal biomass in subantarctic waters SE of New Zealand. *Journal of Geophysical Research*, 104:395–408.

Brainerd, K. and Gregg, M. (1995). Surface mixed and mixing layer depths. *Deep Sea Research*, 42(95):1521–1543.

Capet, X., McWilliams, J. C., Molemaker, M. J., and Shchepetkin, a. F. (2008). Mesoscale to Submesoscale Transition in the California Current System. Part I: Flow Structure, Eddy Flux, and Observational Tests. *Journal of Physical Oceanography*, 38(1):29–43.

Chelton, D., Deszoeke, R., Schlax, M., Naggar, K., and Siwertz, N. (1998). Geographical variability of the first baroclinic Rossby radius of deformation. *Journal of Physical Oceanography*, 28(1984).

Clifford, M. A. (1983). A descriptive study of the zonation of the Antarctic Circumpolar Current and its relation to wind stress and ice cover. Master's thesis, Texas A&M University.

de Boyer Montégut, C., Madec, G., Fischer, A. S., Lazar, A., and Iudicone, D. (2004). Mixed layer depth over the global ocean: An examination of profile data and a profile-based climatology. *Journal of Geophysical Research*, 109(C12):1–20.

Dong, S., Sprintall, J., Gille, S. T., and Talley, L. (2008). Southern Ocean mixed-layer depth from Argo float profiles. *Journal of Geophysical Research*, 113(C6):C06013.

Donlon, C. J., Martin, M., Stark, J., Roberts-Jones, J., Fiedler, E., and Wimmer, W. (2012). The Operational Sea Surface Temperature and Sea Ice Analysis (OSTIA) system. *Remote Sensing of Environment*, 116:140–158.

Durgadoo, J., Ansorge, I. J., de Cuevas, B., Lutjeharms, J. R. E., and Coward, A. (2011). Decay of eddies at the South-West Indian Ridge. *African Journal of Marine Science*, 107:1–10.

Ekman, P. (1962). An argument for basic emotions. *Cognition & Emotion*, 6(3-4):169–200.

Eriksen, C., Osse, T., Light, R., Wen, T., Lehman, T., Sabin, P., Ballard, J., and a.M. Chiodi (2001). Seaglider: a long-range autonomous underwater vehicle for oceanographic research. *IEEE Journal of Oceanic Engineering*, 26(4):424–436.

Fauchereau, N., Tagliabue, A., Bopp, L., and Monteiro, P. M. S. (2011). The response of phytoplankton biomass to transient mixing events in the Southern Ocean. *Geophysical Research Letters*, 38(17).

Faure, V., Arhan, M., Speich, S., and Gladyshev, S. (2011). Heat budget of the surface mixed layer south of Africa. *Ocean Dynamics*, 61(10):1441–1458.

Fox-Kemper, B., Ferrari, R., and Hallberg, R. (2008). Parameterization of Mixed Layer Eddies. Part I: Theory and Diagnosis. *Journal of Physical Oceanography*, 38(6):1145–1165.

Frajka-Williams, E., Rhines, P. B., and Eriksen, C. C. (2009). Physical controls and mesoscale variability in the Labrador Sea spring phytoplankton bloom observed by Seaglider. *Deep Sea Research Part I: Oceanographic Research Papers*, 56(12):2144–2161.

Garau, B., Ruiz, S., Zhang, W. G., Pascual, A., Heslop, E., Kerfoot, J., and Tintoré, J. (2011). Thermal Lag Correction on Slocum CTD Glider Data. *Journal of Atmospheric and Oceanic Technology*, 28(9):1065–1071.

Gordon, A., Weiss, R., Smethie Jr, W., and Warner, M. (1992). Thermocline and intermediate water communication between the South Atlantic and Indian Oceans. *Journal of Geophysical Research*, 97:7223–7240.

Henson, S. a., Robinson, I., Allen, J. T., and Waniek, J. J. (2006). Effect of meteorological conditions on interannual variability in timing and magnitude of the spring bloom in the Irminger Basin, North Atlantic. *Deep Sea Research Part I: Oceanographic Research Papers*, 53(10):1601–1615.

Huang, N. E., Shen, Z., Long, S. R., Wu, M. C., Shih, H. H., Zheng, Q., Yen, N.-C., Tung, C. C., and Liu, H. H. (1998). The empirical mode decomposition and the Hilbert spectrum for nonlinear and non-stationary time series analysis. *Proceedings of the Royal Society A: Mathematical, Physical and Engineering Sciences*, 454(1971):903–995.

Janzen, C. D. and Creed, E. (2011). Physical Oceanogra aphic Data from Seaglid der Trials in Stratified Coasta al Waters Using a New Pumped Payload CTD. *OCEANS 2011*, IEEE:1–7.

Kara, A. B., Rochford, P. A., and Hurlburt, H. E. (2000). An optimal definition for ocean mixed layer depth. *Journal of Geophysical Research*, 105(C7):16803.

Large, W. and Pond, S. (1981). Open ocean momentum flux measurements in moderate to strong winds. *Journal of Physical Oceanography*, 11:324–336.

Lee, C., Gobat, J., Heywood, K., Queste, B., and Dinniman, M. (2011). Using Gliders to Study a Phytoplankton Bloom in the Ross Sea, Antarctica. *OCEANS 2011*, IEEE:1–7.

Lenton, A., Tilbrook, B., Law, R. M., Bakker, D., Doney, S. C., Gruber, N., Ishii, M., Hoppema, M., Lovenduski, N. S., Matear, R. J., McNeil, B. I., Metzl, N., Mikaloff Fletcher, S. E., Monteiro, P. M. S., Rödenbeck, C., Sweeney, C., and Takahashi, T. (2013). Seaair CO2 fluxes in the Southern Ocean for the period 19902009. *Biogeosciences*, 10(6):4037–4054.

Lévy, M., Ferrari, R., Franks, P. J. S., Martin, A. P., and Rivière, P. (2012). Bringing physics to life at the submesoscale. *Geophysical Research Letters*, 39(14).

Lévy, M., Klein, P., and Ben Jelloul, M. (2009). New production stimulated by high-frequency winds in a turbulent mesoscale eddy field. *Geophysical Research Letters*, 36(16):L16603.

Levy, M. and Martin, A. (2013). The influence of mesoscale and submesoscale heterogeneity on ocean biogeochemical reactions. *Global Biogeochemical Cycles*, 27(4):1139–1150.

Lutjeharms, J. and Ansorge, I. (2001). The Agulhas Return Current. *Journal of Marine Systems*, 30(1-2):115–138.

Mahadevan, A., Asaro, E. D., Lee, C., and Perry, M. J. (2012a). Supporting Online Material: Eddy-driven stratification initiates a North Atlantic Spring phytoplankton bloom. *Science*, 54:1–25.

Mahadevan, A., D'Asaro, E., Lee, C., and Perry, M. (2012b). Eddy-driven stratification initiates North Atlantic spring phytoplankton blooms. *Science*, 54.

Mahadevan, A. and Tandon, A. (2006). An analysis of mechanisms for submesoscale vertical motion at ocean fronts. *Ocean Modelling*, 14(3-4):241–256.

Mahadevan, A., Tandon, A., and Ferrari, R. (2010). Rapid changes in mixed layer stratification driven by submesoscale instabilities and winds. *Journal of Geophysical Research*, 115(C3):C03017.

Marshall, J. and Jones, H. (2002). Can eddies set ocean stratification? *Journal of Physical Oceanography*, 32:26–38.

Metzl, N., Tilbrook, B., and Poisson, A. (1999). The annual fCO2 cycle and the airsea CO2 flux in the subAntarctic Ocean. *Tellus*, 51B:849–861.

Monteiro, P., Boyd, P., and Bellerby, R. (2011). Role of the seasonal cycle in coupling climate and carbon cycling in the Subantarctic zone. *Eos, Transactions American Geophysical Union*, 92(28):235.

Nowlin, W. D. and Klinck, J. M. (1986). The physics of the Antarctic Circumpolar Current. *Reviews of Geophysics*, 24(3):469.

Obata, A., Ishizaka, J., and Endoh, M. (1996). Global verification of critical depth theory for phytoplankton bloom with climatological in situ temperature and satellite ocean color data. *Journal of Geophysical Research*, 101(C9):657–667.

Olita, A., Sparnocchia, S., Cusí, S., Fazioli, L., Sorgente, R., Tintoré, J., and Ribotti, A. (2014). Observations of a phytoplankton spring bloom onset triggered by a density front in NW Mediterranean. *Ocean Science*, 10(4):657–666.

Orsi, A., Whitworth III, T., and Nowlin Jr, W. (1995). On the meridional extent and fronts of the Antarctic Circumpolar Current. *Deep Sea Research*, 42(5):641–673.

Parish, T. and Bromwich, D. (1998). A Case Study of Antarctic Katabatic Wind Interaction with Large-Scale Forcing*. *Monthly Weather Review*, pages 199–209.

Pasquero, C., Bracco, A., and Provanzale, A. (2005). Impact of the spatiotemporal variability of the nutrient flux on primary productivity in the ocean. *Journal of Geophysical Research*, 110(C7):C07005.

Patoux, J., Yuan, X., and Li, C. (2009). Satellite-based midlatitude cyclone statistics over the Southern Ocean: 1. Scatterometer-derived pressure fields and storm tracking. *Journal of Geophysical Research*, 114(D4):D04105.

Perry, M., Sackmann, B. S., Eriksen, C. C., and Lee, C. M. (2008). of blooms and subsurface observations maxima off the chlorophyll Seaglider coast. *Limnology and Oceanography*, 53(5):2169–2179.

Pollard, R., Lucas, M., and Read, J. (2002). Physical controls on biogeochemical zonation in the Southern Ocean. *Deep Sea Research Part II: Topical Studies*, 49(2002):3289–3305.

Price, J. F., Weller, R. A., and Pinkel, R. (1986). Diurnal cycling: Observations and models of the upper ocean response to diurnal heating, cooling, and wind mixing. *Journal of Geophysical Research*, 91(C7):8411.

Rato, R., Ortigueira, M., and Batista, A. (2008). On the HHT, its problems, and some solutions. *Mechanical Systems and Signal Processing*, 22(6):1374–1394.

Rintoul, S. and Trull, T. (2001). Seasonal evolution of the mixed layer in the Subantarctic Zone south of Australia. *Journal of Geophysical Research*, 106(C12):31,447–31,462.

Rintoul, S. R. (1991). South Atlantic interbasin exchange. *Journal of Geophysical Research*, 96(C2):2675.

Rintoul, S. R. and Sokolov, S. (2001). Baroclinic transport variability of the Antarctic Circumpolar Current south of Australia (WOCE repeat section SR3). *Journal of Geophysical Research*, 106(C2):2815.

Rudnick, D. L. and Cole, S. T. (2011). On sampling the ocean using underwater gliders. *Journal of Geophysical Research*, 116(C8):C08010.

Sackmann, B. S., Perry, M. J., and Eriksen, C. C. (2008). Seaglider observations of variability in daytime fluorescence quenching of chlorophyll-a in Northeastern Pacific coastal waters. *Biogeosciences Discussions*, 5(4):2839–2865.

Sallée, J. B., Speer, K. G., and Rintoul, S. R. (2010). Zonally asymmetric response of the Southern Ocean mixed-layer depth to the Southern Annular Mode. *Nature Geoscience*, 3(4):273–279.

Sarmiento, J., Gruber, N., Brzezinski, M., and Dunne, J. (2004). High-latitude controls of thermocline nutrients and low latitude biological productivity. *Nature*, 427(January).

Sarmiento, J., Hughes, T., Stouffer, R., and Manabe, S. (1998). Simulated response of the ocean carbon cycle to anthropogenic climate warming. *Nature*, 393(May):1–2.

Schlitzer, R. (2002). Carbon export fluxes in the Southern Ocean: results from inverse modeling and comparison with satellite-based estimates. *Deep Sea Research Part II: Topical Studies in Oceanography*, 49(9-10):1623–1644.

Schulz, E. W., Josey, S. a., and Verein, R. (2012). First air-sea flux mooring measurements in the Southern Ocean. *Geophysical Research Letters*, 39(16).

Sokolov, S. and Rintoul, S. R. (2007). Multiple Jets of the Antarctic Circumpolar Current South of Australia*. *Journal of Physical Oceanography*, 37(5):1394–1412.

Speich, S., Blanke, B., and Madec, G. (2001). Warm and cold water routes of an OGCM thermohaline conveyor belt. *Geophysical Research Letters*, 28(2):311–314.

Sverdrup, H. (1953). On conditions for the vernal blooming of phytoplankton. *Journal du Conseil*, pages 287–295.

Swart, S., Chang, N., Fauchereau, N., Joubert, W., Lucas, M., Mtshali, T., Roychoudhury, A., Tagliabue, A., Thomalla, S., Waldron, H., and Monteiro, P. M. (2012). Southern Ocean Seasonal Cycle Experiment 2012: Seasonal scale climate and carbon cycle links. *South African Journal of Science*, 108(3/4):3–5.

Swart, S. and Speich, S. (2010). An altimetry-based gravest empirical mode south of Africa: 2. Dynamic nature of the Antarctic Circumpolar Current fronts. *Journal of Geophysical Research*, 115(C3):C03003.

Swart, S., Speich, S., Ansorge, I. J., Goni, G. J., Gladyshev, S., and Lutjeharms, J. R. E. (2008). Transport and variability of the Antarctic Circumpolar Current south of Africa. *Journal of Geophysical Research*, 113(C9):C09014.

Swart, S., Thomalla, S., and Monteiro, P. (2014). The seasonal cycle of mixed layer dynamics and phytoplankton biomass in the Sub-Antarctic Zone: A high-resolution glider experiment. *Journal of Marine Systems*.

Tagliabue, A., Sallée, J., Bowie, A., Lévy, M., Swart, S., and Boyd, P. W. (2014). Surface-water iron supplies in the Southern Ocean sustained by deep winter mixing. *Nature Geoscience*, 21(March):1–7.

Tandon, A. and Garrett, C. (1994). Mixed layer restratification due to a horizontal density gradient. *Journal of Physical Oceanography*, 24.

Tandon, A. and Garrett, C. (1995). Geostrophic adjustment and restratification of a mixed layer with horizontal gradients above a stratified layer. *Journal of Physical Oceanography*, 25.

Taylor, J. R. and Ferrari, R. (2010). Buoyancy and Wind-Driven Convection at Mixed Layer Density Fronts. *Journal of Physical Oceanography*, 40(6):1222–1242.

Taylor, J. R. and Ferrari, R. (2011). Ocean fronts trigger high latitude phytoplankton blooms. *Geophysical Research Letters*, 38(23).

Thomalla, S., Fauchereau, N., Swart, S., and Monteiro, P. M. S. (2011). Regional scale characteristics of the seasonal cycle of chlorophyll in the Southern Ocean. *Biogeosciences*, 8:2849–2866.

Thomas, L. and Lee, C. (2005). Intensification of ocean fronts by down-front winds. *Journal of Physical Oceanography*, 35(1972):1086–1102.

Thomas, L., Tandon, A., and Mahadevan, A. (2008). Submesoscale processes and dynamics. *Ocean modeling in an Eddying Regime*, pages 17–38.

Thomson, R. and Fine, I. (2003). Estimating mixed layer depth from oceanic profile data. *Journal of Atmospheric and Oceanic Technology*, 20:319–329.

Trenberth, K. (1991). Storm tracks in the Southern Hemisphere. *Journal of the Atmospheric Sciences*, 48(19).

Trenberth, K., Large, W., and Olson, J. (1990). The mean annual cycle in global ocean wind stress. *Journal of Physical Oceanography*.

Waniek, J. J. (2003). The role of physical forcing in initiation of spring blooms in the northeast Atlantic. *Journal of Marine Systems*, 39(1-2):57–82.

Yuan, X., Patoux, J., and Li, C. (2009). Satellite-based midlatitude cyclone statistics over the Southern Ocean: 2. Tracks and surface fluxes. *Journal of Geophysical Research*, 114(D4):D04106.

Zhang, H.-M., Bates, J. J., and Reynolds, R. W. (2006). Assessment of composite global sampling: Sea surface wind speed. *Geophysical Research Letters*, 33(17):L17714.